Theses and Dissertations

2010

Magnetic field effects on electron transfer reactions: heterogeneous photoelectrochemical hydrogen evolution and homogeneous self exchange reaction

Heung Chan Lee
University of Iowa

Recommended Citation

Lee, Heung Chan. "Magnetic field effects on electron transfer reactions: heterogeneous photoelectrochemical hydrogen evolution and homogeneous self exchange reaction." PhD (Doctor of Philosophy) thesis, University of Iowa, 2010.
http://ir.uiowa.edu/etd/2562.

MAGNETIC FIELD EFFECTS ON ELECTRON TRANSFER REACTIONS:

HETEROGENEOUS PHOTOELECTROCHEMICAL HYDROGEN EVOLUTION

AND HOMOGENEOUS SELF EXCHANGE REACTION

by

Heung Chan Lee

An Abstract

Of a thesis submitted in partial fulfillment
of the requirements for the Doctor of
Philosophy degree in Chemistry
in the Graduate College of
The University of Iowa

May 2011

Thesis Supervisor: Associate Professor Johna Leddy

ABSTRACT

Magnetic field effects (MFE) on electrochemical systems have been of interest to researchers for the past 60 years. MFEs on mass transport, such as magnetohydrodynamics and magnetic field gradients effects are reported, but MFEs on electron transfer kinetics have been rarely investigated. Magnetic modification of electrodes enhances electron transfer kinetics under conditions of high concentrations and low physical diffusion conditions, as shown by Leddy and coworkers. Magnetic microparticles embedded in an ion exchange polymer (e.g., Nafion) applied to electrode surfaces. Rates of electron transfer reactions to diffusing redox probes and to adsorbates are markedly enhanced.

This work reports MFEs on hydrogen evolution on illuminated p-Si; MFEs on hydrogen evolution on noncatalytic electrodes; a model for MFEs on homogeneous self-exchange reactions; and a convolution based voltammetric method for film modified electrodes.

First, a MFE on the photoelectrochemical hydrogen evolution reaction (HER) at p-Si semiconductors is demonstrated. The HER is an adsorbate reaction. Magnetic modification reduces the energetic cost of the HER by 400 - 500 mV as compared to Nafion modified electrodes and by 1200 mV as compared to unmodified p-Si. Magnetically modified p-Si achieves 6.2 % energy conversion efficiency. Second, from HER on noncatalytic electrodes, the MFE on photoelectrochemical cells arises from improved heterogeneous electron transfer kinetics. On glassy carbon electrodes, magnetic modification improves heterogeneous electron transfer rate constant, k_0, for HER 80, 000 fold. Third, self exchange reaction rates are investigated under magnetic

modification for various temperatures, outersphere redox probes, and magnetic particles. Arrhenius analyses of the rate constants collected from the experiments show a 30 - 40 % decrease in activation energy at magnetically modified electrodes. A kinetic model is established based on transition state theory. The model includes pre-polarization and electron nuclear spin polarization steps and characterizes a majority of the experimental results. Lastly, a convolution technique for modified with uniform films electrodes is developed and coded in Matlab (mathematical software) for simple and straightforward analysis of Nafion modified electrodes.

Abstract Approved: _____

Thesis Supervisor

Associate Professor   Chemistry

Title and Department

1 December 2010

Date

MAGNETIC FIELD EFFECTS ON ELECTRON TRANSFER REACTIONS:

HETEROGENEOUS PHOTOELECTROCHEMICAL HYDROGEN EVOLUTION

AND HOMOGENEOUS SELF EXCHANGE REACTION

by

Heung Chan Lee

A thesis submitted in partial fulfillment
of the requirements for the Doctor of
Philosophy degree in Chemistry
in the Graduate College of
The University of Iowa

May 2011

Thesis Supervisor: Associate Professor Johna Leddy

Graduate College
The University of Iowa
Iowa City, Iowa

CERTIFICATE OF APPROVAL

_____

PH.D. THESIS

_____

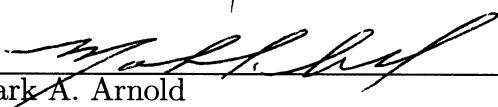This is to certify that the Ph.D. thesis of

Heung Chan Lee

has been approved by the Examining Committee for the thesis
requirement for the Doctor of Philosophy degree in Chemistry
at the May 2011 graduation.

Thesis Committee: _____
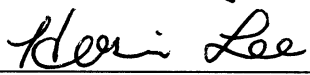   Johna Leddy, Thesis Supervisor

                   _____
                   Mark A. Arnold

                   _____
                   Edward G. Gillan

                   _____
                   Lei Geng

                   _____
                   Hosin Lee

To the one by whom I am defined

ACKNOWLEDGMENTS

TABLE OF CONTENTS

LIST OF TABLES

Table

vii

CHAPTER 1

INTRODUCTION

As demands for sustainable energy increase, molecular hydrogen becomes a strong candidate as a next generation fuel. However, hydrogen as a fuel is not realized because its production and environmental cost are higher than that of petroleum energy even when hydrogen is produced by the most advanced technologies. Among the technologies, a photoelectrochemical cell is a system that can produce hydrogen in the most sustainable way with high efficiency because it directly converts solar energy to chemical energy that is then stored as molecular hydrogen. Thermodynamically, electrochemical energy conversion is more efficient than conventional energy conversion system such as combustion engines whose maximum efficiency is limited theoretically by the Carnot cycle.

However, slow electron transfer kinetics limit the practicality of these electrochemical systems. Electron transfer kinetics are involved in all electrochemical energy conversion systems. Photoelectrochemical solar to electric or chemical energy conversion also suffers from slow kinetics although they are thermodynamically more advantageous than any other energy production methods.

Electrons have two properties, one is charge and the other is spin. Magnetic field effects on electron transfer events have been reported between paramagnetic species as well as between para- and diamagnetic species by Shelley Minteer [1] and Wayne Gellett [2]. Magnetic fields improve the kinetics of electron transfer events.

Here, solar to chemical energy conversion under magnetic fields will be discussed as well as fundamental aspects of magnetic field effects on electron transfer kinetics

that include homogeneous self exchange reactions and heterogenous electron transfer reactions. Homogeneous electron transfer occurs in a single phase as in solution or in the solid state. Heterogeneous electron transfer occurs across an interface, such as across the electrode|solution interface.

1.1   Magnetic Field Effects on Electrochemical Systems

At room temperature, magnetic fields influence chemical systems through dynamics [3–9]. Effects on transport, that include magnetohydrodynamics (MHD) and gradient magnetic field effects, have been achieved by placing electrodes in an externally applied magnetic field [10–14]. Incorporation of a permanent magnetic field at the electrode surface provides advantages of experimental simplicity and reduced weight. Magnetically modified electrodes can sustain a permanent magnetic field because magnetic microparticles are either attached to the electrode surface or incorporated into the electron conductor that is the electrode itself. In a number of systems, magnetic modification of electrode surfaces increases electrochemical flux as compared to electrodes without magnetic modification [15–23].

On the other hand, electron transfer kinetic enhancements at magnetically modified electrodes are also reported when physical diffusion in a polymer matrix are limited by restricted motion of redox couples trapped in a polymer matrix and redox couples are adsorbed on an electrode surface. Improved homogenous outer sphere electron transfer kinetic of transition metal complexes trapped in a polymer matrix was demonstrated by Minteer [1] and Gellett [2]. Gellett also reports enhanced heterogeneous electron transfer kinetic for oxidation of adsorbed carbon monoxide

at magnetically modified Pt electrodes [2]. Magnetic modifications are also reported
for polymer electrolyte fuel cell electrodes [24], nickel hydroxide|nickel oxyhydroxide
electrodes of nickel metal hydride and nickel cadmium batteries [25], and manganese
dioxide electrodes of alkaline primary batteries [26–28].

Here, magnetically modified silicon photoelectrodes, non-catalytic electrodes are
presented, as are models for homogeneous electron transfer under magnetic fields.

1.2 Photoelectrochemical Hydrogen Evolution Reactions

Since Fujishima and Honda first demonstrated photoelectrochemical water
splitting [29], research has been conducted to improve the dynamics and systems of
semiconductor photoelectrochemistry. Bard et. al. suggested a conceptual design
for an optimized photoelectrochemical cell [30]. Lewis reviewed and explained the
physicochemistry of heterogeneous electron transfer kinetics at a semiconductor
electrode surface and an electrolyte junction [31]. Turner reviewed hydrogen
production and demonstrated a photoelectrochemical water splitting system that
uses two different semiconductors for the photoanode and photocathode [32, 33].

Although a photoelectrochemical cell can provide photoenergy conversion
efficiency of up to 17 % for the generation of electrical energy and 10 % to fuels
conceptually, much remains to make a photoelectrochemical energy conversion a
practical system [34].

A key component of a photoelectrochemical cell is the semiconductor electrode.
Silicon is an effective photoelectrode because of its excellent thermodynamic

properties for energy conversion as compared to other semiconductor materials. Silicon has an optimized band gap to harvest the solar spectrum. To produce molecular hydrogen by reducing water, a p-type semiconductor is required as its photogenerated minority carriers, electrons, drive photoreduction.

A major limitation of photoelectrochemical hydrogen evolution on the p-Si photocathode is that the heterogeneous electron transfer kinetics from photogenerated electrons in a p-type silicon to adsorbed protons on the surface of the p-type silicon are too slow to drive the photoelectrochemical reduction. Slow kinetics could arise from surface recombination between photogenerated electrons and holes on silicon surface defects sites and from sluggish heterogeneous electron transfer events. Therefore, if the reaction rate on p-Si is increased, hydrogen production is enabled at lower cost.

There have been various approaches to improve the rate of hydrogen photoreduction at p-Si. A notable modification to the p-Si surface was performed by M. Szklarczykt and J. O'M. Bockris [35], who coated surfaces with various metal catalysts and achieved a quantum efficiency of 1.4 % with a nickel coating. Although coating with catalysts could make photoelectrosynthetic hydrogen evolution possible, desirable efficiency and stability of such coatings are not yet achieved.

A quantum efficiency is a percentage of the number of separated charges over the number of photons hitting the surface of a device whereas an energy conversion efficiency is a percentage of the produced energy from the device over total light energy given to the device.

1.3 Self Exchange Reaction

A self exchange reaction is electron transfer reaction between two molecules identical except for different charge states.

$$M^n + M^{n+1} \leftrightarrows M^{n+1} + M^n$$
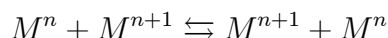
M^n is a metal with charge of n. M^n and M^{n+1} are two halves of a single redox couple. The electron transfers results in an effective transposition of M^n and M^{n+1}. The rates of the forward and backward reactions are the same. The rate constant for a self exchange reaction (k_{se}) is a parameter important to the analysis of magnetic field effects on kinetics. This rate can be measured spectroscopically and electrochemically. Here, the self exchange reaction rate constants are measured electrochemically by measuring the hopping diffusion rate of transition metal complexes embedded in a Nafion matrix where physical diffusion is restricted and probe concentration is high. When magnetic microparticles are also embedded in Nafion, the self exchange rates increase. A model based on activated complex theory is presented. By measuring the self exchange rate constants at various temperatures, more detailed physical parameters in the rate constants are determined. Impacts of magnetic fields on homogeneous electron transfer rates are discussed.

1.4 Heterogeneous Electron Transfer Reactions

Heterogeneous electron transfer is a reaction that involves electron transfer across the interface between an electrode and the electrolyte that contains the redox probe. According to Marcus theory, this heterogeneous electron transfer reaction

rate constant can be derived from the rate of the self exchange reaction of the redox couple involved in the heterongenous reaction if the reaction is an ideal, outer sphere electron transfer reaction [36]. The hydrogen evolution reaction is an adsorbate reaction and there is no appropriate way to estimate or calculate the heterogeneous rate constant from its homogeneous rate constant. On a platinum electrode, hydrogen evolution is catalytic and the heterogeneous electron transfer rate is reversible; that is the electron transfer is fast relative to the rate of the measurement and mass transport. Therefore, at normal measurement time scales, further enhancements in the electron transfer rate are not anticipated. However, on a noncatalytic electrode, hydrogen evolution kinetics are slow (quasireversible or irreversible). On noncatalytic surfaces, electron transfer kinetics are enhanced by magnetic modification.

Here, the rates of hydrogen evolution reactions on noncatalytic electrodes such as glassy carbon (GC) electrodes and n-type gallium arsenide (n-GaAs) electrodes have been studied to demonstrate the effects of magnetic field on heterogeneous electron transfer reactions.

1.5   Uniform Film Modified Electrodes

Nafion is used ubiquitously to modify electrodes. Because Nafion provides slow physical diffusion and high concentrations, it is a matrix commonly involved in studies of magnetically modified electrodes. The importance of understanding the properties of Nafion modification on electrodes cannot be overstated. Nafion is a well known ion exchange polymer. The chemical structure of Nafion is shown in
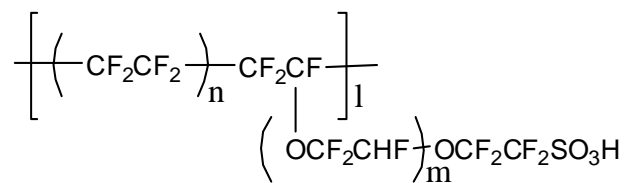
Figure 1. The general chemical structure of Nafion.

Figure 1.

When an electrode coated with Nafion is placed in an electrolyte solution containing a redox probe, the probe partitions between the Nafion film and the electrolyte. The process is characterized by an extraction parameter (κ). During electrolysis of the probe, the diffusion profiles at the film solution interface are coupled through κ. Schematic of the system is shown in Figure 46 (page 128).

Solution of Fick's second law by Laplace transform gives an exact solution of the diffusion profile of this electrochemical system. This solution is the basis for the convolution analysis protocol described below.

Convolution, also known as the semi-integration, allows easier and more straight forward interpretation of many types of electrochemical sweep voltammograms than unprocessed current and voltage data analysis. It can be also used to eliminate unwanted charging capacitance and rapid assessment of reaction kinetics [37].

Here, the convolution technique for uniform film modified electrodes is modeled mathematically. Exact solution of the diffusion profiles is provided by Laplace transform. The resulting equations are computationally coded in Matlab, mathematical programming software, and used to fit experimental data as a means

to demonstrate the method for assessing film parameters of partition coefficient (κ), diffusion coefficients in the film (D_f) and solution (D_s), and film thickness (l).

CHAPTER 2

MAGNETIC FIELD EFFECT ON PHOTOELECTROCHEMISTRY

When semiconductors are irradiated by light, photons with higher energy than its band gap separate charges, electrons and holes, into a conduction band and a valence band, respectively. These separated charges flow along the potential gradients formed in the semiconductor and can drive reactions on the surface of the electrode in contact with the electrolyte. Possible reactions include catalysis and synthesis and these reactions are widely called photoelectrochemistry.

The hydrogen evolution reaction is of great current interest because hydrogen is an excellent source of alternative fuel. A photoelectrochemical cell can generate hydrogen by conversion of light energy. Sunlight is the most sustainable means of energy generation on the earth. However, slow reaction kinetics on the semiconductor surface is the major obstacle to the practicality of this reaction. Here, we improve reaction kinetics by modifying semiconductor electrodes with magnetic particles that establish magnetic fields.

2.1   Theoretical Background

By definition, a semiconductor is a material for which conductivity increases with increased temperature. Semiconductors have a band gap in their electronic energy states. The lower band is called the valance band and the upper band is called the conduction band.

An intrinsic semiconductor has equal density of electrons and holes because when

an electron is generated in the conduction band, a hole is simultaneously generated in the valence band. The Fermi level is the average energy of carriers and is midway between the conduction band and the valence band energies. (See Figure **??**.)

When a intrinsic semiconductor is doped with an electron rich dopant, the majority carriers are electrons and the Fermi level is established just below the conduction band. This is an n-type semiconductor. When an intrinsic semiconductor is doped with electron poor dopant, the majority carriers are holes and the Fermi level is established just above valence. This is called a p-type semiconductor.

Semiconductors are integral to photoelectrochemical cells. Light energy greater than the band gap energy separates charges (electrons and holes) in the semiconductor and photoelectrochemical cells use the potential of the separated charges to drive reactions. When the band gap is 1.2 - 1.4 V, solar energy conversion efficiency is theoretically maximized [38]. If the band gap of the semiconductor is smaller than the theoretical optimum, the semiconductor harvests more photons, but the operation potential of the cell is smaller and corresponds to a smaller band gap. If the band gap is larger than the theoretical optimum, the electric potential of the separated charges is higher but the number of photons the semiconductor can harvest is reduced and overall efficiency drops.

2.1.1   Photoelectrochemistry of Semiconductor Electrodes

Figure 2 shows the energy diagram of a p-type semiconductor on the left side and a redox couple in an electrolyte on the right side. Fermi energy level (E_f) is

established just above the valence band for a p-type semiconductor. In this energy state flat band potential (E_{fb}) equals the Fermi level. When the electrolyte and semiconductor make contact, their potentials equilibrate and a potential gradient is generated in the semiconductor because an electrical double layer forms in the semiconductor near the semiconductor electrolyte interface. Because the number of energy states on the electrolyte side is greater than the number of energy states in semiconductor, the Fermi level of the semiconductor moves to the Fermi level of redox couple in the electrolyte. Electrical double layers form on the electrolyte side as well, but its effects are negligible as compared to the extensive potential gradient in the semiconductor. Figure 3 represents the equilibrium state between a p-type semiconductor and an electrolyte junction.

If a p-type semiconductor is illuminated with light, photons with higher energy than the band gap energy separate charges into the conduction band and the valance band. Separated electrons are dragged toward the electrode surface by the potential gradients whereas holes are dragged to the back side of the semiconductor electrode. The electrons with higher potential than the redox potential of the redox couple in the electrolyte can drive an electrochemical reaction. Figure 4 shows the schematic procedure of the photoelectrochemical reaction.

The flat band potential (V_{fb}) is the potential when there is no potential gradient in the semiconductor, so there is no band bending and valence and conduction bands are flat. For p-type semiconductors, when the potential is swept from positive to negative potentials, the photoelectrochemical reaction can be driven from the flat band potential (V_{fb}). The flat band potential can be measured from the onset
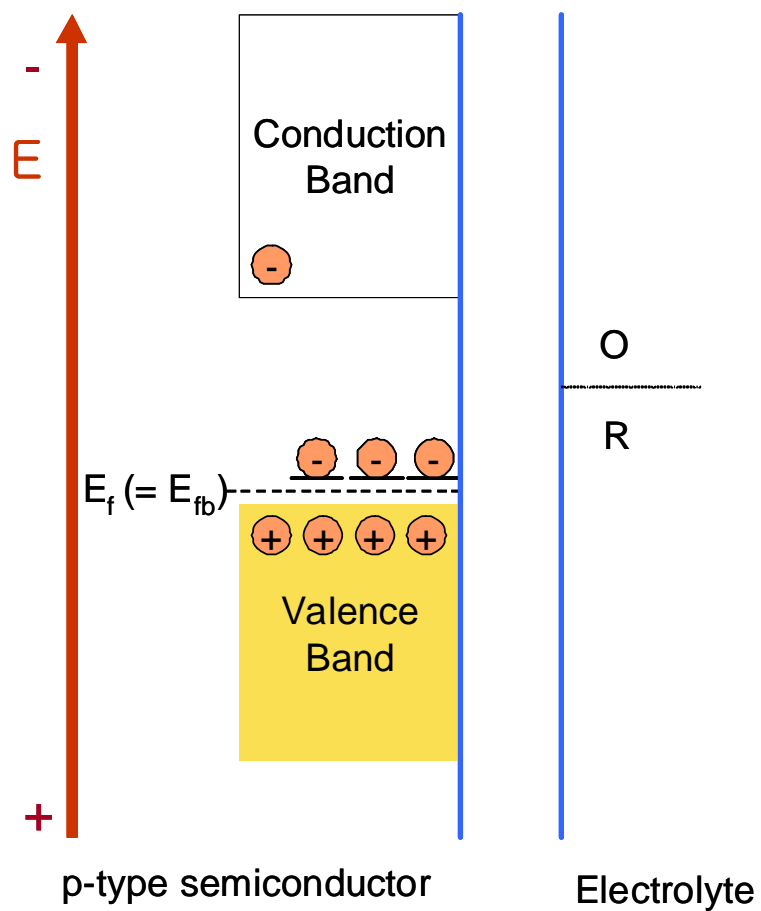
Figure 2. Energy diagram of a p-type semiconductor and an electrolyte containing a redox couple not yet in contact. Fermi energy level (E_f) is established just above the valence band for a p-type semiconductor. In this energy state, the flat band potential (E_{fb}) equals the Fermi level.
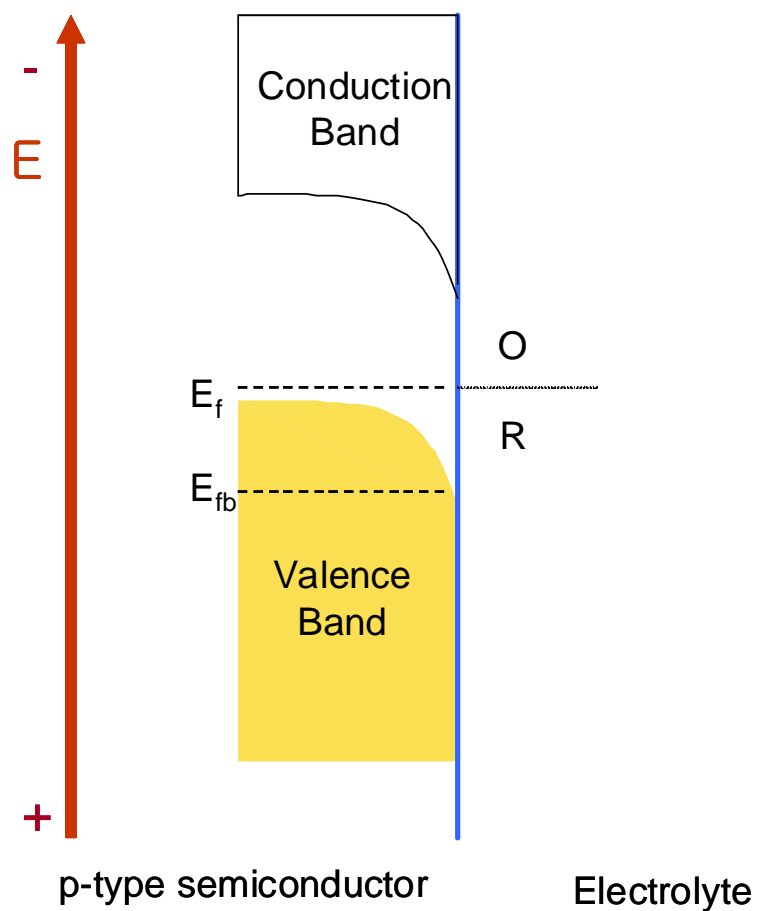
Figure 3. Energy diagram of a p-type semiconductor and an electrolyte with redox couple in contact. When the two phases contact each other, equilibrium is established and the extensive potential gradient is formed in semiconductor.

potential of the reduction reaction or an AC impedance measurement. Because the onset potential measurements are not accurate in most cases due to slow electron transfer kinetics, and corresponding high overpotential, AC impedance measurements are widely used.

A ideal photoelectrochemical process of a p-type semiconductor can be described by Equation 1.

$$I = I_{ph} - I_0 \left[\exp\left(\frac{qV}{kT}\right) - 1 \right] \tag{1}$$

$$I = -I_0 \left[\exp\left(\frac{qV}{kT}\right) - 1 \right] \tag{2}$$

I_{ph} is the photocurrent that approximately equals the photon flux; V is the applied potential (V); q is charge on the carrier; k is the Boltzman constant (J/K); and T is temperature (K). I_0 can be interpreted as the exchange current density (s^{-1}), a measure of the heterogeneous electron transfer between the majority carrier (holes) and the reduced species of redox probe in solution [31]. Details of I_0 are described in Equations 3, 4 and 5.

$$I_0 \;=\; h_{so}C \tag{3}$$

$$C \;=\; qAk_{et}[R]_s \tag{4}$$

$$h_{so} \;=\; h_b \exp\left(-\frac{q\,|V_{bi}|}{kT}\right) \tag{5}$$

A is an electrode area (cm^2); k_{et} is the electron transfer rate constant (cm^4/s); $[R]_s$ is the concentration of an reduced species at the surface of an electrode (cm^{-3}); V_{bi} is the built-in potential due to the potential gradient (V); h_b is the concentration of majority carriers (holes) in a bulk p-type semiconductor (cm^{-3}); and h_{so} is the
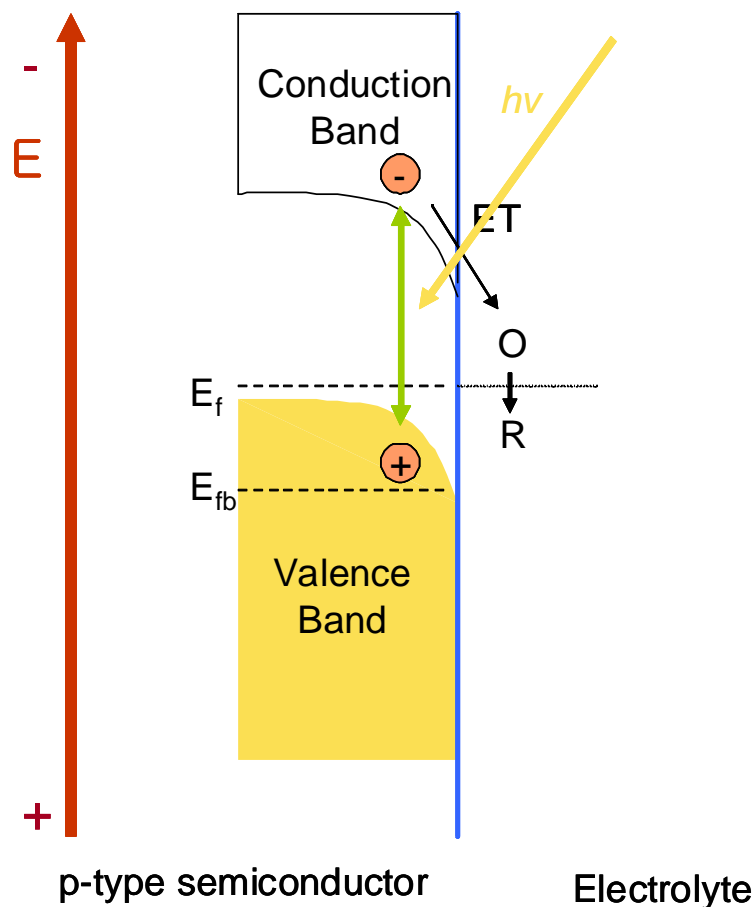
Figure 4. Energy diagram of a p-type semiconductor and an electrolyte with a redox couple junction under illumination with energy higher than the band gap of the semiconductor. Photons with higher energy than the band gap energy generates charges and the charges separate as they move apart along the the potential gradient established in the semiconductor.

concentration of majority carrier (holes) at the surface of the electrode (cm^{-3}) at equilibrium.

Figure 5 shows current voltage profiles of p-type semiconductor electrochemical cells. The solid blue and red lines are calculated ideal current voltage profiles for fast electron transfer kinetics when a cell is under dark conditions and when a cell is illuminated, respectively. The green dotted line is a typical current voltage profile
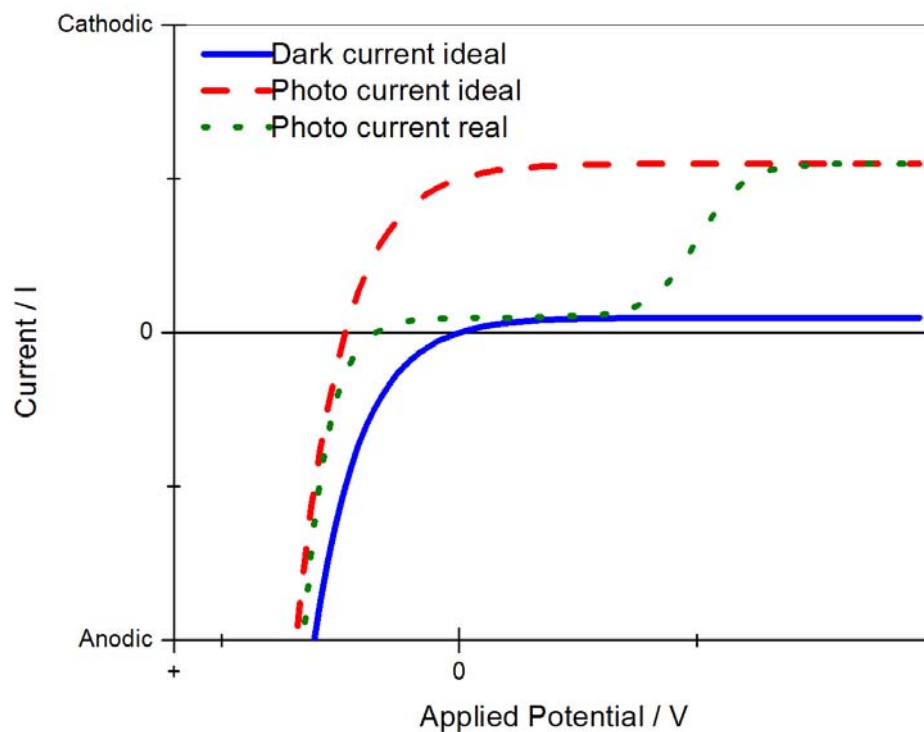
Figure 5. Current and voltage profiles of a p-type semiconductor electrochemical cell. The solid blue line is a current response when a cell is not illuminated. When a cell is illuminated, the calculated ideal photocurrent is the dashed red line. The green dotted line is a typical current voltage profile of a p-type semiconductor electrochemical cell that shows high overpotential due to slow reaction kinetic for electron transfer.

of p-type semiconductor electrochemical cell in most cases. To drive a reaction, the system needs a high over potential to overcome slow reaction kinetics. Overpotential is any voltage applied in excess of the thermodynamic potential that is used to over come a resistance, such as resistance to electron transfer and resistance to mass transport. For ideal cases, the current voltage profiles are plotted using Equations 1 and 2 for light condition and for dark condition, respectively.

2.1.2 Hydrogen Evolution Reaction (HER) on Silicon Electrodes

Although a current voltage profile of a semiconductor should represent a rectifying current, silicon (Si) does not show clear rectifying behavior because of silicon chemistries under oxidizing conditions. When silicon is oxidized, as in the anodic current area, it tends to be silicon dioxide (SiO_2). The silicon dioxide layers act as insulators and prevent the electrode from further electrochemical reaction. Hydrofluoric acid (HF) is traditionally used to evaluate silicon under anodic conditions because HF dissolves the silicon oxide layer. For the hydrogen evolution reaction (HER), only the cathodic current is of interest and the anodic current area is not interrogated voltammetrically.

2.1.3 Energy Conversion Efficiency

Photoconversion efficiencies, η, of three-electrode photoelectrochemical cells are calculated as

$$\eta(\%) \quad = \quad 100 \times \frac{j_p \times V}{I_l} \tag{6}$$

$$V \quad = \quad E_{meas} - E \tag{7}$$

where I_l (W/cm^2) is the power density of the incident light, and the photocurrent density, j_p (A/cm^2), is the current density measured at a potential, E_{meas} (V). E is the thermodynamic potential of the hydrogen evolution reaction in a given system. Because open circuit potential of hydrogen evolution on p-Si cannot be determined in the absence of hydrogen, E is measured from a hydrogen evolution current-potential

profile on a platinum electrode at the same pH.

$$E = E^{o\prime} - \frac{0.0591}{2} \log \frac{P_{H_2}}{[H^+]^2} \tag{8}$$

As shown below, photoconversion efficiencies on p-Si can only be calculated for the magnetically modified semiconductor electrodes. Only the magnetically modified p-Si demonstrate economically feasible light energy to hydrogen. To evolve hydrogen with the p-Si photocathode in either acidic or basic solution, higher overpotential is needed than the thermodynamic potential for hydrogen evolution on a platinum electrode, so the photoconversion efficiency is negative. On a magnetically modified p-Si electrode under illumination, the potential applied to generate hydrogen is less than the potential applied at platinum, so the photoconversion efficiencies are positive. The lower applied potential at magnetically modified p-Si reflects the efficiency of conversion of light energy into electrochemical energy.

2.2 Experimental

2.2.1 Magnetic Particles

Magnetic microparticles previously made in house were prepared [1, 2, 39]. Magnetite (Fe_3O_4) particles (Aldrich, < 5 μm) were ball milled in hexane for 20 minutes to a uniform particle size. The ball milled magnetite particles (1 g) were then added to a mixture of toluene (10 mL) and (3-aminopropyl)trimethoxysilane (10 mL; Alfa Aesar) in a 20 mL screw-cap vial, and the mixture was agitated by slow rotation of the vial for 4 hours. The supernatant was decanted and the particles

were washed with toluene (3 × 20 mL). The particles were dried overnight in a vacuum oven at 70 °C. Ethylene glycol diglycidyl ether (10 mL) and deionized water (10 mL) are added into the vial containing the dried particles and the mixture was agitated by slow rotation (~30 rpm) of the vial for 4 hours. The particles were then rinsed with deionized water (3 × 20 mL), dried overnight in a vacuum oven at 70 °C, and stored in a capped vial. Thickness of the encapsulation was controlled by amount of added reagents. As prepared here, the siloxane encapsulated magnetic particles were less than 5 μm in diameter. The sizes of magnetic particles were little changed by the coating. The thickness of the siloxane coating was about 10 to 30 Å that was determined by thermal gravimetric analysis (TGA) [2]. Properties vary from batch to batch and coating thickness and size of the particle can vary by batch. However, scanning electron microscope (SEM) images determine typical diameters of the coated magnetic particles were about 4 - 5 μm.

2.2.2 Preparation of Silicon Electrodes

Five kinds of p-type silicon were used to fabricate semiconductor electrodes. For p-Si with a (100) surface, wafers of resistivity of 1 - 4 Ωcm (ITME), 0.5 - 1.5 Ωcm (ElCat) and 0.001 - 0.005 Ωcm (ElCat) were purchased. For p-Si with (110) and (111) surfaces, wafers of resistivity of 2 - 4 Ωcm (ElCat) and 3 - 6 Ωcm (ITME) were purchased, respectively. Refer to Table 1 for details. Labels and specifications of p-Si wafers used to fabricate semiconductor electrodes are shown in Table 1 as well. Notations of a, b and c were categorized by resistivities: a was within 1 - 10 Ωcm, b was 0.5 - 1.5 Ωcm, and c was 0.001 - 0.005 Ωcm.

Table 1. Labels and specifications of p-Si wafers used to fabricate semiconductor electrodes.

Label	Surface	Resistivity (Ωcm)	Thickness (μm)	Vendor
100a	(100)	1 - 4	200	ITME
100b	(100)	0.5 - 1.5	355 - 405	ElCat
100c	(100)	0.001 - 0.005	380 ± 52	ITME
110a	(110)	2 - 4	355 - 405	ElCat
111a	(111)	3 - 6	380 ± 25	ITME

To fabricate semiconductor electrodes, p-type silicon wafers were cut to 5 mm by 5 mm with a diamond scribe. The cut silicon semiconductor chips were cleaned to remove organic residues by industrial standard RCA–1 cleaning procedure followed by RCA–2 etching procedure [40].

Ga-In eutectic (Aldrich, 99.99+%) was brushed onto the completely cleaned and etched silicon surface to achieve an ohmic contact with an electric wire, which was attached by conductive silver epoxy (Circuitworks, CW2400) [35].

The side with the electric wire became the back side of the electrode, whereas obverse was the electroactive electrode surface. The silver epoxy was cured for over 4 hours in oven at 70 °C. The exposed silver epoxy and silicon on the back side was completely covered by nonconductive epoxy resin (LOCTITE, 1C) to stabilize the wire and to confine the exposed area to the front, electrode surface. The nonconductive epoxy was allowed to set for 6 hours at 70 °C.

After the electric wire was attached on the back side of the silicon chip, the electrode surface was cleaned and etched again following the RCA-1 and RCA-2 procedures just before experiments were run. Some electrodes are modified with magnetic materials and unmodified electrodes were used as controls.

2.2.3 Preparation of Magnetically Modified
        Semiconductor Electrodes

For magnetically modified semiconductor electrodes, the electrode surfaces of
cleaned semiconductor electrodes were coated with a suspension of Nafion (3.60 μl;
Aldrich, 5 % wt/vol, 1,100 eqwt) that contained magnetic microparticles at 0%, 15%
and 20% v/v in suspension. The coatings were dried on the electrode surface within
an external magnetic field for 15% and 20% v/v magnetic modification and without
an external magnet for 0% modification to form a 6 μm-thick coating. The external
magnetic field was applied with an NdFeB ring magnet (o.d. = 3.0 in.; i.d. = 1.5
in.; and 0.5 in. thickness) placed around the electrode surface. Thickness of the
coating was estimated from literature values of densities of dried and fully hydrated
Nafion and of magnetic particles [41] as well as a density of Nafion suspension from
the manufacture's manual.

Fabricated electrodes were labeled as follows: "a labeling of p-Si wafer" / "a
symbol of coating material and magnetic particle content" / "a pH of a solution".
For example, an uncoated semiconductor electrode made with 100a wafer in pH 1
solution was labeled "100a//1"; if the electrode was coated with 15 % v/v magnetic
particles in Nafion, it was labeled "100a/M15". Then, if is 100a/M15 placed in a
solution of pH 13, it was labeled "100a/M15/13".

2.2.4 Experimental Set Up and Testing

A three-electrode electrochemical cell was used to measure the potential and
current profile for hydrogen evolution. The working electrode was a prepared

Figure 6. A photograph of a cell set up. A semiconductor electrode (green wire) is facing the fiber optic light guide. The fiber optic light guide is touching the window of the cell while the SE is placed at the blue line on the apparatus glass to fix the distance between them.

semiconductor electrode (0.25 cm^2), with or without magnetic modification. The counter electrode was a high surface area platinum wire mesh, and the reference electrode was a saturated calomel electrode (SCE). Potentials were reported versus SCE, unless otherwise noted.

A home made glass apparatus was used as the cell volume. The container cell had flat glass windows on the side and on the bottom. The working, reference and counter electrodes and an electrolyte solution were placed in the cell. The surface of the working electrode was faced toward either the bottom or side window. The output of a light guide was set touching the outside of the window of the cell where the working electrode was placed. The distance between the output of the light guide and a working electrode was carefully set at 1.2 cm by adjusting the clamp on the working electrode, Figure 6.
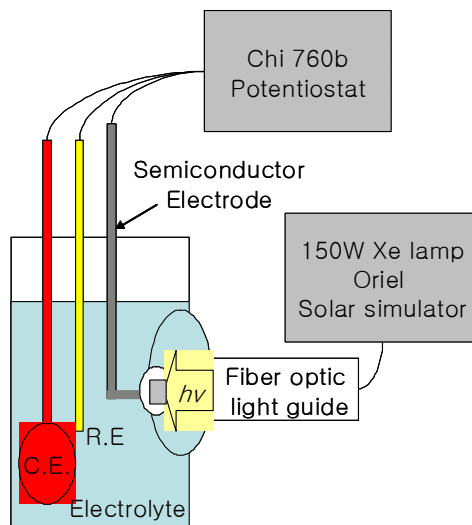
Figure 7. Schematic of the experimental setup.

A working electrode was irradiated by an Oriel 150 W Xe arc lamp solar simulator through the light guide. The working electrode was placed at the distance from the output of the light guide where the light intensity is 20 mW/cm^2. The light intensity was measured by a power meter (Thorlabs, PM10), Figure 7.

Linear sweep voltammograms (LSVs) were recorded with a potentiostat (CHinstrument 760b) to monitor current-potential profiles for the hydrogen evolution reaction on various electrodes in various electrolytes. The scan rate was 0.100 V/s and potential was swept within a 2 V to -2 V window from positive potential to negative potential so as to drive the proton reduction reaction. Open circuit potential measurements were performed with the same potentiostat.

2.2.5 Time-resolved Microwave Photoconductivity
        Measurements

Surface recombination rates are measured by time-resolved microwave

photoconductivity measurements. An intrinsic silicon wafer with a (111) crystallographic surface plane, resistivity of 1200 - 3000 Ωcm and thickness of 300 ± 29 μm was used for sample preparation. The wafer was cut approximately 1 cm by 1 cm and modified with only Nafion or magnetic particles (Simag-methyl, chemicell. GmbH) in Nafion suspension. The thicknesses of the modification are 6 μm. A total of six samples were prepared and three were modified with only Nafion and the other three were magnetically modified.

The photoconductivity measurement system was provided by Professor Stephen Maldonado at the University of Michigan, Ann Arbor. Excitation pulses were generated by a Continuum Minilite Nd:YAG laser operating at $\lambda = 1064$ nm with a full-width at half-maximum of <10 ns. A frequency of 24 GHz microwave was generated by a HP 8350B Sweep Oscillator with a 83570 A module. The reflected signal was detected by a Schottky detector connected to a Tecktronix TDS 1002B digital oscilloscope. The decays were fit with a single exponential function to determine the effective time constant for the lifetime of separated charges in the silicon wafers.

2.3   Results and Discussion

Effects of magnetic modifications of p-Si photocathode surfaces are demonstrated here. First, there is a magnetic effect consistent with pH. In pH 0 solution, the 100a/M15/0 photocathode shows maximum 6.2% light to chemical energy conversion efficiency. Second, it is shown that a magnetic effect is not surface crystallographic planes dependent. Third, doping level dependence on the magnetic modification

follows the general concept that when the doping level is too high and resistance is correspondingly too low, a semiconductor behaves like a metal and loses its photocathodic properties. Fourth, the magnetic particle loading experiments show protons extracted into Nafion enhance the proton concentration at the electrode and shift the band edge potentials as well as the flat band potential. When magnetic particles are included in the Nafion, the potential of the hydrogen evolution is shifted further to positive.

Furthermore, a comparison of hydrogen evolution on magnetically modified p-Si and on platinum electrodes with the same magnetic modification leads to the conclusion that the magnetic field is the larger effect as compared to the proton concentration effect of the Nafion. The magnetic field effect enhances the heterogeneous electron transfer rate by suppressing entropy of the electron spin and lowering the height of the activation energy barrier.

2.3.1 pH

To investigate the pH dependence of the hydrogen evolution reaction on a magnetically modified semiconductor electrode (MMSE) and a semiconductor electrode (SE), solutions of pH 0 and pH 1 are made with 1 M and 0.1 M HNO_3, respectively, and a pH 13 solution is made with 0.1 M NaOH. For the MMSE, 15 % v/v composite of magnetite microparticles in Nafion is coated on the surface of a p-Si electrode made with 100a p-Si wafer, labeled 100a/M15. The pH dependence of photohydrogen evolution on the 100a/M15 and the 100a/ as voltage is polarized and current is measured is shown in Figure 8 and some data are summarized in
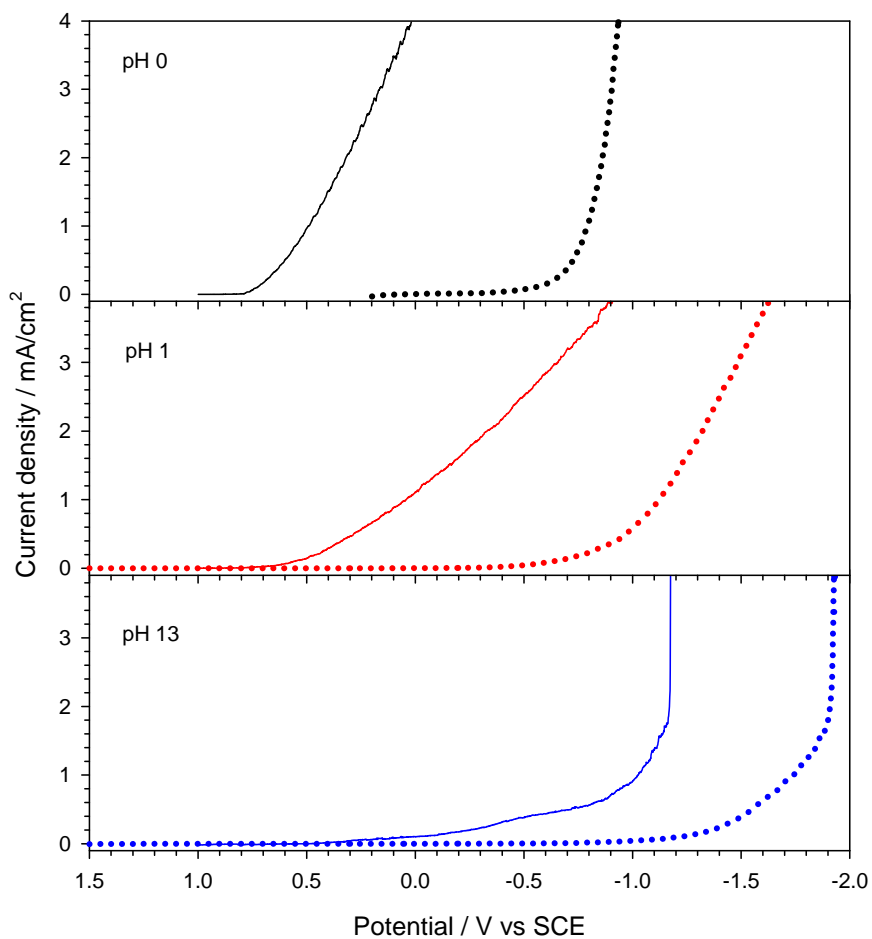
Figure 8. The pH dependence of hydrogen photoelectrochemical evolution on the 100a/M15/, and 100a// surfaces at pH 0, 1, and 13 under illumination. 100a/M15/s are solid lines and 100a//s are dotted. For better visualization on the linear sweep voltammograms, the same pH is coded the same color.

Tables 2 and 4.

In Figure 8 for pH 0, the onset of hydrogen evolution is measured at a current density of 0.2 mA/cm^2 for 100a/M15/0 (solid line) occurs at 0.689 V whereas the onset of hydrogen evolution of the 100a//0 (dotted line) occurs at -0.584 V. The onset potential of unmodified 100a//0 is 1.276 V more negative than that of magnetically modified 100a/M15/0.

For the magnetically modified electrode, there is no overpotential for hydrogen evolution. In general, unmodified p-Si has too high an overpotential to allow efficient hydrogen evolution as can be seen on the 100a//0. Whereas the overpotential on the 100/M15/0 is small enough to realize reasonable light conversion efficiency.

The onset potential of 100a/15M/0 is at more positive potential than the flat band potential typically measured on unmodified p-Si. Shifts in the flat band potential have been reported with solution pH and surface modification. The reported shifts with pH are typically measured as 30 - 90 mV/pH unit [42]. The large shifts here arises from both pH of solution and immobilization of protons in the Nafion matrix. Shift of band edge is illustrated in Figure 14 (page 41).

In the Figure 8 for pH 1, the onset of hydrogen evolution measured at 0.2 mA/cm^2 at the 100a/M15/1, solid line, is at 0.455 V whereas the onset of hydrogen evolution of the 100a//1, dashed line, also measured at 0.2 mA/cm^2 occurred at -0.771 V. The onset potential of unmodified 100a//1 is 1.226 V more negative than that of the modified 100a/M15/1. The current amplifier on the potentiostat overloaded at -0.6 V when current density reaches 4 mA/cm^2 for the 100a/M15/1, when the current density for the 100a//1 is approximately 20 fold lower. This markedly higher

Table 2. Potentials at certain current densities on various magnetically modified semiconductor electrodes.

	Experimental set up				E(V vs SCE) for hydrogen evolution at different current densities (mA/cm^2)			
surface	resistivity	Loading	pH	Label	0.2	1	2	3
(100)	a	15	0	100a/M15/0	0.689	0.492	0.318	0.165
(100)	a	15	1	100a/M15/1	0.455	0.042	-0.331	-0.656
(100)	a	15	13	100a/M15/13	-0.250	-1.025	-1.171	-1.174
(100)	c	20	0	100c/M20/0	-0.483	-0.895	-0.976	-
(100)	b	20	0	100b/M20/0	-0.092	-0.295	-0.401	-0.454
(100)	a	20	0	100a/M20/0	-0.146	-0.324	-0.533	-0.591
(110)	a	20	0	110a/M20/0	-0.106	-0.278	-0.38	-0.416
(111)	a	20	0	111a/M20/0	-0.134	-0.334	-0.339	-0.436

current for the MMSE is consistent with a significant increase in efficiency for the MMSE device.

Similar effects are observed in pH 13 basic solution. The reduction potential shifts to negative as expected by the Nernst equation and the flat band shift. In Figure 8 at pH 13, the onset of hydrogen evolution measured at 0.2 mA/cm^2 at the 100a/M15/13, solid line, is at -0.250 V whereas the onset of hydrogen evolution of the 100a//13, dashed line occurred at -1.359 V. The onset potential of the unmodified 100a//0 is 1.109 V more negative than that of the magnetically modified 100a/M15/13.

From the Nernst equation for hydrogen, a change in pH of 13 units should lead to a potential shift of about -0.6 V. Both MMSE and SE shift potential consistent with a Nernstian change in pH. At each pH, the MMSE shows onset of hydrogen evolution at 1.2 V positive of the corresponding SE.

By comparison of the linear sweep voltammograms (LSVs) of 100a/M15 and 100a/ at different pHs, the effect of magnetic microparticles modification on hydrogen

Table 3. Potentials at certain current densities on various Nafion modified semiconductor electrodes

			E(V vs SCE) for hydrogen evolution at different current densities (mA/cm^2)			
	Experimental set up					
surface	resistivity	Label	0.2	1	2	3
(100)	a	100a/M0/0	-0.575	-0.737	-0.794	-0.826
(100)	b	100b/M0/0	-0.515	-0.707	-0.780	-0.822
(100)	c	100c/M0/0	> -1	> -1	> -1	> -1
(110)	a	110a/M0/0	-0.370	-0.487	-	-
(111)	a	111a/M0/0	-0.321	-0.443	-0.486	-0.513

Table 4. Potentials at certain current densities on various semiconductor electrodes.

				E(V vs SCE) for hydrogen evolution at different current densities (mA/cm^2)			
	Experimental set up						
surface	resistivity	pH	Label	0.2	1	2	3
(100)	a	0	100a//0	-0.584	-0.748	-0.779	-0.823
(100)	a	1	100a//1	-0.771	-1.123	-1.322	-1.485
(100)	a	13	100a//13	-1.359	-1.743	-1.911	-1.923
(100)	b	0	100b//0	-0.683	-0.837	-0.890	-0.922
(100)	c	0	100c//0	-1.260	-1.489	-1.554	-1.591
(110)	a	0	110a//0	-0.673	-0.867	-0.942	-0.98
(111)	a	0	111a//0	-0.695	-0.88	-0.931	-0.96

evolution is evident. Moreover, the constancy of shifts in all range of pH supports that magnetic microparticles do not effect the concentration of hydrogen and protons in the Nafion matrix and that the effect of the magnets is on the fundamental electron transfer event as opposed to any associated chemical steps.

2.3.2 Crystallographic Plane

To study the effect of magnetic modification on crystallographic planes of the surfaces of the p-Si electrodes, working electrodes were prepared from 100a, 110a, and 111a wafers and 20 % v/v and 0% v/v (Nafion only) magnetic modification.

The resistivities of the 100a, 110a and 111a wafers were comparable within the range of 1 - 6 Ωcm so the effect of different crystallographic planes of their suffices can be studied. pH 0, 1 M HNO_3, solution were used as the electrolyte.

LSVs of 100a ,110a and 111a surfaces with /M20/, /M0/ and // (20 % v/v magnetic modification in Nafion, Nafion and unmodified) modification in pH 0 solution are illustrated in Figure 9. The figure is divided to three parts that are labeled corresponding to their crystallographic surface plane. Solid lines, dashed lines and dotted lines are LSVs with /M20/, /M0/ and // modification, respectively. For example, dashed line in Figure 9 (100) is 100a/M0/0. In Tables 2, 3 and 4, potentials of fabricated photocathodes at certain photocurrent densities are tabulated.

As can be seen in Figure 9, magnetic modification impacts all crystallographic planes of p-Si surfaces

The magnetically modified photocathodes (/M20/0) show that the photohydrogen evolution reaction occurs with 490 mV to 550 mV lower potential then unmodified photocathodes (//0) at 0.2 mA/cm^2 according to Tables 2 and 4. LSV shifts from //0 to /M20/0 are relatively constant, which indicates that no significant change of catalytic sites or reaction pathway occurs under magnetic modification.

LSV shifts for unmodified SE (//0) to Nafion modified SE (/M0/0) vary with surface crystallographic planes. For each surface orientation, the proton immobilized by Nafion may interact differently with each surface and the surface atomic densities. The atomic density on (100), (110) and (111) silicon surfaces are 6.18×10^{14} cm^{-2}, 9.59×10^{14} cm^{-2} and 15.66×10^{14} cm^{-2}, respectively [42].

The origin of the small plateau shown in the 100a/M20/0 at -0.4 V is thus far
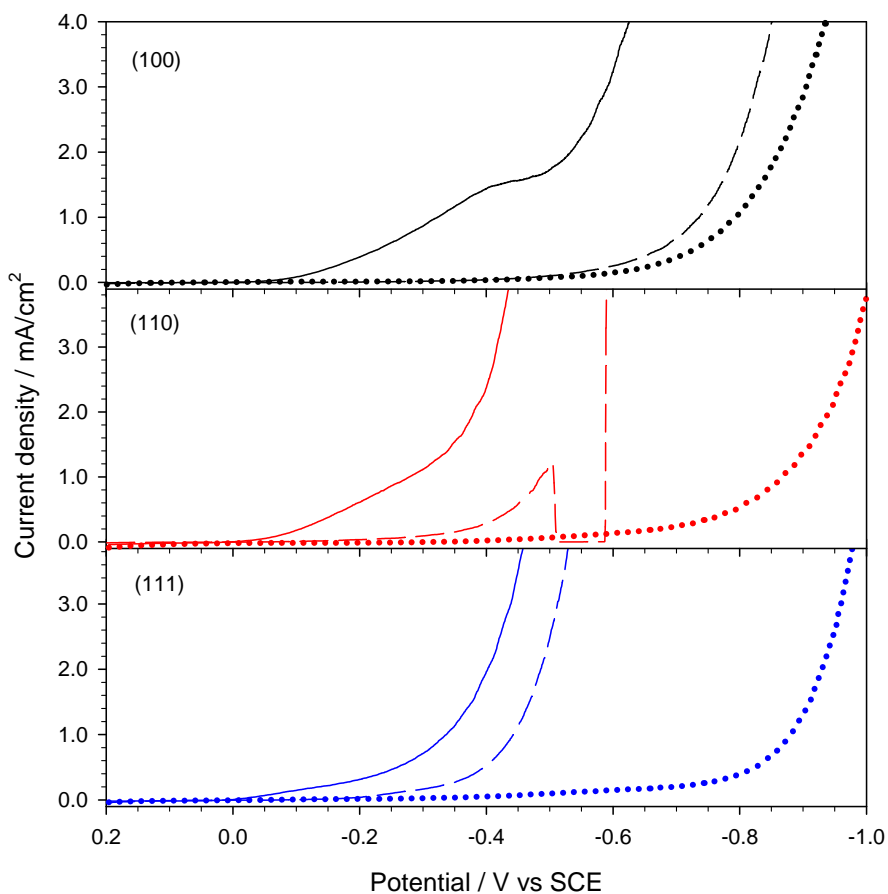
Figure 9. LSVs of photoelectrochemical hydrogen evolution on 100a/, 110a/, and 111a/ electrodes in pH 0 solution, 1 M HNO$_3$. Power of incident light on a surface of an electrode is 20 mW/cm^2. Labels correspond to the surface crystallographic plane. From top to bottom figures, solid lines are LSVs of 20 % v/v magnetic particle modified p-Si electrodes (100a/M20/0, 110a/M20/0, and 111a/M20/0). Dashed lines are Nafion modified p-Si electrodes (100a/M0/0, 110a/M0/0, and 111a/M0/0). Dotted lines are p-Si electrdoes (100a//0, 110a//0, and 111a//0).

unknown. The sharp drop of current on 110a/M0/0 is when light illumination is cut to show how the current varies when there is no light.

2.3.3 Doping

The effect of magnetic modification on the doping levels of p-Si photocathodes was studied by fabricating photocathodes with different resistivities and studying photocurrent potential profiles of the photohydrogen evolution reaction.

Wafers of 100a, 100b, and 100c were used to fabricate the p-Si electrodes and /M20/, /M0/ and // modifications were applied. As described in Table 1, 100a, 100b and 100c had resistivities of 1 - 4, 0.5 - 1.5, and 0.001 Ωcm, respectively, and the same crystallographic surface plane. pH 0, 1 M HNO_3, solution was used as the electrolyte.

LSVs of 100a//, 110b// and 111c// with /M20/, /M0/ and // modifications in pH 0 solution are illustrated in Figure 10. The Figure is divided into three parts that are labeled corresponding to their doping levels. Solid lines, dashed lines and dotted lines are LSVs with /M20/, /M0/ and // modification, respectively. For example, the solid line in Figure 10 (b) is 100b/M20/0. In Tables 2, 3 and 4, potentials of fabricated photocathodes at certain photocurrent densities are tabulated.

In Figure 10, magnetic modification is shown to impact all doping levels. When resistivity decreases (doping level increases) from 1 - 4 Ωcm to 0.5 - 1.5 Ωcm, that is 100a/M20/0 and 100b/M20/0 respectively, the current voltage profile is almost the same as their resistivities (Ωcm) are similar. However, when resistivity decreases to 0.001 Ωcm, 100c/M20/0 shows little semiconductor photoelectrochemical behavior.

Table 5. Potentials of 100a electrodes with various modifications when photocurrent density at 0.2 mA/cm^2. Electrolyte is pH 0, 1 M HNO$_3$ solution.

Loading contents (v/v %) on an 100a/	100a	100a/M0	100a/M15	100a/M20
E(V) at 0.2 mA/cm^2 in pH 0	-0.584	-0.397	0.689	-0.146

At this low resistivity, p-Si loses its semiconductor properties and behaves more like metal.

2.3.4 Magnetic Particle Loading

The effect of magnetic particle loading contents was investigated by comparing LSVs of 100a//0, 100a/M0/0 and 100a/M20/0 in Figure 9 (100) and 100a/M15/0 in Figure 8. For convenience, some data were tabulated in Table 5. These LSVs were run under the same experimental conditions except the magnetic particle content varied.

When the modification is 100/M0, Nafion with a thickness of 6 μm was coated on the surface. In Figure 9 for (100), the Nafion only coated photocathode (100a/M0/0), shows enhanced photocurrent voltage profile for the photohydrogen evolution compared to the unmodified photocathode, 100a//0. Nafion is a well known proton exchange polymer and provides a large number of immobilized proton at the electrode surface. Band-edges on the surface of a semiconductor electrode are known to shift with immobilized or adsorbed charged species. Therefore, the impact on the photocurrent voltage profile of Nafion as compared to unmodified p-Si is as expected [43].

The magnetically modified 100a/M15/0 and 100a/M20/0 exhibit enhanced
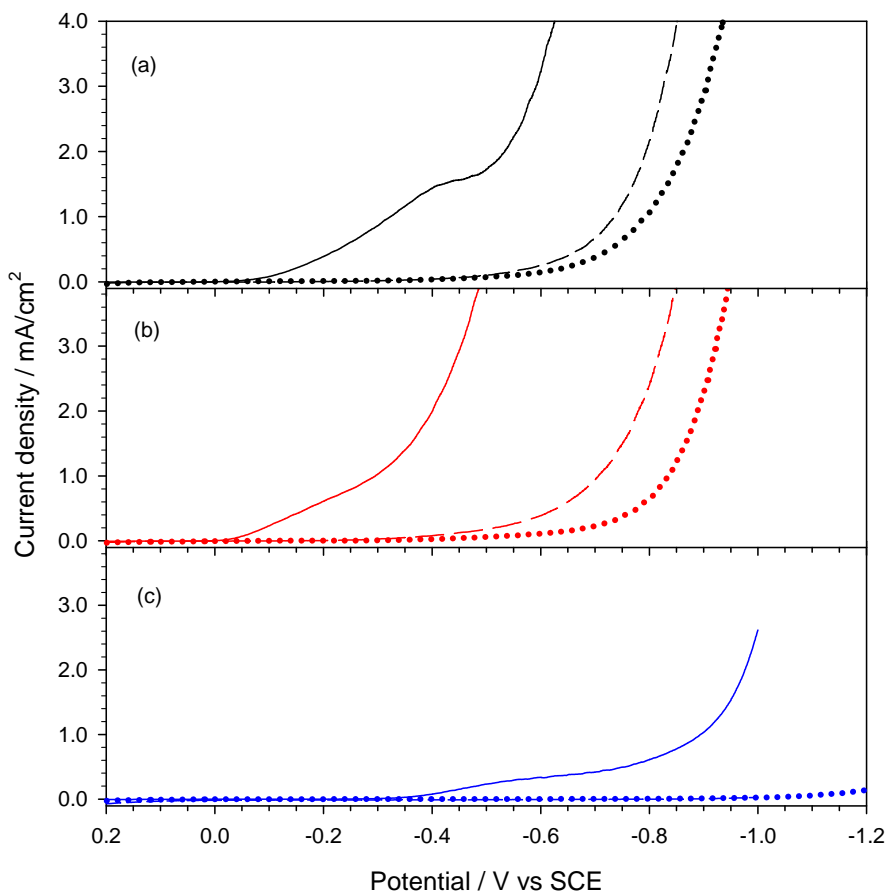
Figure 10. LSVs of photoelectrochemical hydrogen evolution on 100a/, 100b/, and 100c/ electrodes in pH 0 solution, 1 M HNO$_3$. Power of the incident light on the electrode surface of an electrode is 20 mW/cm^2. Labels correspond to doping level label 100a for (a), 100b for (b) and 100c for (c) and they have resistivities of 1 - 4, 0.5 - 1.5, and 0.001 Ωcm, respectively. From top to bottom figures, solid lines are LSVs of 20 % v/v magnetic particle modified p-Si electrodes (100a/M20/0, 100b/M20/0, and 100c/M20/0). Dashed lines are Nafion modified p-Si electrodes (100a/M0/0, 100b/M0/0, and 100c/M0/0). Dotted lines are p-Si electrdoes (100a//0, 100b//0, and 100c//0).

current output compared to the 100a/M0/0. This enhancement is solely due to magnetic particles. The maximum performance is achieved when the magnetic particle content is 15 % v/v in Nafion as seen in Figure 8 and Table 5. Because magnetic particles are coated on the electrode surface where light comes in, magnetic microparticles themselves block the pathway of the incident light and attenuate light energy actually hitting the electrode surface.

The measured power density of light after passing through 20% v/v magnetic particle in Nafion on a glass is 9 % less than that after passing through 15% v/v magnetic particle in Nafion.

2.3.5   Modification of a Pt Electrode

To confirm that improved photocurrent voltage profiles are not due to a change of proton concentration under a magnetic modification, Pt electrodes were modified with 20 % magnetic microparticles by the same procedure as the semiconductors. Current potential profiles of magnetically and Nafion only modified Pt electrodes as well as a bare Pt electrode were recorded, respectively. A typical three-electrodes cell in a 1 M nitric acid solution was used with saturated hydrogen established with hydrogen purging.

Results are shown in Figure 11 as current potential profiles of hydrogen evolutions on Pt, magnetically modified Pt (Pt/M20/0) and Nafion modified Pt (Pt/M0/0) electrodes. As can be seen in the figure, these three electrodes have very similar current potential characteristics. Magnetic and Nafion modifications do not affect the ratio of proton and hydrogen activities significantly. Consequently, open circuit
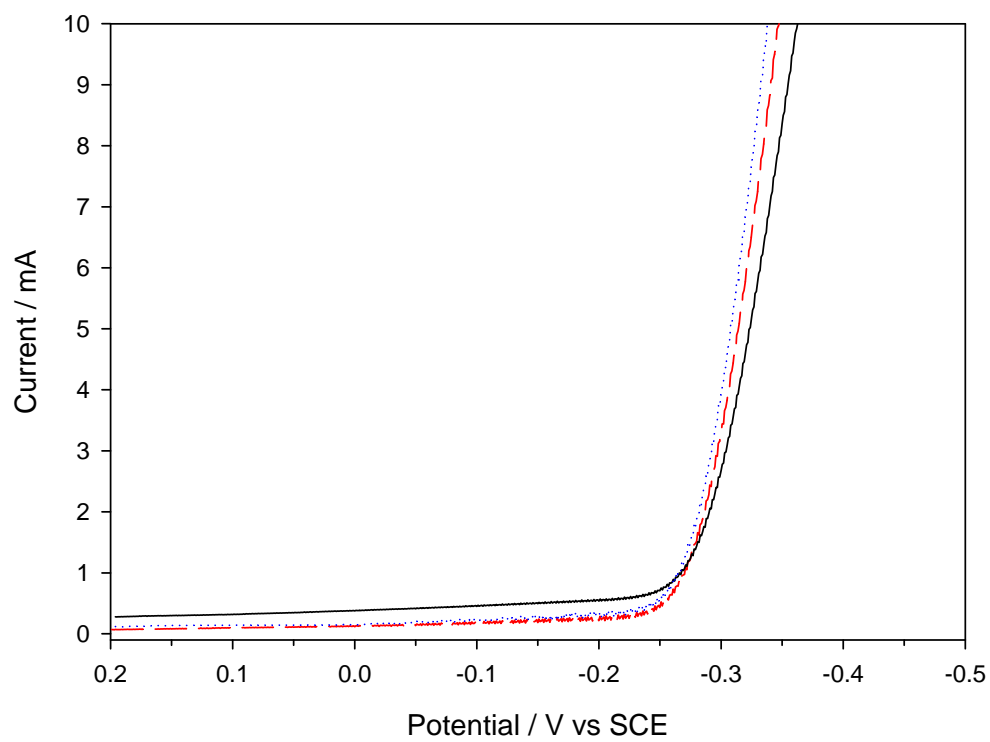
Figure 11. LSVs of hydrogen evolution on unmodified Pt (dashed red), magnetically modified Pt (Pt/M20/0, solid black), and Nafion modified Pt (Pt/M0/0, dotted blue) in 1 M HNO$_3$ with hydrogen purging.

Table 6. Open circuit potential of 1M nitric acid solution with hydrogen purging on Pt electrodes.

	V_{oc} versus SCE	V_{oc} versus NHE
Pt/0	-0.251	-0.009
Pt/M0/0	-0.255	-0.013
Pt/M20/0	-0.256	-0.014

potential measurements shown in Table 6 also shows very similar values for the three electrodes. The ratio of proton and hydrogen concentrations is not altered by the magnetic modification. Further, a change in the ratio would affect the equilibrium. Magnetic effects on thermodynamics at room temperature are negligible. Magnetic effects are only through dynamics.

2.3.6 Energy Conversion Efficiency

Confirmation of the impact of magnetic modification is found in calculation of the light energy conversion efficiency. To evolve hydrogen on the p-Si photocathode without magnetic modification in either acidic or basic solution, potential lower than the thermodynamic potential for hydrogen evolution on a platinum electrode is needed, so the efficiency calculation yields a negative result.

Efficiencies are calculated from Equation 6. Efficiency profiles for 100a/M15/0 (solid line), 100a/M15/1 (dotted line), and 100a/M15/13 (dashed line) are shown in Figure 12. At pH 13, the maximum efficiency at 100a/M15/13 is lower than for 100a/M15/0 and 100a/M15/1/, and corresponds to significant photocurrent at potential negative of 0 V. Maximum photoconversion efficiency of 1.8 % is achieved
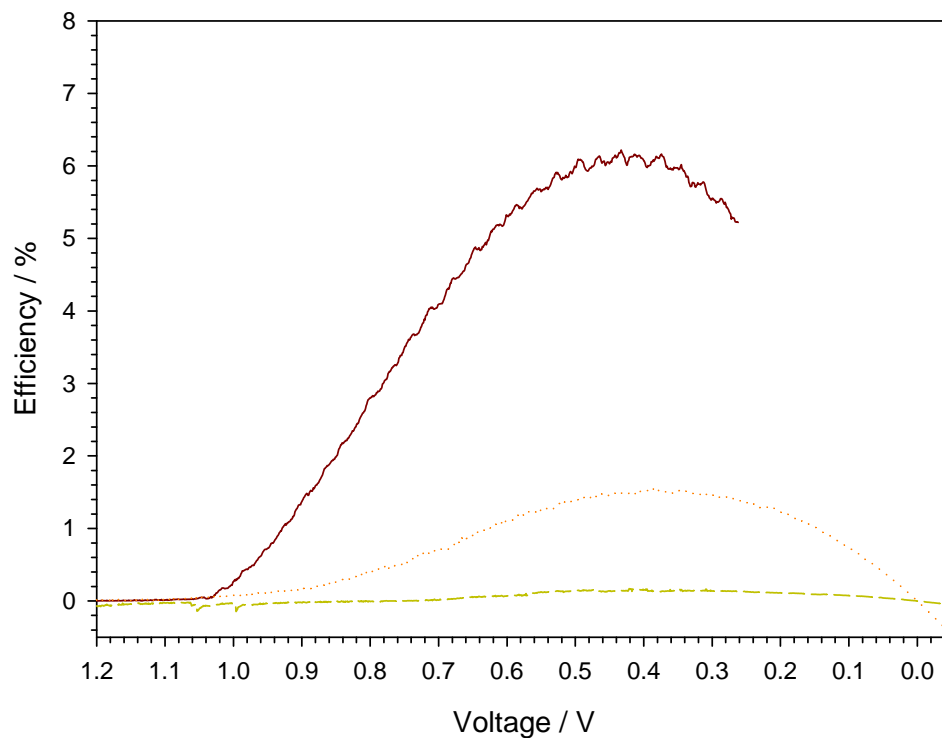
Figure 12. The calculated efficiency profiles of the 100a/M15/0 (solid line), 100a/M15/1 (dotted line), and 100a/M15/13 (dashed line). The efficiency (η) and voltage (V) are defined as in Equation 7.

at 0.80 mV of applied voltage (V) for the 100a/M15/1. An efficiency of 6.2 % is achieved at 0.42 V of applied voltage (V) for the 100a/M15/0.

2.3.7 Impacts of Magnetic Modification on p-Si Electrodes

Here, possible mechanisms for observed enhancements under magnetic modification are discussed. A schematic view of potentials and current at the p-Si|electrolyte junction is shown in Figure 13 and at the modified p-Si|electrolyte junction in Figure 14. Four important parameters determine the performance of a
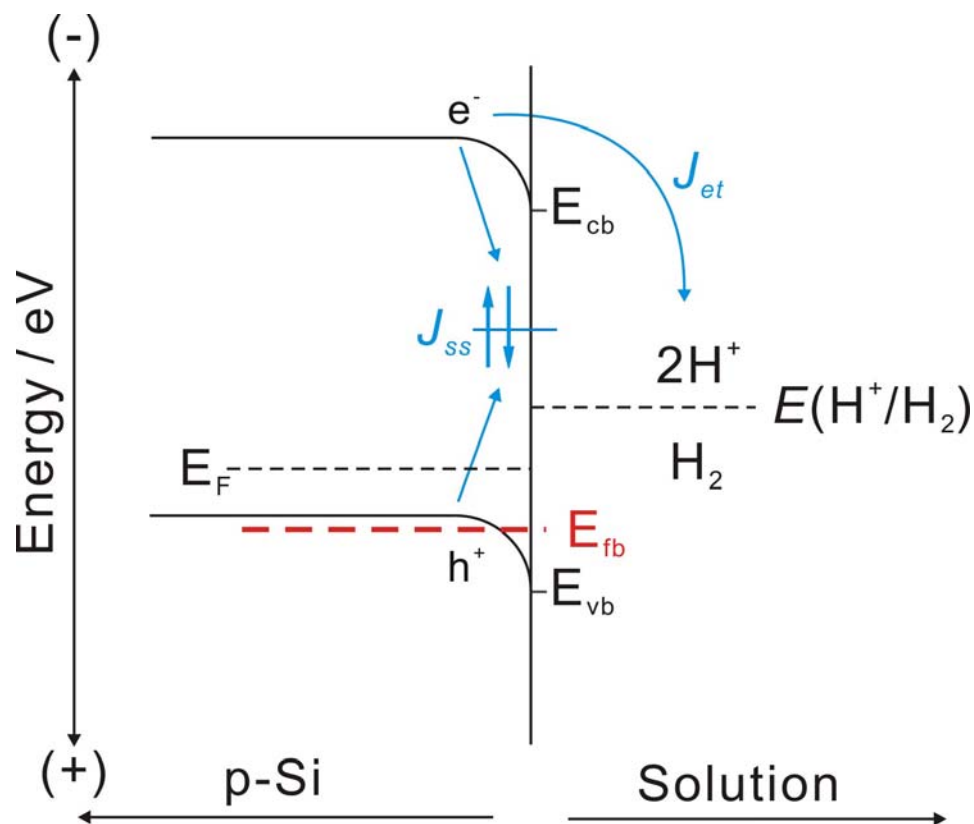
Figure 13. Energy and current flow diagram of p-Si and solution interface for the photoelectrochemical HER.

photoelectrochemical cell: the reduction potential of the redox couple (E), the flat band potential of the semiconductor (E_{fb}), the surface recombination rate (J_{ss}), and the heterogeneous electron transfer rate (J_{et}).

The flat band potential is the potential at which the valence and conduction band potentials are flat; there is no potential gradient in the semiconductor at the semiconductor solution interface. The surface recombination reaction is the process by which light generated electrons and holes recombine at the defect sites of the electrode surface. The electron and hole are lost to driving a useful reaction and the photo triggered charge separation does not contribute to cell efficiency.

The energy gap between the flat band potential (E_{fb}) and the reduction potential of the redox couple (E) sets the maximum energy the system can produce. The surface recombination rate (J_{ss}) and the heterogeneous electron transfer rate (J_{et}) dominate system dynamics. Fast surface recombination rates (J_{ss}) and slow heterogeneous electron transfer rates (J_{et}) are the major factors that diminish photocurrent (J_p).

Nafion modification allows band edges, E_{cb} and E_{vb}, to shift toward positive potentials. The band edge potential shift leads to a more positive flat band potential (E_{fb}) as shown in Figure 14. The shift in the flat band leads to a larger difference in E_{fb} and E. Then, more energy is derived from the cell.

One fundamental question is whether spin states of the recombination sites can be affected by the magnetic field so as to change surface recombination rate (J_{ss}). A second question is whether magnetic fields impact the rate of photocurrent driven heterogeneous electron transfer (J_{et}) to proton adsorbates on the p-Si surface. Schematics of the two currents, J_{ss} and J_{et}, are drawn in Figure 14 for the hydrogen reduction reaction.

In addition to possible magnetic effects on surface recombination and heterogeneous electron transfer, it is known that Nafion provide charges to the surface of p-Si that increases the energy available from the cell.

Flat band potential, E_{fb}, shifts with Nafion modification. Nafion coating can provide immobilized charge on p-Si electrodes. It is known that band edges shift with pH. When silicon is placed in a low pH solution, band edges of the silicon shift to more positive potential. p-Si 5 Ωcm in 1 M H_2SO_4 has a reported flat band
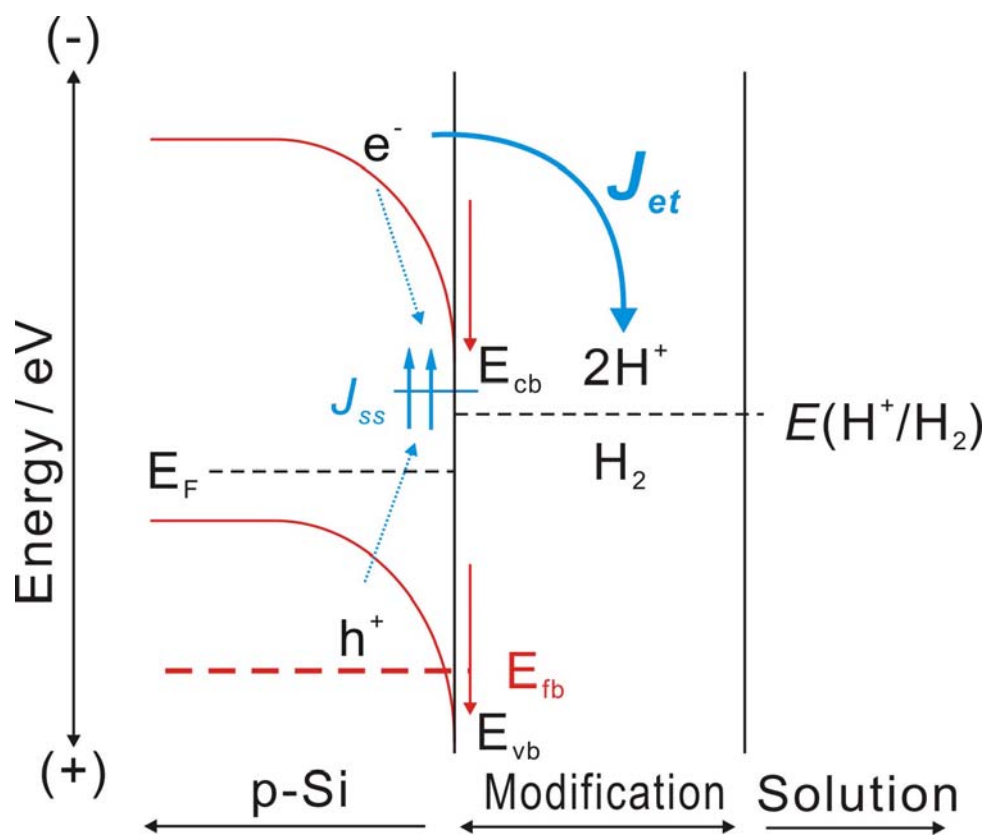
Figure 14. Energy and current flow diagram of p-Si, modification and solution interfaces for the photoelectrochemical HER.

potential of 0.35 V vs SCE [42]. The flat band potential also shifts toward a positive potential with immobilized positively charged ions on the surface [43]. Because Nafion can provide immobilized protons to the surface, band edges shift to positive potential.

Considering the hydrogen reduction reaction

$$2\text{H}^+ + 2\text{e}^- \rightleftarrows \text{H}_2 \tag{9}$$

the means for increasing the rate of the HER are to increase H^+ concentration, increase electron concentration, eliminate hydrogen, and catalyze the reaction rates. The concentrations of protons and electrons and the rate of the reaction are discussed below. The hydrogen concentration is largely invariant in the Nafion matrix.

The onset potential for magnetically modified electrodes shifts 1.2 V from bare electrode for pH across the range 0 to 13. From the platinum electrode modification experiments, it is confirmed that magnetic modification does not change the concentration of H^+ at the electrode surface. Magnetic modification does not increase the concentration of photogenerated electrons. If magnetic modification increases photogenerated electrons, increased magnet loading would increase photocurrent, but it is found that 20% loading blocks light and efficiency is reduced, consistent with fewer photogenerated electrons.

Therefore, the supply of the reactants, proton and photogenerated electrons, in the reaction Equation 9 are not affected by magnetic modification. The basic mechanism in Equation 9 and the catalytic sites are not altered by magnetic particles. It is concluded that the magnetic field impacts the kinetic rates instead of

component concentrations.

There are two kinetic procedures impacting reaction rates, surface recombination rate and heterogeneous electron transfer rate. Measurements by time-resolved microwave photoconductivity show that the surface recombination rate at magnetically modified silicon is the same as Nafion modified silicon. The magnetic fields enhance the rate of heterogeneous electron transfer. A magnetic field effect on heterogeneous electron transfer is demonstrated for non-catalytic electrodes, as presented in the next Chapter. Magnetically facilitate heterogeneous electron transfer to carbon monoxide adsorbate on platinum electrodes has also been observed [2].

2.3.8 Surface Recombination Rate Measurements

Because, in a semiconductor, microwave power absorbance changes with the amount of excess charge carriers, the amount of photogenerated excess charges can be recorded by monitoring the power of microwaves that are reflected or penetrated the semiconductor. A time-resolved microwave photoconductivity measurement includes monitoring reflected microwaves from a semiconductor while applying excitation laser pulses to the semiconductor [44].

Time-resolved microwave photoconductivity measurements of intrinsic silicon, Nafion modified intrinsic silicon, and magnetically modified intrinsic silicon are shown in Figure 15. Intrinsic silicon is undoped single crystal (100) silicon. The curves in the Figure 15 map the decay of charge carriers. The lifetime of charge allows assessment of the surface recombination rate. The exponential decay is

modeled as follows.

$$\frac{\Delta P}{P} = \exp\left(-\frac{t}{\tau}\right) \tag{10}$$

$$\log\left(\frac{\Delta P}{P}\right) = -\left(\frac{1}{\tau}\right)t$$

$$\frac{1}{\tau} = \frac{1}{\tau_{bulk}} + \frac{S}{2d}$$

$$\simeq \frac{S}{2d}$$

$$S = \frac{2d}{\tau} \tag{11}$$

where t, τ, τ_{bulk}, $\Delta P/P$, S and d correspond to time (s), time constant (s), bulk recombination time constant (s), normalized signal, surface recombination rate (cm/s) and thickness of the semiconductor $(3.00 \pm 0.25 \times 10^{-2}$ cm), respectively. The y-axis in Figure 15 is normalized intensity of reflected microwave power and the x-axis is time in seconds. Decay of the reflected microwave intensity is described by Equation 10.

Figure 16 is a semi-log plot of the results, where the slope for each sample is the inverse time constant $(1/\tau)$. Steeper slopes have smaller time constants, which corresponds to faster surface recombination rates.

Surface recombination rates can be calculated directly from the time constant calculated from Equation 11. The values are tabulated in Table 7.

The result shows that magnetically modified Si and Nafion modified Si have longer lifetimes than unmodified Si wafer.

Because Figure 16 did not show excellent linearity, a non-linear fit to the data in
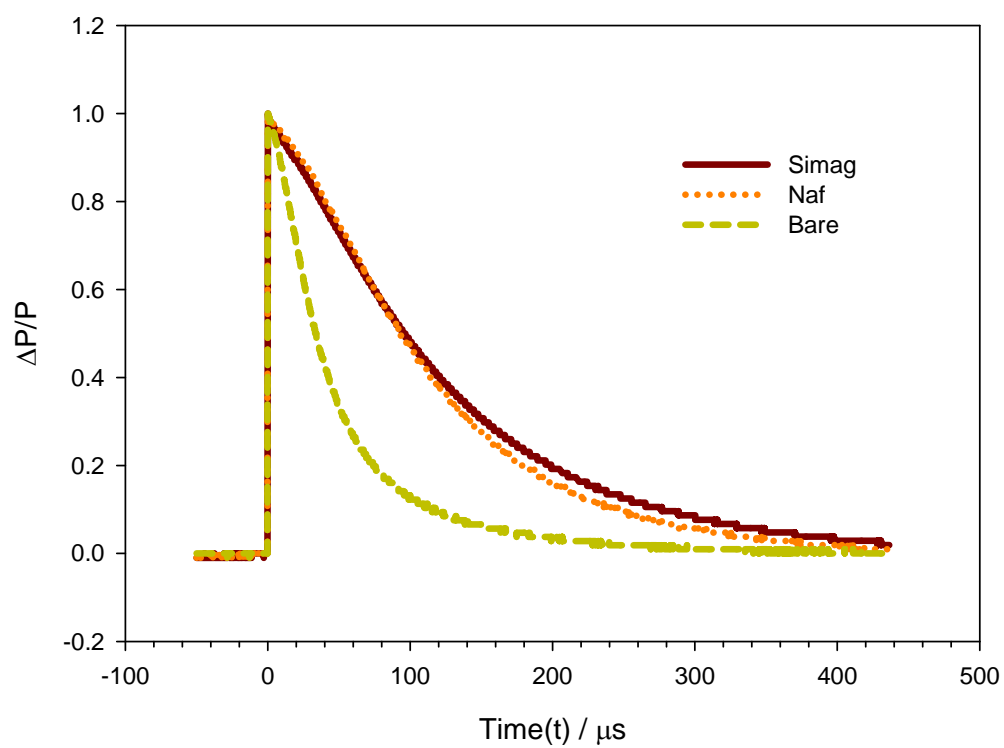
Figure 15. Time-resolved microwave photoconductivity measurents. The y-axis is the normalized intensity of the reflected microwave power and the x-axis is time (s). The magnetic microparticle Nafion suspension coated Si electrode and Nafion coated Si electrode show similar and longer lifetime than the unmodified Si electrode.
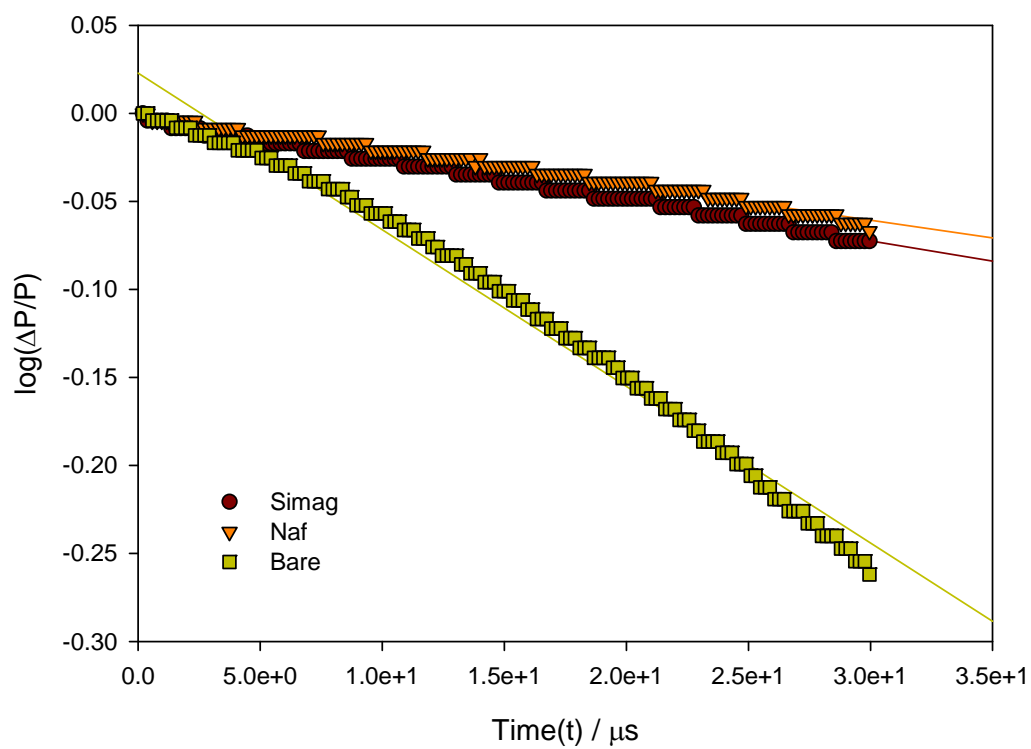
Figure 16. Logarithm of normalized intensity versus time plot. Slopes can be directly converted to time constants such that surface recombination rates can be calculated.

Table 7. Surface recombination rate of Si, Nafion coated Si and magnetically modified Si electrode caculated from nonlinear fittings.

	-a($-1/\tau$)	R^2	S (cm/s)
Si	-21290±50	0.9976	1300±200
Nafion coated Si	-9160±30	0.9964	550±90
Simag modified Si	-8230±10	0.9985	490±80

Figure 15 was also performed using equation

$$y = b \exp(-ax)$$

From the calculated surface recombination rates, Nafion coated Si and magnetically modified Si show similar rates, 490±80 and 550±90 cm/s and the unmodified Si has a surface recombination rate of 1270±210 cm/s. Nafion on the silicon electrode surface diminishes surface trap sites and provides higher proton concentration on the surface. Most importantly, no impacts of magnetic fields on surface recombination rates are found.

2.3.9 Heterogeneous Electron Transfer Rates

The impact of magnetic modification on the heterogeneous electron transfer rate for HER on p-Si can be estimated from the potential shift of the magnetic particles relative to the analogous Nafion modified Si. HER proceeds through an adsorption reaction and, crudely, the voltammetry is based on thin layer response with little change in a symmetry of the barrier.

The difference in potentials at the same current density can be used to estimate the ratio of electron transfer rates. Let E_M and E_N be the potential for a given

Table 8. Ratio of estimated heterogeneous electron transfer rates for magnetically and Nafion modified p-Si electrodes.

		$\ln\left(k_M^0/k_N^0\right)$ and k_M^0/k_N^0 at different current densities (mA/cm^2)			
	Label	0.2	1	2	3
$\ln\left(k_M^0/k_N^0\right)$	100a/M15	24.610	23.929	21.651	19.295
	100a/M20	8.352	8.041	5.082	4.575
	100b/M20	8.232	8.018	7.375	7.161
	110a/M20	5.137	4.067		
	111a/M20	3.639	2.121	2.861	1.498
k_M^0/k_N^0	100a/M15	4.88×10^{10}	2.47×10^{10}	2.53×10^{9}	2.40×10^{8}
	100a/M20	4.24×10^{3}	3.11×10^{3}	1.61×10^{2}	9.71×10^{1}
	100b/M20	3.76×10^{3}	3.76×10^{3}	1.60×10^{3}	1.29×10^{3}
	110a/M20	1.70×10^{2}	5.84×10^{1}		
	111a/M20	3.81×10^{1}	8.34	1.75×10^{1}	4.47

current density on a magnetically modified electrode and on analogous Nafion filmed electrode. Then, the corresponding heterogeneous electron transfer rates k_M^0 and k_N^0 are

$$E_M - E_N \sim \frac{RT}{\alpha F} \ln \frac{k_M^0}{k_N^0} \tag{12}$$

If the transfer coefficient α is approximated as 0.5 and $F/RT = 38.92$ V^{-1}, then

$$\frac{k_M^0}{k_N^0} = \exp\left[\frac{\alpha F}{RT}\left(E_M - E_N\right)\right] = \exp\left[\left(E_M - E_N\right) 19.47\text{V}^{-1}\right] \tag{13}$$

Some results are tabulated for 100a/M15/0 and 100a/M20/0 with 100a/M0/0 in Table 8. This approximation yields about an order of magnitude estimate.

At the foot of the waves, where current density is low and heterogenous kinetic limitations are largest, the 20 % magnet loading increases the rate of the heterogeneous electron transfer where k_{M15}^0/k_N^0 is 4.24×10^3 at 0.2 mA/cm^2. For 15 % magnetic loading, the enhancement is substantially larger, k_{M20}^0/k_N^0 is 4.88×10^{10} at 0.2 mA/cm^2. At higher current density and more extreme applied

voltages, the kinetic limitation are somewhat mitigated by the driving force of the applied potential. In all cases, the magnetic effect remains substantial, such that $\ln(k_M^0/k_N^0)$ is lowered from 3.777 to 5.315.

Potential sweep voltammograms of hydrogen evolution on noncatalytic electrodes confirm that magnetic field effects primarily impact heterogeneous electron transfer rates. Simulations of the measured LSVs give relative kinetic parameters where 10^2 - 10^4 times faster k^0 is found for magnetically modified electrode than for unmodified electrodes. Details are described in Chapter 4.

2.4   Conclusion

In this study, a series of p-Si electrodes with various doping levels and surface crystallographic planes were prepared. Some electrodes were modified with composites of magnetic microparticles and Nafion. For the magnetically modified semiconductor electrodes (MMSEs), various loadings of magnetic microparticles were used. For the magnetically modified and unmodified electrodes, the photoelectrochemical hydrogen evolution reaction was tested by linear sweep voltammetry under light and dark condition and with electrolytes at several pH values.

Magnetic modification of p-Si increased reaction rates and enabled direct hydrogen production from light. A maximum energy conversion efficiency of 6.4 % was achieved when p-Si with (110) surface and doping level of 1 Ωcm was modified with a composite of 20 % magnetic particles in Nafion in pH = 0 electrolyte. From the tests of doping level, magnetic particle loading, surface crystal orientation, and

pH, it is demonstrated that a p-Si with resistivity of 0.5 to 1.5 Ωcm modified with 15 % magnetic particles in Nafion pH = 0 electrolyte facilitates hydrogen evolution.

From measurements of time-resolved microwave photoconductivity, HERs on magnetically modified and unmodified non-catalytic electrodes and platinum electrodes, it is confirmed that the observed effect arises from enhanced heterogeneous electron transfer kinetics between an electrode surface and the adsorbates by the magnetic modification and not proton concentration.

Although magnetic modification of p-Si dramatically improves the slow kinetics of photoelectrosynthetic hydrogen evolution, stability issues of coatings remain, and must be resolved before practical devices are possible to generate hydrogen from sunlight.

CHAPTER 3

MAGNETIC FIELD EFFECT ON HETEROGENEOUS ELECTRON TRANSFER

In this thesis, magnetic field effects on photoelectrochemical hydrogen evolution reaction (HER) on silicon electrodes and self exchange reactions of transition metal complex redox couples at Nafion modified electrodes are discussed.

As to fundamental causes of this effect on semiconductor electrodes (SE), we speculated that two processes are impacted by magnetic fields in the photoelectrochemical reaction on semiconductor electrodes: the surface recombination rate and the heterogeneous electron transfer rate. It has been demonstrated that the improved photoelectrochemical responses at magnetically modified semiconductor electrodes (MMSE) are not due to inhibition of surface recombination rates; this is based on the results of time-resolved microwave photoconductivity measurements.

On a platinum electrode, hydrogen evolution is catalytic and the heterogeneous electron transfer rate is reversible, which means the electron transfer is fast relative to the rate of the measurement. Therefore, further enhancement of the electron transfer rate cannot be measured under the current experimental conditions. HERs on magnetically modified, Nafion only modified and unmodified platinum electrodes are shown in Figure 11. The current voltage profile of HERs on these three electrodes are the same and confirm that differences in rates of heterogeneous electron transfer kinetics are not observed on catalytic electrodes. However, on noncatalytic electrodes, hydrogen evolution reaction kinetics are quasireversible to irreversible and differences in electron transfer kinetics can be measured. Here,

increases in the heterogeneous electron transfer rates are achieved through magnetic modification.

In this Chapter, the electrochemistry of the HER on noncatalytic electrodes are evaluated to study magnetic field effects (MFEs) on heterogeneous electron transfer rates. For control experiments, noncatalytic electrodes are modified with either Nafion or magnetic microparticles in Nafion. The noncatalytic electrodes studied are n-type gallium arsenide electrodes (nGaAsE) and glassy carbon electrodes (GCE). n-GaAs has electrons as the majority carrier and does not have a photoresponse for cathodic reactions and thus behaves as a noncatalytic electrodes for HER. Glassy carbon is also a noncatalytic electrode for the HER. GC is extensively used as an electrode because of its wide potential window in water. Unlike noble metal electrodes, GC exhibits no metal|oxidation voltammetry.

3.1   Experimental

nGaAsEs were fabricated in the same manner as p-Si electrodes, as described in Chapter 2. n-GaAs wafers with tellurium (Te) doping, (100) crystallographic surface plane, 450 ± 25 μm thickness, and 2.5×10^{-3} Ωcm resistivity where both side polished were purchased from SEMI. The wafers were cut to 5 mm by 5 mm and cleaned using the RCA-1 procedure to remove organic residuals. The cleaned chips were etched with 1% Br_2/CH_3OH solution (HF was used for p-Si). To establish ohmic contact, a drop of 1 mM chloroauric acid solution was applied to one side of the n-GaAs chip and allowed to sit for 20 minutes. This side became the back side of an electrode. Residuals were flushed with deionized water three times and the chip was

dried in air. Silver epoxy was used to contact wires on the back side of electrodes and Loctite nonconductive epoxy was applied to cover the exposed silver epoxy. For GCEs, glassy carbon rotating disc electrodes with 0.5 mm diameter were used after polishing.

The prepared noncatalytic electrodes, nGaAsEs and GCEs, were magnetically modified or modified with only Nafion. Magnetic modification involved application of a mixture of magnetic microparticles and Nafion suspension (15 % v/v) directly onto the electrode surface. Magnetic microparticles of iron oxide (Fe_3O_4, Aldrich) with a silane coating were prepared according to the method described in Chapter 2. Nafion modification involved coating electrode surfaces with only the Nafion suspension (Ion Power). The coating thickness was controlled to be 6 μm, based on the calculated total volume of dried Nafion. A density of 1.95 g/cm^3 was used [45].

The three-electrode electrochemical cell included using a saturated calomel electrode (SCE) as the reference electrode and a platinum mesh as the counter electrode. Nitric acid (1.00 M) was used as the electrolyte. Solutions were not degassed. Potential sweep voltammograms of hydrogen evolution reaction were recorded using a CH Instrument model Chi760b potentiostat/galvanostat.

3.1.1 Computer Simulation

To compare rate constants of magnetically modified and to only Nafion modified glassy carbon electrodes, current voltage profiles were fitted to a computer simulation. The computer simulation was based on semi-infinite linear diffusion condition and the Butler-Volmer model for electron transfer kinetic model. The

Table 9. Parameters used in the computer simulation.

E_{init}	Initial potential (V)
E_f	Final potential (V)
A	Electrode surface area (GC: 0.785, nGaAs: 0.25, p-Si: 0.25 cm^2)
Frx Conc	Fractional concentration: 1
υ	Scan rate (0.1 V/s)
T	Temperature (298 K)
t_k	Maximum characteristic time: $2\left(E_f - E_{init}\right)/\upsilon$ or $1/nf\upsilon$
C	Concentration (1.5 mole/cm^3)
E^0	Standard redox potential: -2.42 V vs SCE
α	Transfer coefficient
D_i	Dimensionless diffusion coefficient: $D\Delta t/\left(\Delta x\right)^2$
X_0	Dimensionless standard heterogeneous electron transfer rate: $k^0\sqrt{t_k/D}$
n	Number of electron
k^0	Standard heterogeneous rate constant
D	Diffusion coefficient (5.00×10^{-5} cm^2/s)
$j_{\max}$	Maximum spatial index: $1 + 6\sqrt{D_i k_{\max}}$
$k_{\max}$	Total number of time steps in the simulation: 300

simulation was coded in Visual Basic programming language in Microsoft Excel 2003.
The code was shown in Appendix C. Table 9 includes explanations of parameters
used in the simulation.

3.2 Results and Discussion

3.2.1 Hydrogen Evolution Reaction on n-GaAs Electrodes

Figure 17 shows cyclic voltammograms (CV) of the HER at magnetically modified
(nGaAsMag) and Nafion modified (nGaAsNaf) electrodes. When hydrogen evolution
current reaches 1 mA, the potential of the magnetically modified electrodes is 233
mV positive of the potential for Nafion modified electrodes. Concentrations are
the same for both electrodes. The more facile HER on the magnetically modified
electrodes arise from magnetically improved heterogenous electron transfer kinetics.
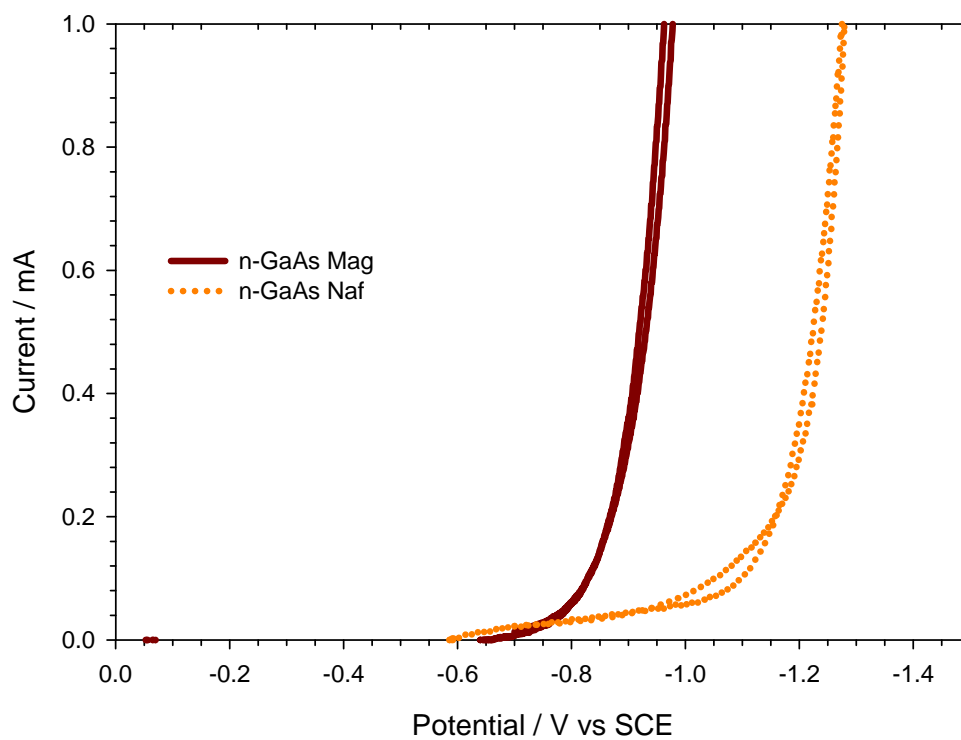
Figure 17. Cyclic voltammograms for hydrogen evolution on n-GaAs electrodes with magnetic modification (solid) and Nafion modification (dotted). The potential of the magnetically modified electrodes is 233 mV positive of the potential for Nafion modified electrodes

Hydrogen evolution is an adsorbate reaction. Adsorbate reactions can be modeled as diffusion-free thin layer cells [37, 46].

Analysis for a totally irreversible electron transfer process in a thin layer cell is

$$E_{pc} = E^{0\prime} + \frac{RT}{\alpha F} \ln \left(\frac{ARTk^0}{\alpha FVv} \right) \tag{14}$$

where E_{pc}, $E^{0\prime}$, R, T, α, F, k^0, F, A and v are peak potential (V), formal potential (V), ideal gas constant (8.314 J mol^{-1} K^{-1}), temperature (K), transfer coefficient, standard heterogeneous rate constant (cm/s), Faraday constant (9.64853×10^4 C), electrode surface area (cm^2) and scan rate (V/s), respectively.

Because the hydrogen evolution current-voltage profile does not depict a peak current, E_{pc} analysis can not be directly applied to the measured data. However, relative k^0 values for the two systems can be estimated by comparing potentials at the same current on each system. Therefore, if E_1 and E_2 are potentials when each magnetic and non-magnetic electrode reaches the same current, the ratio of heterogeneous rate constant for magnetic (k_1^0) and non-magnetic (k_2^0) electrode can be calculated from Equation 15.

$$
\begin{aligned}
E_1 - E_2 &= \frac{RT}{\alpha F} \ln \left(\frac{ARTk_1^0}{\alpha FVv} \right) - \frac{RT}{\alpha F} \ln \left(\frac{ARTk_2^0}{\alpha FVv} \right) \\
&= \frac{RT}{\alpha F} \ln \left(\frac{k_1^0}{k_2^0} \right)
\end{aligned}
$$

$$\frac{k_1^0}{k_2^0} = \exp \left[\frac{\alpha F}{RT} (E_{pc1} - E_{pc2}) \right] \tag{15}$$

This analysis is a good approximation if the wave shapes for the thin layer response are the same. The potential difference between the magnetically modified

electrode and Nafion modified electrode for current of at 1.0 mA is 233 mV. Assuming $\alpha = 0.5$, The calculated ratio of rate constants (k_1^0/k_2^0) for n-GaAsMag to n-GaAsNaf is 93. The heterogenous electron transfer kinetics of the HER on an n-GaAs electrode is estimated to be 93 times faster or about two orders of magnitude faster under magnetic modification than with only Nafion modification.

Figures 18 and 19 show potential sweep voltammograms of the hydrogen evolution reaction on a magnetically modified n-GaAs electrode (nGaAsMag, dotted red) and Nafion modified n-GaAs electrode (nGaAsNaf, dashed green). Reaction kinetics of these two potential sweep voltammograms are obtained by fitting the data to the computer simulation for cyclic voltammetry. Simulated data (solid black) for the n-GaAsNaf and n-GaAsMag are plotted in Figures 18 and 19, respectively. Butler-Volmer kinetic and explicit finite difference method for semi-infinite linear diffusion are used for the simulation. In Tables 10 and 11, parameters for the simulated data fitting are tabulated. All parameters are the same for the two simulations except for the dimensionless rate constant X_0, which is set by k^0. As shown in the Tables 10 and 11, the k^0 for magnetically modified n-GaAs is 1.6×10^{-13} where as k^0 for the Nafion modification is 1.6×10^{-15}. The transfer coefficients (α) are the same for the two electrodes, $\alpha = 0.2$. From the result of the simulations, the fact that magnetic field modification improves the HER rate constant on n-GaAs electrodes 100 times is also confirmed by computer simulation.
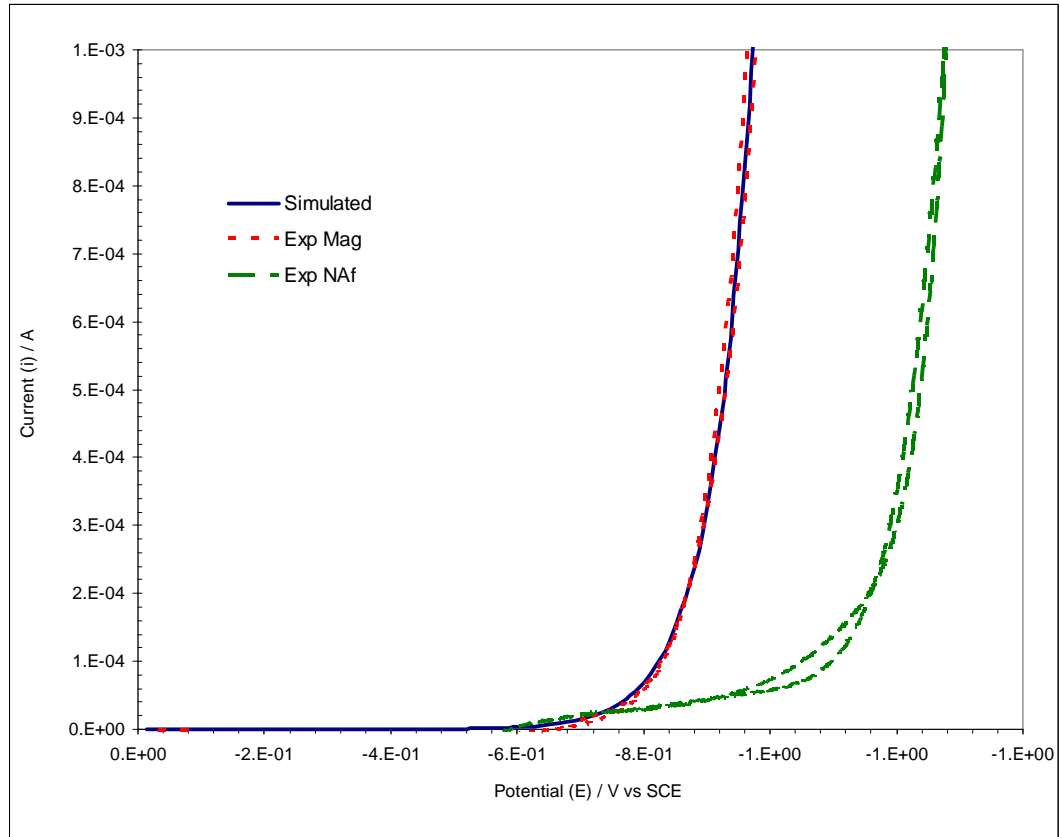
Figure 18. Potential sweep voltammogram of hydrogen evolution on n-GaAs electrodes with magnetic modification (dotted red) and Nafion modification (dashed green). Blue solid line is computer simulated current voltage profile for magnetically modified n-GaAs electrode where k^0 is 1.6×10^{-13}. Refer to Table 10 for more details about the simulation parameters.

Table 10. Simulation parameters for magnetically modified n-GaAs electrode.

E_{init}	0	V	E^0	-2.42	V
E_f	-2	V	α	1.2	
A	0.25	cm^2	D$_i$	0.49	
Frx Conc	1		X_0	3.20×10^{-10}	
υ	0.1	V/s	n	2	
T	298	K	k^0	1.6×10^{-13}	
t_k	40		D	1.0×10^{-5}	cm^2/s
C	1.5	mole/cm^3	$j_{\max}$	73.7	
			$k_{\max}$	0.003	
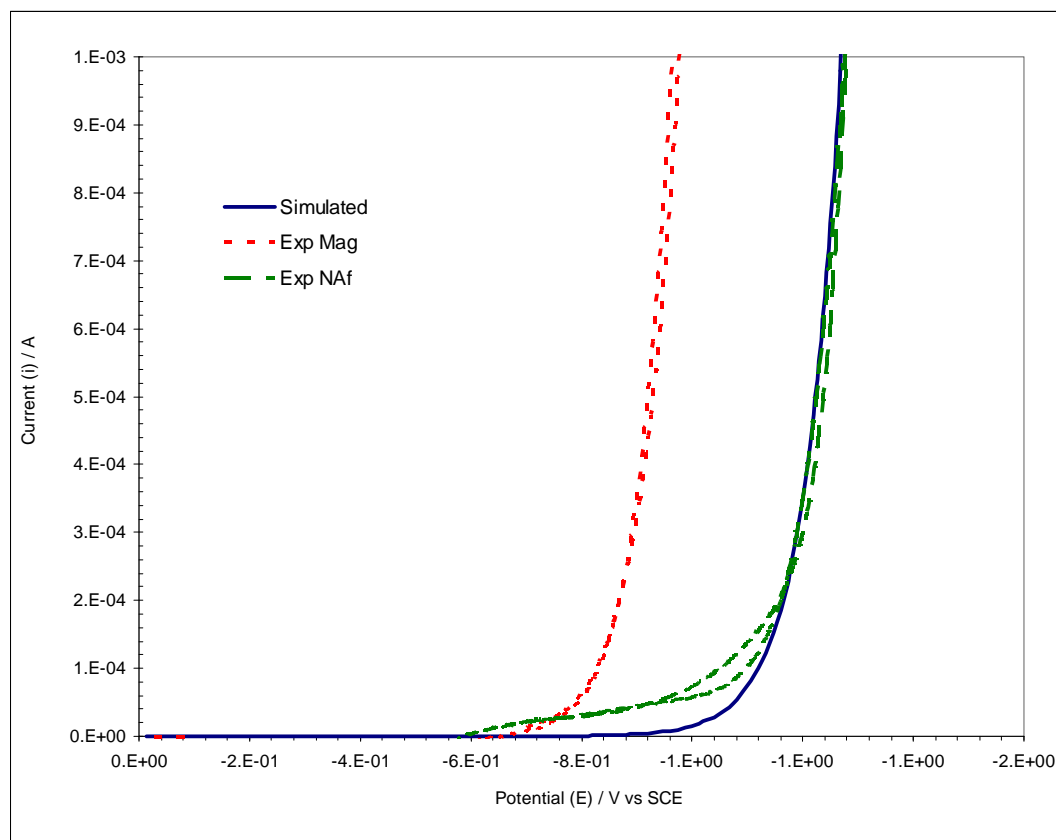
Figure 19. Potential sweep voltammogram of hydrogen evolution on n-GaAs electrodes with magnetic modification (dotted red) and Nafion modification (dashed green). Blue solid line is computer simulated current voltage profile for Nafion modified n-GaAs electrode where k^0 is 1.6×10^{-15}. Refer to Table 11 for more details about the simulation parameters.

Table 11. Simulation parameters for Nafion modified n-GaAs electrode.

E_{init}	0	V	E^0	-2.42	V
E_f	-2	V	α	0.2	
A	0.25	cm^2	D$_i$	0.49	
Frx Conc	1		X_0	3.20×10^{-12}	
υ	0.1	V/s	n	2	
T	298	K	k^0	1.6×10^{-15}	
t_k	40		D	1.0×10^{-5}	cm^2/s
C	1.5	mole/cm^3	$j_{\max}$	73.7	
			$k_{\max}$	0.003	

3.2.2 Hydrogen Evolution Reaction on Glassy Carbon Electrodes

Figures 20 and 21 show potential sweep voltammograms for the hydrogen evolution reaction on magnetically modified glassy carbon electrode (MMGCE, dotted red) and Nafion modified glassy carbon electrode (NMGCE, dashed green).

The potential differences between MMGCE and NMGCE at 1.0×10^{-4} A and 1.0×10^{-3} A are 0.314 V and 0.111 V, respectively. Since the potential differences vary with the current, the thin layer analysis used for n-GaAs electrodes is not appropriate here.

Reaction kinetics of these two potential sweep voltammograms are obtained by fitting the data to a computer simulation for the cyclic voltammogram. Simulated data (solid black) for the NMGCE and MMGCE are plotted in Figure 20 and 21, respectively. Butler-Volmer kinetic and explicit finite difference method for semi-infinite linear diffusion are used for the simulation. In Tables 12 and 13, parameters for simulation fitting are tabulated. k^0 for MMGCE is 8×10^{-11} where as k^0 for NMGCE, it is 1×10^{-15}. From the result of the simulations, magnetic modification improves the rate constant of HER on GCEs by 8×10^4 fold. The transfer coefficient (α) of MMGCE, 0.1, is much smaller than that for NMGCE, 0.3. Because the transfer coefficient characterizes the symmetry of the energy barrier for electron transfer, different α values mean the symmetry of the energy barrier of the reaction under the magnetic field differs from the barrier without the magnetic filed.
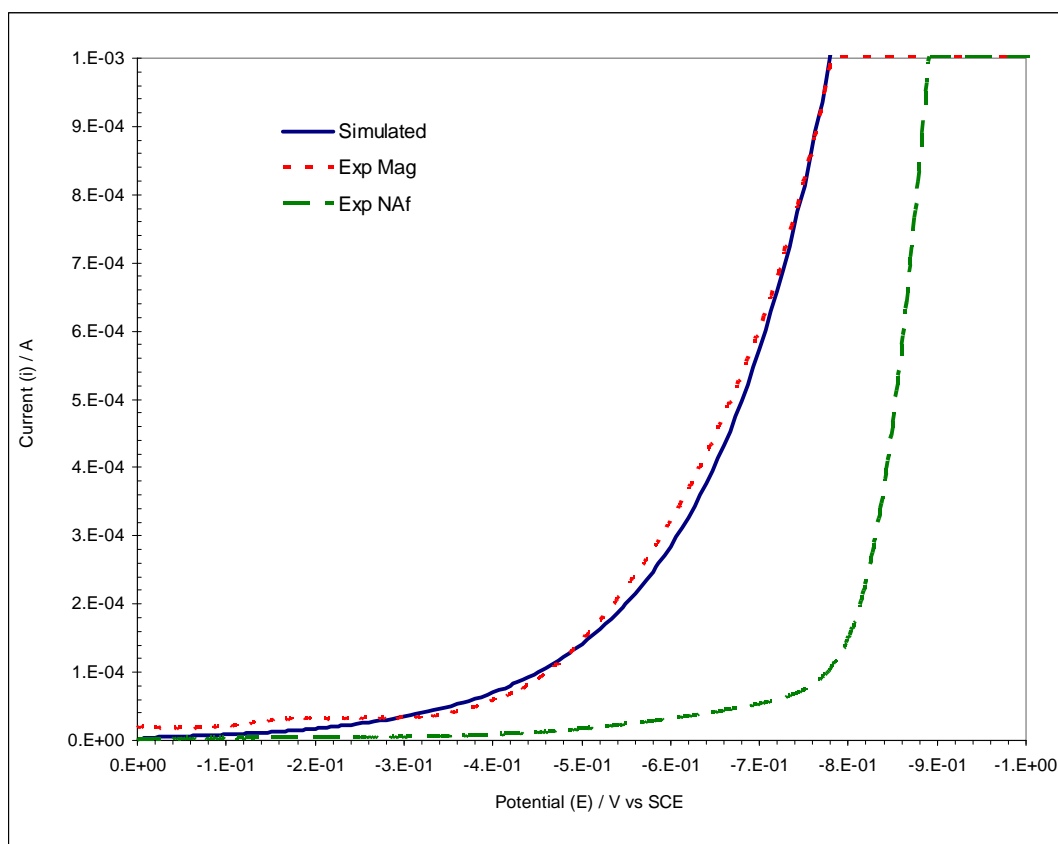
Figure 20. Potential sweep voltammogram of hydrogen evolution on glassy carbon electrodes with magnetic modification (dotted red) and Nafion modification (dashed green). Blue solid line is computer simulated current voltage profile for magneticaly modified GC electrode where k^0 is 1.4×10^{-10}. Refer to Table 12 for more details about the simulation parameters.

Table 12. Simulation parameters for magnetically modified glassy carbon electrode.

E_{init}	0	V	E^0	-2.42	V
E_f	-1	V	α	0.09	
A	0.785	cm^2	D_i	0.49	
Frx Conc	1		X_0	1.41×10^{-7}	
υ	0.1	V/s	n	2	
T	298	K	k^0	1×10^{-10}	
t_k	20		D	1.0×10^{-5}	cm^2/s
C	1.5	mole/cm^3	j_{max}	73.7	
			k_{max}	0.003	
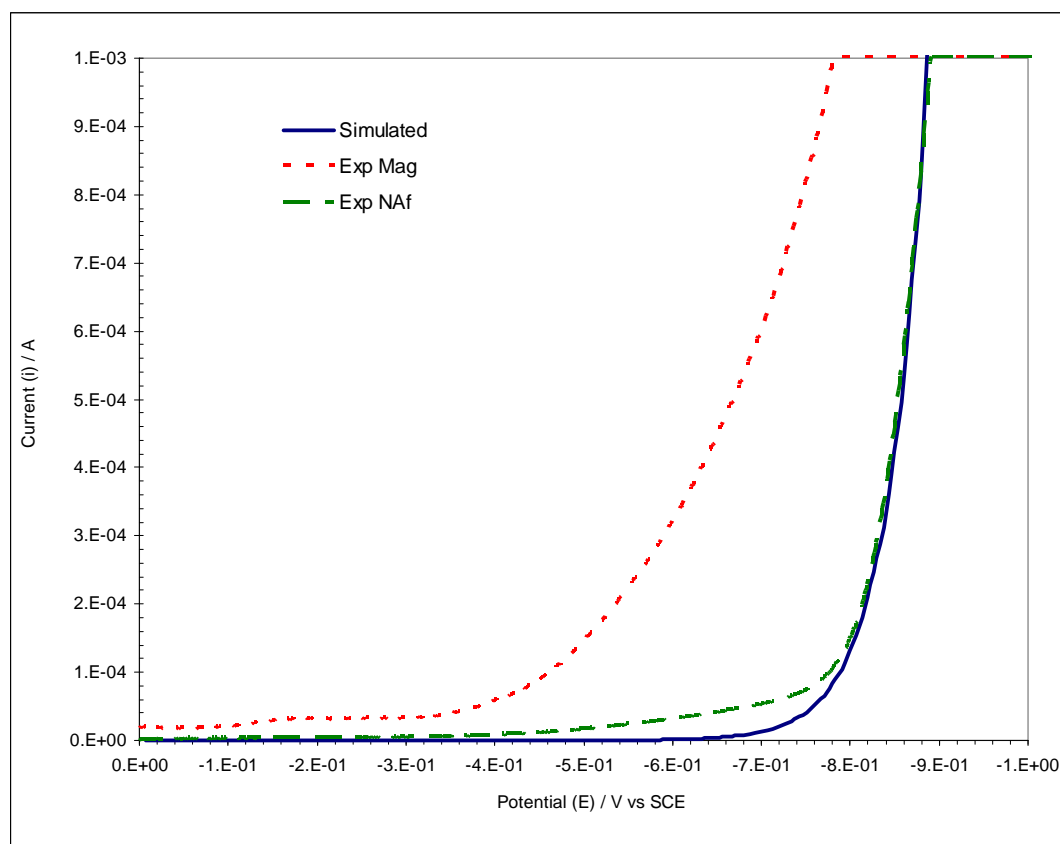
Figure 21. Potential sweep voltammogram of hydrogen evolution on glassy carbon electrodes with magnetic modification (dotted red) and Nafion modification (dashed green). Blue solid line is computer simulated current voltage profile for Nafion modified GC electrode where k^0 is 1.4×10^{-15}. Refer to Table 13 for more details about the simulation parameters.

Table 13. Simulation parameters for Nafion modified glassy carbon electrode.

E_{init}	0	V	E^0	-2.42	V
E_{fin}	-1	V	α	0.3	
A	0.785	cm^2	D_i	0.49	
Frx Conc	1		X_0	1.98×10^{-12}	
υ	0.1	V/s	n	2	
T	298	K	k^0	1.4×10^{-15}	
t_k	20		D	1.0×10^{-5}	cm^2/s
C	1.5	$mole/cm^3$	j_{max}	73.7	
			k_{max}	0.003	

3.2.3 Hydrogen Evolution Reaction on p-Type Silicon Electrodes

Figures 22 and 23 show potential sweep voltammograms for the hydrogen evolution reaction on a magnetically modified p-type silicon electrode (100a/M20/1, dotted red) and Nafion modified p-type silicon electrode (100a/M0/1, dashed green). Electrodes are illuminated as in Chapter 2. The potential differences between 100a/M20/1 and 100a/M0/1 at 5×10^{-4} A and 2.5×10^{-3} A are 0.383 V and 0.244 V, respectively. Because the potentials differences vary with the current, the thin layer analysis is not appropriate here, again.

Reaction kinetics of these two potential sweep voltammograms are obtained by fitting the data to a computer simulation for a cyclic voltammetry. Simulated data (solid black) for the 100a/M20/1 and 100a/M0/1 are plotted in Figures 22 and 23, respectively. In Tables 14 and 15, parameters for the simulation fitting are tabulated. k^0 for 100a/M20/1 is 1.3×10^{-9} whereas k^0 for 100a/M0/1 is 2.0×10^{-11}. From the simulations, the magnetic modification increases the rate constant for the HER on p-type silicon by 65 fold. The transfer coefficient (α) of 100a/M20/1, 0.08, is much smaller than that for100a/M0/1, 0.135. Because the transfer coefficient characterizes the symmetry of the energy barrier for electron transfer, different α values mean the symmetry of the energy barrier of the reaction under magnetic field differs from the barrier without the magnetic field.

If a totally irreversible thin layer cell analysis is used at the potentials when current is 1 mA, the ratio of k^0 of 100a/M20/1 and k^0 of 100a/M0/1 is 266. The results of the totally irreversible thin-layer analysis and of Butler-Volmer kinetic
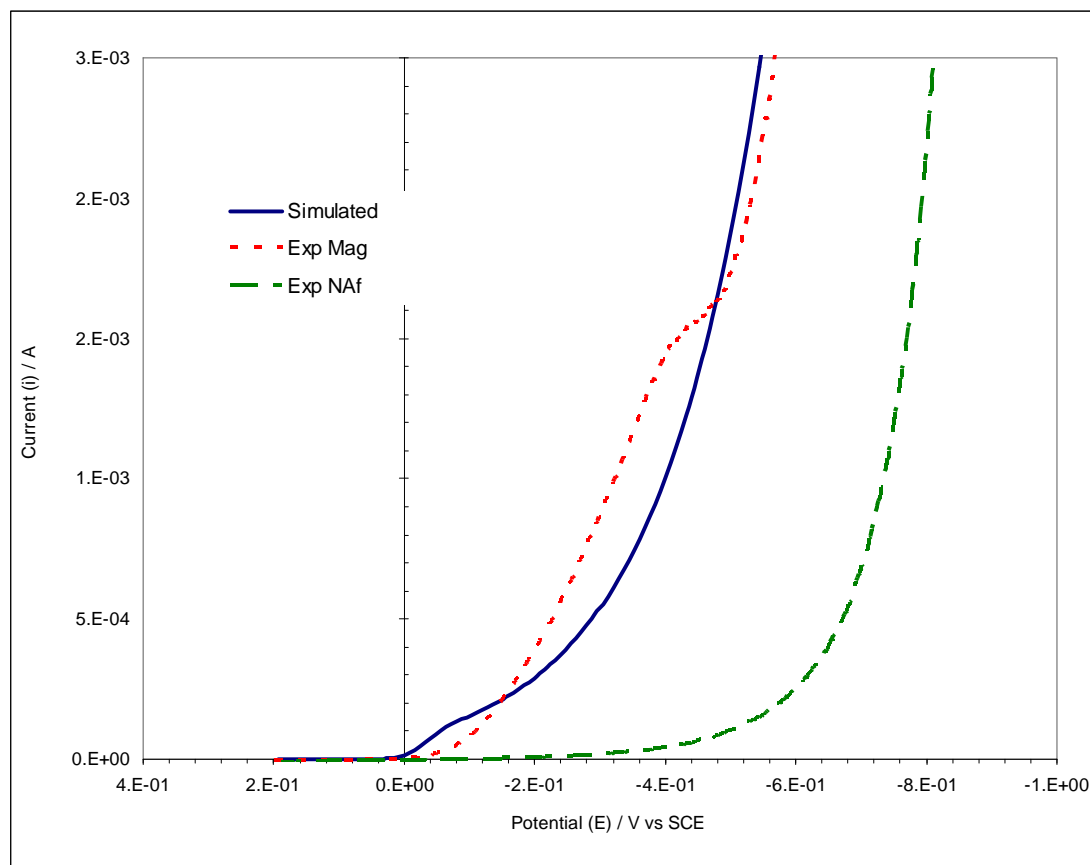
Figure 22. Potential sweep voltammogram of hydrogen evolution on p-Si electrodes with magnetic modification (dotted red) and Nafion modification (dashed green). Blue solid line is computer simulated current voltage profile for magneticaly modified p-Si electrode where k^0 is 2.01×10^{-6}. Refer to Table 14 for more details about the simulation parameters.

simulation has differ by about 4 fold, but this is not surprising as the α value assumed in the thin layer analysis is 0.5. Both analyses are consistent with a substantial increase in rate under magnetic modification.

3.2.4 Summary of Data

The data for the magnetic and Nafion modified electrodes are summarized in Table 16.

Table 14. Simulation parameters for magnetically modified p-Si electrode.

E_{init}	0.2	V	E^0	-2.42	V
E_f	-1	V	α	0.08	
A	1	cm^2	D_i	0.49	
Frx Conc	1		X_0	2.01×10^{-6}	
υ	0.1	V/s	n	2	
T	298	K	k^0	1.3×10^{-9}	
t_k	24		D	1.0×10^{-5}	cm^2/s
C	1.5	$mole/cm^3$	j_{max}	73.7	
			k_{max}	0.003	
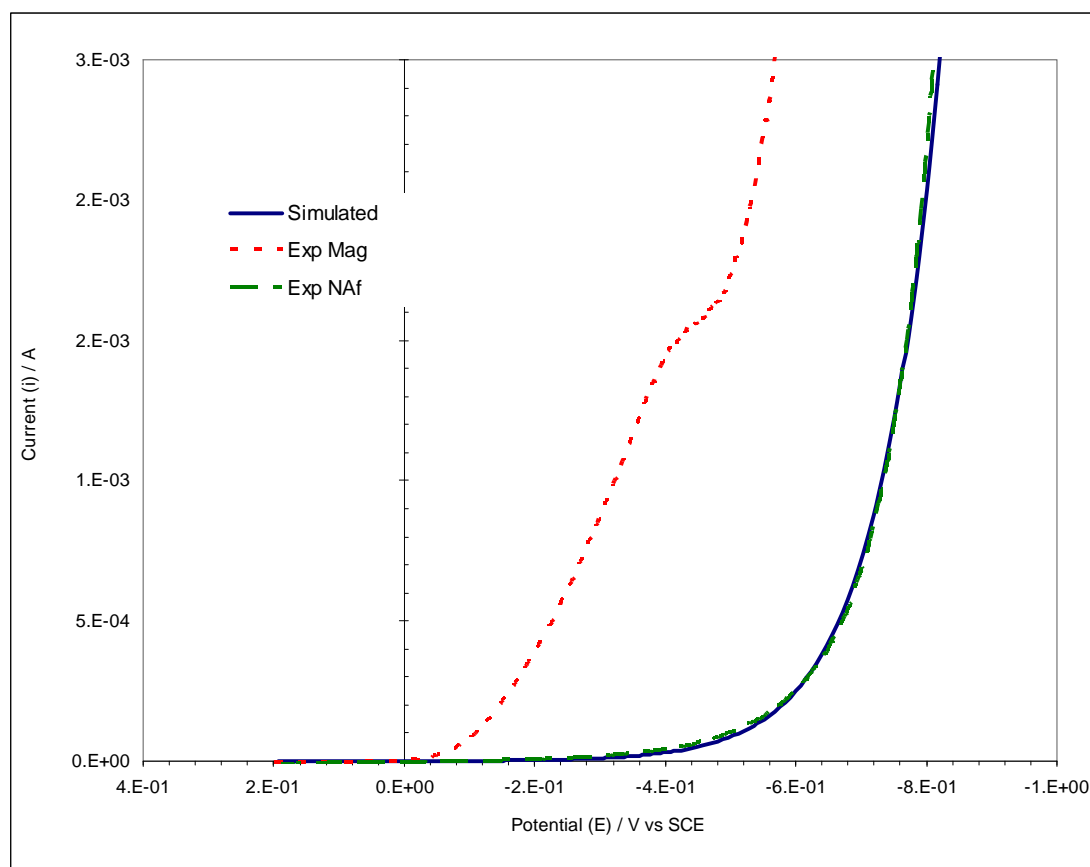
Figure 23. Potential sweep voltammogram of hydrogen evolution on p-Si electrodes with magnetic modification (dotted red) and Nafion modification (dashed green). Blue solid line is computer simulated current voltage profile for magneticaly modified p-Si electrode where k^0 is 2.01×10^{-6}. Refer to Table 14 for more details about the simulation parameters.

Table 15. Simulation parameters for Nafion modified p-Si electrode.

E_{init}	0.2	V	E^0	-2.42	V
E_f	-1	V	α	0.135	
A	1	cm^2	D_i	0.49	
Frx Conc	1		X_0	3.10×10^{-8}	
υ	0.1	V/s	n	2	
T	298	K	k^0	2.00×10^{-11}	
t_k	24		D	1.0×10^{-5}	cm^2/s
C	1.5	$mole/cm^3$	j_{max}	73.7	
			k_{max}	0.003	

Table 16. Summary of k^0 and α data for noncatalytic electrodes and Pt.

	Surface	Loading	$k^0(Mag)/k^0(Naf)$	$\alpha(Mag)$	$\alpha(Naf)$
n-GaAs	(100)	15	100	0.2	0.2
Glassy Carbon	-	15	80,000	0.09	0.3
p-Si	(100)	20	65	0.08	0.135
Pt	-	-	1	0.5	0.5

From the data, magnetic modification consistently increases the standard heterogeneous rate constant, k^0. The largest effect is for GC, where the increase is 80,000 fold and the current voltage profile shifts about 111 - 314 mV to lowered potential. For n-GaAs, k^0 is 100 fold faster and overpotential is reduced by 233 mV. For p-Si, k^0 is 65 fold faster aand the current voltage profile shifts about 383 - 244 mV to lowered potential. The transfer coefficients are low for all these adsorbate reactions, and in the case of glassy carbon and p-Si, the α values are smaller under magnetic modification.

3.3 Discussion and Conclusion

To investigate magnetic field effects on the HER on noncatalytic electrodes,

n-GaAs , glassy carbon , p-Si electrodes are prepared and modified with a mixture of magnetic particles and Nafion or only Nafion. By comparing current voltage profiles of HER on these electrodes, it has been shown that heterogenous electron transfer kinetics for hydrogen evolution on magnetically modified electrodes is 10^2 to 10^4 times faster than only Nafion modified electrodes. Results are summarized in Table 16.

For n-GaAs electrode experiments, peak current analysis for a totally irreversible thin layer cell is used and the ratio of the electron transfer rate constant of a magnetic modified electrode and a Nafion modified electrode is calculated and k_{mag}/k_{naf} is 93. For the glassy carbon experiments, experimental results of potential sweep voltammogram are fitted by computer simulation which is based on the models of Butler-Volmer kinetic and explicit finite difference method for mass transport. The result of the simulation is a k_{mag}/k_{naf} ratio of 10^4. Although calculated and simulated values are different by two orders of magnitude, the discrepancy can be attributed to the differences between assumptions of these two methods and possible material properties differences. The fact that the magnetic field enhances the heterogeneous electron trasfer kinetic of hydrogen evolution reaction is confirmed.

Magnetic fields have been shown to increase the rate of electron transfer at semiconductor surfaces (Chapter 2) and between outer sphere transition metal complexes (Chapter 4). Here, the rate of heterogeneous electron transfer are substantially improved at noncatalytic electrodes. Further increases in the efficiency of these electrodes are possible with application of magnetic microparticles with higher magnetization, such as samarium cobalt and neodymium iron boron magnets.

With sufficiently high magnetic fields, noncatalytic electrodes may be rendered effective catalysts. Conversely, the efficiency of catalytic electrode may arise from their magnetic properties and ability to interact with the spin characteristics of redox probe and adsorbates.

CHAPTER 4

MAGNETIC FIELD EFFECT ON SELF EXCHANGE REACTION

4.1   Theoretical Background

Magnetic field effects on self exchange reactions were first reported by Shelley Minteer [1]. It was found the rates increased in the field and in proportion to the magnetic properties of the redox probe. For reactions where the halves of the redox couple include one diamagnetic and one paramagnetic species, the rates were proportional to gS, where g is the Lande g-value and S is the spin for the paramagnetic half of the couple. However, full physical interpretation of these results for outer sphere transition metal redox couples has not been completed. Models are needed that account for different spin states, gS, and the impact of the field strength, H.

To develop a more complete physicochemical model for magnetic effects, the temperature dependence of magnetic field effects on self exchange reactions for $Co(bpy)_3^{2+/3+}$, $Co(bpy)_3^{2+/1+}$, $Ru(bpy)_3^{3+/2+}$ and $Os(bpy)_3^{3+/2+}$ redox couples are studied at electrodes modified with Nafion, with and without magnetic microparticles. Magnetic microparticles with different magnetic field strengths were used to vary the field. The couples have different self exchange rates, standard potentials, and magnetic properties, but are otherwise similar in charge, size, and electrostatic interaction with the Nafion matrix. Cyclic voltammetric peak currents were determined for each redox probe at various temperatures from 5 to 70 ^{o}C. The

square of the peak current is proportional to the apparent diffusion coefficient that is, in turn, proportional to the self exchange rate.

The data are analyzed according to the Arrhenius equation to find the pre-exponential factor and the activation energies of the self exchange reaction for each redox couple. The data derived from the Arrhenius analysis are the basis of a model for magnetic effects that is developed within classical transition state theory (TST). The relatively simple model includes impacts of prepolarization in an applied field and spin polarization effects on the cage complex. When one half of the redox couple is a singlet (diamagnetic), electron nuclear spin polarization occurs. In this model, magnetic impacts on enthalpy and entropy are identified. The model provides a simple interpretation of outer sphere self exchange reactions of tris-bipyridal complexes. It is found that gHS is a component in the enthalpy of activation but that enthalpy is largely set by electrostatics. The entropy includes terms associated with the spin states of the halves of the couple.

4.1.1 Physical Diffusion and Hopping Diffusion in Electrochemical Systems

Figure 24 shows an electrochemical system of an electrode in low viscosity electrolyte such as an aqueous solution. Three basic electrochemical events are presented: change of potential on the electrode, heterogeneous electron transfer to a redox probe (e.g., Ru^{3+}), and diffusion of the product (e.g., Ru^{2+}) away from the electrode and fresh reactant (e.g., Ru^{3+}) toward the electrode. In typical electrochemical systems, the concentration of the redox probe is low and the viscosity

is low such that transport occurs by physical diffusion. In the Dahms [47] and Ruff [48–50] models, diffusion of redox couples in an electrolyte occurs by two processes [51]. One process is physical diffusion and the other is electron hopping. When the electrolyte has low viscosity, the motion of the redox couple is parameterized by D_p (cm^2/s), physical diffusion. When electrolyte viscosity is extremely high, physical diffusion is limited. If the concentration of the redox probes is also high, electron hopping between adjacent redox moieties becomes possible and the diffusion is enhanced by electron self exchange between the redox moieties. This is illustrated in Figure 25 when electrodes are modified with Nafion that restricts physical motion and extracts cations to high concentrations. Under these conditions, the measured apparent diffusion coefficient (D_0) is dominated by self exchange or hopping diffusion. Dahms and Ruff modeled the apparent diffusion coefficient in terms of D_p and the self exchange diffusion coefficient D_{et}.

$$D_0 \quad = \quad D_p + D_{et} \tag{16}$$

$$= \quad D_p + \frac{k_{ex}\delta^2 C_0^*}{6} \tag{17}$$

where k_{ex} is the self exchange reaction rate constant (M^{-1}s^{-1}), δ is the center to center distance between the two adjacent redox moieties that undergo self exchange (cm), and C_0^* is bulk concentration of the redox couple (M). The value of 6 is a geometric factor for three dimensions. Based on data from Gellett's dissertation [2] for transition metal complexes in Nafion, D_p is of the order of 10^{-12} cm^2/s, which is negligible compared to D_{et}. Thus,

$$D_0 \rightarrow \frac{k_{ex}\delta^2 C_0^*}{6} \tag{18}$$
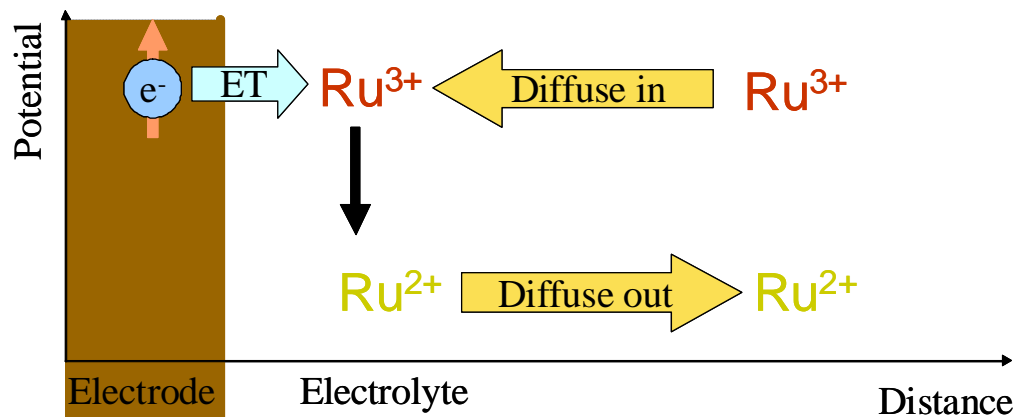
Figure 24. Schematic diagram of an electrochemical cell in a low viscosity electrolyte. The three events central to the current response are: potential at the electrode surface is applied, heterogeneous electron transfer event occurs between the electrode and redox probe in solution, and the redox reactant and product diffusion toward and away from the electrode, respectively.

4.1.2 Determination of Apparent Diffusion Coefficients

In cyclic voltammetry, the peak current on the forward sweep yields the apparent diffusion coefficient, D_0. The transition metal complexes considered here are fully exchanged into Nafion and displace all other cations. The complexes neutralize the available sulfonic acid sites $(-SO_3^-)$ of the Nafion. The sulfonate concentration is determined from in the Nafion density, 1.95 g cm^{-3} [52], and the nominal equivalent weight of 1100 g/mole of SO_3^-. (Titration has shown the equivalent weight is closer to 1000 g/mol of SO_3^- [45].) This yields $C_{SO_3}^* = (1.95\ gc\ m^{-3})/(1100\ g/mol) = 1.77 \times 10^{-3}$ mol/cm^3. The concentration of the redox probe is determined from the charge of the redox species present at the electrode surface at the start of the cyclic voltammetric perturbation of the redox couple. For a species with $z_{initial}$ of 3, the redox probe
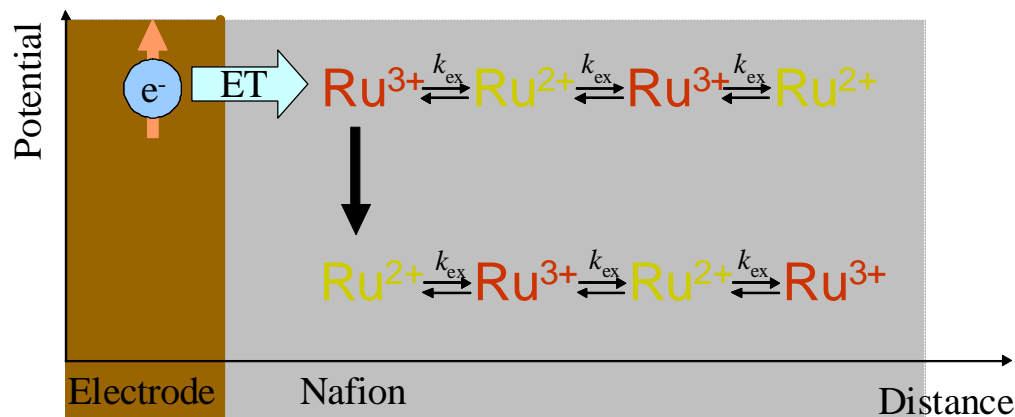
Figure 25. Schematic diagram of an electrochemical cell with a high viscosity medium at the electrode surface where physical diffusion is slow and the redox probe concentration is high. This reduces physical diffusion and enhances electron hopping or self exchange diffusion, where the self exchange rate is k_{ex}. The events central to the current response are: potential at the electrode surface is applied, heterogeneous electron transfer event occurs between the electrode and redox probe in solution, and the redox reactant and product diffusion toward and away from the electrode by physical and hopping diffusion, respectively. In the extreme case, such as in Nafion, physical diffusion is negligible as compared to hopping diffusion.

concentration is $C_0^* = C_{SO_3}^*/z_{initial} = 0.591 \times 10^{-3}$ mol/cm^3; for $z_{initial}$ of 3,

$C_0^* = 0.886 \times 10^{-3}$ mol/cm^3.

For species with fast heterogeneous electron transfer rates, Equation 19 known as Randles-Sevcik equation is appropriate where the peak current on the forward potential sweep is i_p (A) [53].

$$i_p = 2.69 \times 10^5 n^{\frac{3}{2}} A D_0^{\frac{1}{2}} C_0^* v^{\frac{1}{2}} \tag{19}$$

where n is the number of electrons transferred in the heterogeneous electron process (here, $n = 1$ throughout); A is area in cm^2; and v is the cyclic voltammetric scan rate in V/s (here, $v = 0.100$ V/s throughout). D_0 has units of cm^2/s and C_0^* has units of mole/cm^3.

4.1.3 Determination of k_{ex} and the Arrhenius Plots

The apparent diffusion coefficient for these complexes is well represented as in Equation 18. Substitution into Equation 19 yields

$$
\begin{aligned}
i_p &= 0.4463 \left(\frac{F^3}{RT}\right)^{1/2} n^{\frac{3}{2}} A \left(\frac{k_{ex}\delta^2 C_0^*}{6}\right)^{\frac{1}{2}} C_0^* v^{\frac{1}{2}} \\
&= \left(\frac{0.4463}{6^{\frac{1}{2}}}\right) \left(\frac{F^3}{R}\right)^{1/2} \left(\frac{1}{T}\right)^{1/2} n^{\frac{3}{2}} A\delta C_0^{*\frac{3}{2}} v^{\frac{1}{2}} k_{ex}^{\frac{1}{2}} \\
&= 1.893 \times 10^6 n^{\frac{3}{2}} A\delta C_0^{*\frac{3}{2}} v^{\frac{1}{2}} k_{ex}^{\frac{1}{2}} \tag{20} \\
&= L k_{ex}^{\frac{1}{2}} \left(\frac{1}{T}\right)^{1/2} \tag{21}
\end{aligned}
$$

Peak current and self exchange reaction rate constant are related as in Equation 22.

$$
i_p^2 T = L^2 k_{ex} \tag{22}
$$

$$
\frac{i_p^2 T}{L^2} = k_{ex} \tag{23}
$$

where

$$
L^2 = 3.582 \times 10^{12} n^3 A^2 \delta^2 C_0^{*3} v \tag{24}
$$

For the $M\,(bpy)_3^{2+/3+}$ and $M\,(bpy)_3^{1+/2+}$ complexes, where $\delta = 1.36 \times 10^{-7}$ cm and $n = 1$. Throughout, $v = 0.100$ V/s and $A = 0.196$ cm^2. $L^2 = 3.582 \times 10^{12} \delta^2 A^2 C_0^{*3} = 2.24 \times 10^{-5} A^2 C_0^{*3}$. Allow the initial species to have charge $z_{initial}$ and note $C_{SO_3}^* = 1.77 \times 10^{-3}$ mol/cm^3. Then, $L^2 = 2.24 \times 10^{-5} A^2 \left(C_{S0_3}^*/z_{initial}\right)^3 = 1.24 \times 10^{-13} A^2 z_{initial}^{-3}$.

The self exchange reaction rate constant (k_{ex}) is expressed by the Arrhenius relationship.

$$
\frac{i_p^2 T}{L^2} = k_{ex} = A \exp\left(-\frac{E_a}{RT}\right)
$$

Table 17. Properties in common for the commercial Chemicell magnetite microparticles.

Weight per volume	50 mg/ml
Size	1.0 μm
Number of particles	1.8×10^{12}/g
Surface area	~ 100 m^2/g
Density	2.25 g/cm^3

$$\ln k_{ex} = \ln \left(\frac{i_p^2 T}{L^2} \right) = \ln (A) - \frac{E_a}{R} \left(\frac{1}{T} \right) \tag{25}$$

The self exchange reaction rate constant (k_{ex}) can be determined from peak currents at various temperatures. From Equation 25, activation energy (E_a) and pre-exponential factor (A) can be determined by plotting $\ln \left(i_p^2 \right)$ vs $1/T$. The term $\ln \left(L^2 \right)$ is embedded in the intercept.

4.2   Experimental

4.2.1   Magnetic Particles

Magnetic particles were purchased from Chemicell. Four types of magnetic particles were purchased and the properties are tabulated in the Tables 17 and 18. Although their surface have different functional group coatings, their physical and chemical properties are similar.

The magnetic susceptibilities of lots C1, C3, C8, and C18 are determined below.

Table 18. Properties specific to commercial
Chemicell magnetite microparticles.

	Naming	Functional Group
SiMAG-Octadecyl	C18	$-Si-(CH_2)_{17}CH_3$
SiMAG-Octyl	C8	$-Si-(CH_2)_7CH_3$
SiMAG-Propyl	C3	$-Si-(CH_2)_2CH_3$
SiMAG-Methyl	C1	$-Si-CH_3$
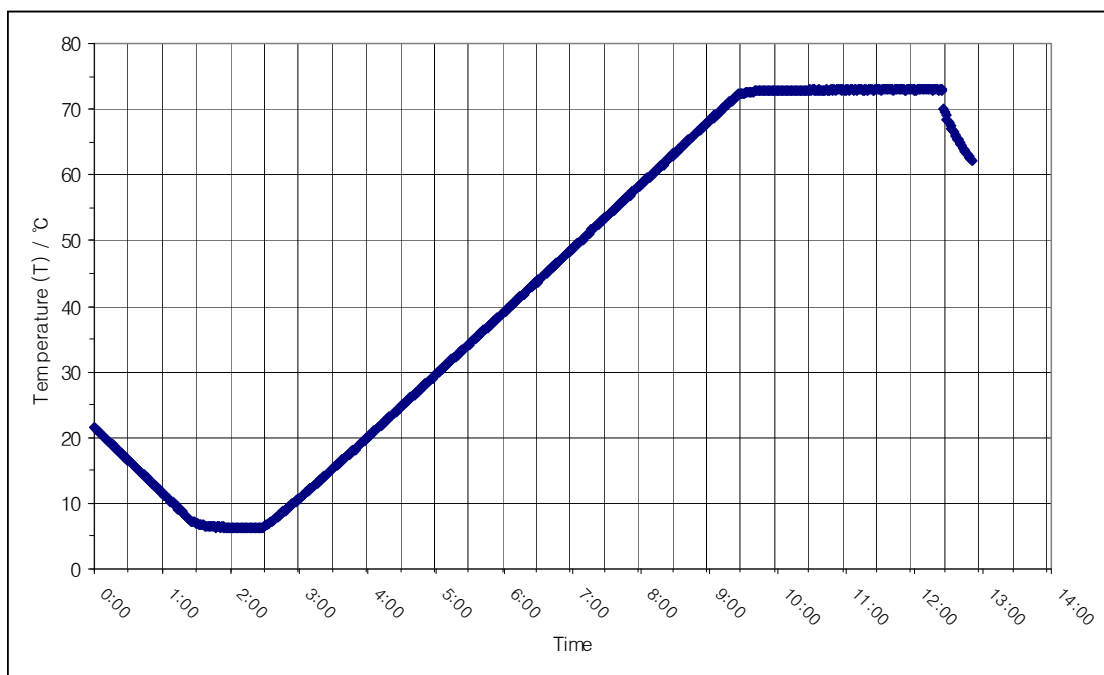
Figure 26. Temperature program for the electrochemical cell. The temperature is first lowered to 5 $^\circ C$ and held for 1 hour. The temperature is then raised to 75 $^\circ C$ at a rate of approximately 10 $^\circ C$/hour. Cyclic voltammograms are recorded at various temperatures along the temperature program.

4.2.2 Temperature Control

Temperature studies were undertaken with a Thermotron Environmental Chamber that was programmed with a 288 Programmer/Controller. The three-electrode cell was placed in the chamber and the temperature was controlled from 5 ^{o}C to 70 ^{o}C. A typical temperature program is shown in Figure 26. The temperature was first lowered to 5 $^{\circ}C$ and held for 1 hour. The temperature was then raised to 75 $^{\circ}C$ at a rate of approximately 10 $^{\circ}$C/hour. Cyclic voltammograms were recorded at various temperatures along the temperature program.

A two probe temperature logger was used to record the temperature (HH506RA Omega). One probe was placed in the air in the chamber and the other was placed in the electrolyte solution attached at the top of a electrode to measure the temperature about the electrode surface.

4.2.3 Magnetic Susceptibility Measurements

Magnetic susceptibilities of the magnetic microparticles were measured with a magnetic susceptibility balance (The Auto MSB, Sherwood scientific). Samples were prepared by dispersing the commercial magnetic particle suspension into deionized water by weight. Before the weighing tube was put in the magnetic susceptibility balance, the suspensionwas thoroughly mix to make the particle dispersed well.

Immediately after the weighing tube was inserted into the balance, the magnetic susceptibility was read as the magnetic susceptibility. The value decreased and stabilized when the magnetic particles agglomerated on the bottom of the test tube.

Table 19. Magnetic Properties of Transition Metal Complexes.

Complex	μ (BM)	m		g	S	gs
$Ru(bpy)_3^{3+}$	1.86	1	D	2.15	1/2	1.07
$Os(bpy)_3^{3+}$	1.49	1	D	1.72	1/2	0.86
$Co(bpy)_3^{2+}$	3.45	3	Q	1.78	3/2	2.67
$Co(bpy)_3^{1+}$	*	2	T		1	2

Note: All values were determined experimentally by Gellett in SQUID except $Co(bpy)_3^{1+}$ (marked by *) , g is taken as 2 and the electron configuration for a T yields $S = 1$.

Because the magnetic susceptibility should have been measured when samples were homogeneously suspended in the test tube, the value measured first was reported as the magnetic susceptibility of the commercial particles.

4.2.4 Experimental Setups

The protocol to evaluate the dependence of the self exchange reaction on temperature was as follows. A glassy carbon electrode (5 mm diameter, $A = 0.196$ cm^2) was modified with either Nafion or Nafion/Simag suspension. A total of six glassy carbon electrodes are prepared. The modified GC electrodes were soaked in an electrolyte solution, containing 1 mM redox couple and 0.1 M electrolyte, to equilibrate the probe into the Nafion matrix for at least 9 hours. A large surface area platinum mesh counter electrode was used and a saturated silver chloride electrode was used as the reference. A Chi1030 8-channel multi-potentiostat was used to measure cyclic voltammograms. Peak currents were measured manually.

The redox species initially extracted into the films are $Co(bpy)_3^{3+}$, $Ru(bpy)_3^{2+}$

and $Os(bpy)_3^{3+}$. The $Co(bpy)_3^{2+/1+}$ was measured on cyclic voltammetric sweep well after the initial present $Co(bpy)_3^{3+}$ had been reduced to $Co(bpy)_3^{2+}$. The initial concentration for the $Co(bpy)_3^{2+/1+}$ was thus taken as $Co(bpy)_3^{2+}$. C_0^* for each species was $C_{SO_3}^*/z_{initial}$. Thus, for $Co(bpy)_3^{3+}$ and $Os(bpy)_3^{3+}$ C_0^* is 0.591×10^{-3} mol/cm^3 and for $Ru(bpy)_3^{2+}$ and $Co(bpy)_3^{2+}$, C_0^* was 0.886×10^{-3} mol/cm^3.

Some data, presented in Table 19 taken from Gellett's dissertation are needed for the current discussion [2]. Several species are singlets: $Ru(bpy)_3^{2+}$, $Os(bpy)_3^{2+}$, and $Co(bpy)_3^{3+}$, so all have $g = 0$, $S = 0$, and $gS = 0$.

4.3 Results

4.3.1 Magnetic Susceptibilities

Magnetic susceptibilities are measured and converted to volume magnetic susceptibilities for the commercial magnetic particles. Figure 27 shows the volume magnetic susceptibilities of the commercial particles. A correlation between volume magnetic susceptibilities and the coatings of the Simag particles was anticipated based on the chain length of the silane coatings, but none was found. The strength of the magnetic field established at each magnetic particle is important to characterizing the response of the magnetically modified electrodes. The susceptibility is taken as a relative measure of the field strength, H. Susceptibilities are presented in Table 20.

4.3.2 $Ru(bpy)_3^{2+/3+}$

The ruthenium complex was used as the probe to assess the impact of different
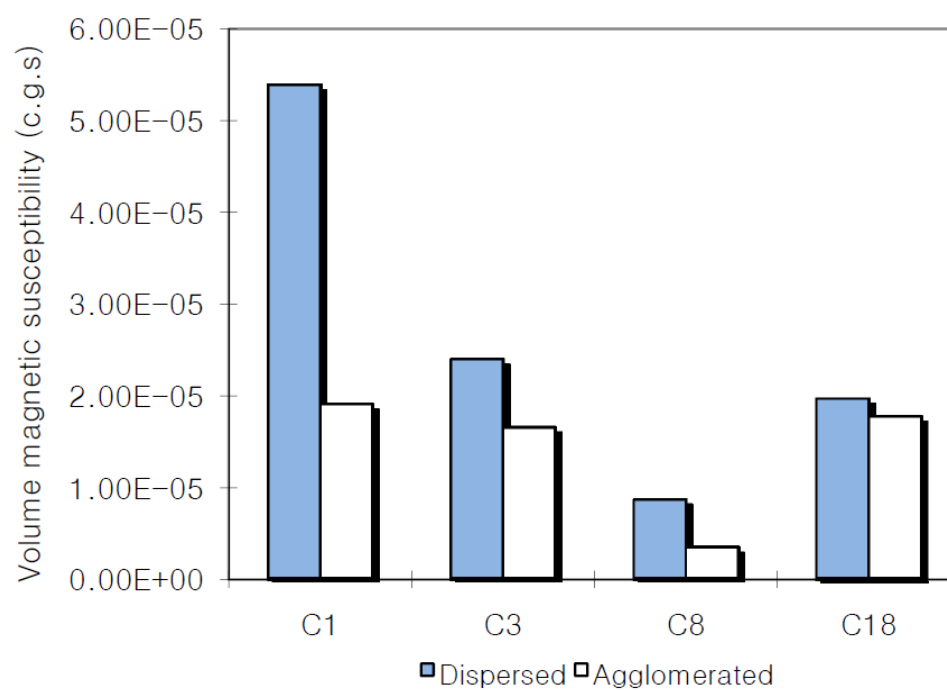
Figure 27. Volume magnetic susceptibilies of purchased SiMAG particles. C1 has highest magnetic susceptibility of 5.39×10^{-05} (c.g.s. scale).

Table 20. Volume magnetic susceptibility in c.g.s. for Simag particles.

	Volume magnetic susceptibility (c.g.s)	
	Dispersed	Agglomerated
C1	5.39×10^{-05}	1.90×10^{-5}
C3	2.39×10^{-05}	1.65×10^{-5}
C8	8.60×10^{-6}	3.40×10^{-6}
C18	1.96×10^{-5}	1.77×10^{-5}
water	-1.06×10^{-06}	
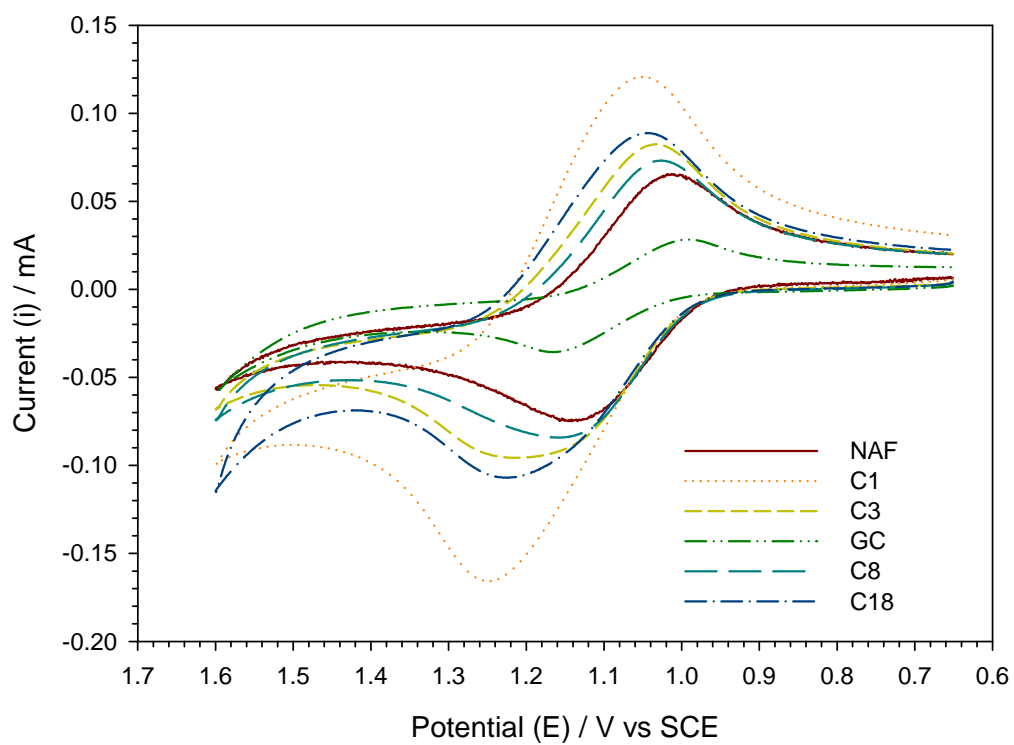
Figure 28. Cyclic voltammogram of $Ru(bpy)_3^{+2/+3}$ on various electrode modifications. Nafion modificaton and C1, C3, C7 and C8 magnetic modifications are applied to each electrode as well as Nafion only modification as a control.

strength magnetic fields established at the electrode surface by using commercial microparticles with different magnetic content. Nafion films and composites of Nafion and C1, C3, C18, and C8 were evaluated.

4.3.2.1 Variation of Response with Magnetic Content

Figure 28 shows cyclic voltammogram for $Ru(bpy)_3^{2+/3+}$ under various electrode modifications. The electrolyte is 1.0 mM $Ru(bpy)_3^{2+/3+}$ in 0.10 M HNO_3. C1, C3, C8 and C18 magnetic microparticles are each applied electrodes in a Nafion suspension. Unmodified and Nafion modified electrode are also shown. Different modifications yield slightly different cyclic voltammetric morphologies and different peak currents. C1 has the highest peak current whereas the unmodified electrode has the lowest peak current. The C1 electrode yields current four times as high as the unmodified electrode.

The peak currents of each voltammogram in Figure 27 increase monotonically with volume magnetic susceptibility. In Figure 29, these data are linearized as peak currents (i_p) versus volume susceptibility. Recall from Equation 22 that $i_p^2 \propto k_{ex}$. When magnetic susceptibility and the magnetic content of the particles increases, the self exchange reaction rate constant increases at room temperature.

4.3.2.2 Variation of Response with Magnetic Content and Temperature

To evaluate the impact of magnetic fields on the self exchange rate, a classical kinetic study to evaluate rate with temperature was undertaken. The different magnetic content commercial particles in Nafion were evaluated as was a Nafion film.
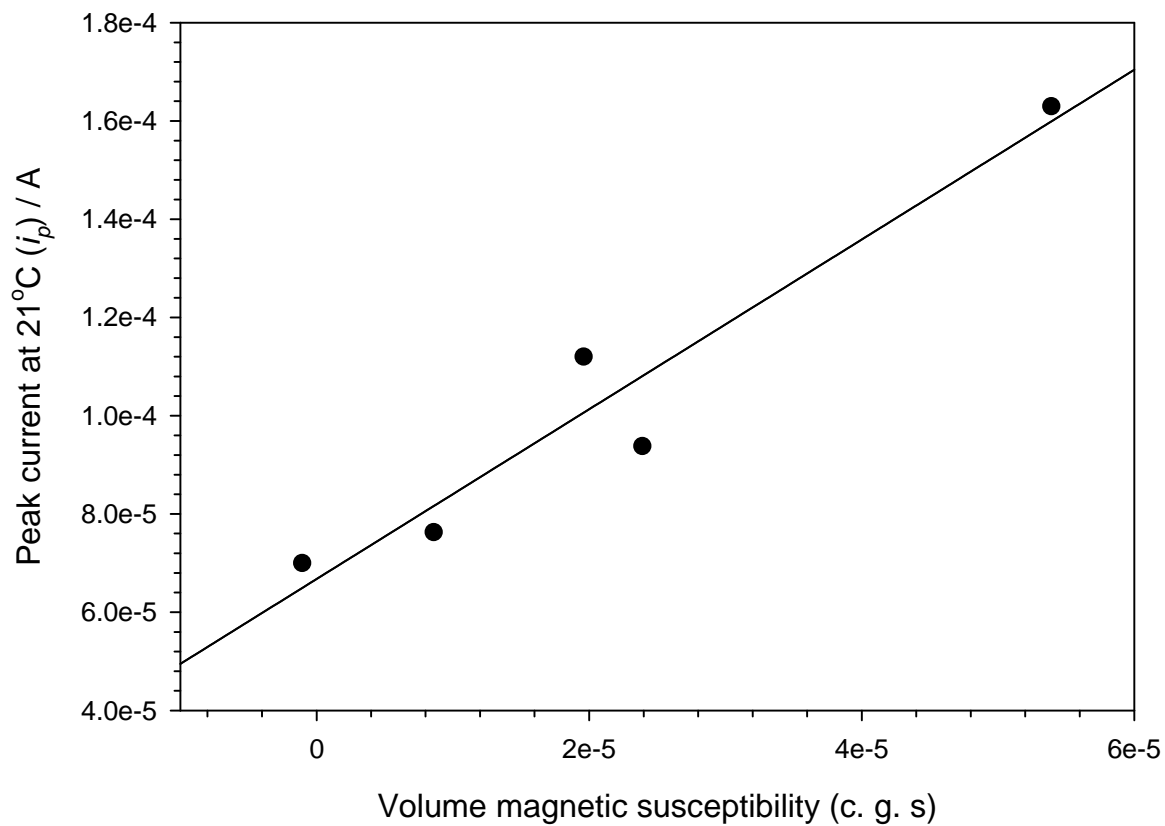
Figure 29. Volume magnetic susceptibility versus i_p at 21 ^{o}C. Peak current is directly related to self exchange reaction rate constat (k_e). When magnetic susceptibility increases self exchange reaction rate becomes faster then showing higher peak current (i_p) for Ru$^{2+/3+}$ at room temperature.
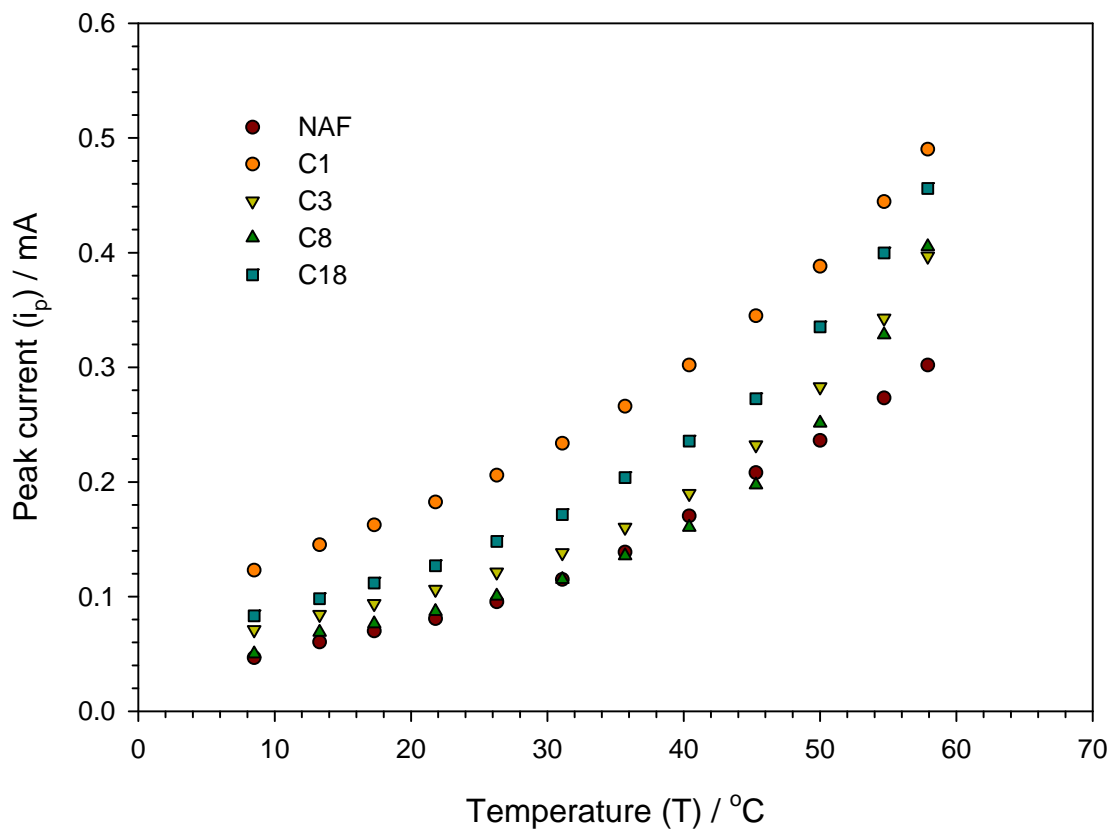
Figure 30. Peak currents (i_p) of CVs at increasing temperature from 5 to 60 °C. Peak currents increase exponentially following Arrhenius behavior.

The results of the temperature studies for 5 to 60 °C are shown in Figure 30. The peak currents increase with temperature. These data are converted to an Arrhenius format, based on Equation 22, by plotting $\ln(i_p^2 T/L^2)$ vs 1/T. The slope of the Arrhenius plot yields the activation energy (E_a) and pre-exponential factor (A). The Arrhenius plots are shown in Figure 31. Note that as the magnetic susceptibility increases, the slopes diminish, with the shallowest slope found for the C1 composites.

From the Arrhenius plot of various electrodes with individual modifications,
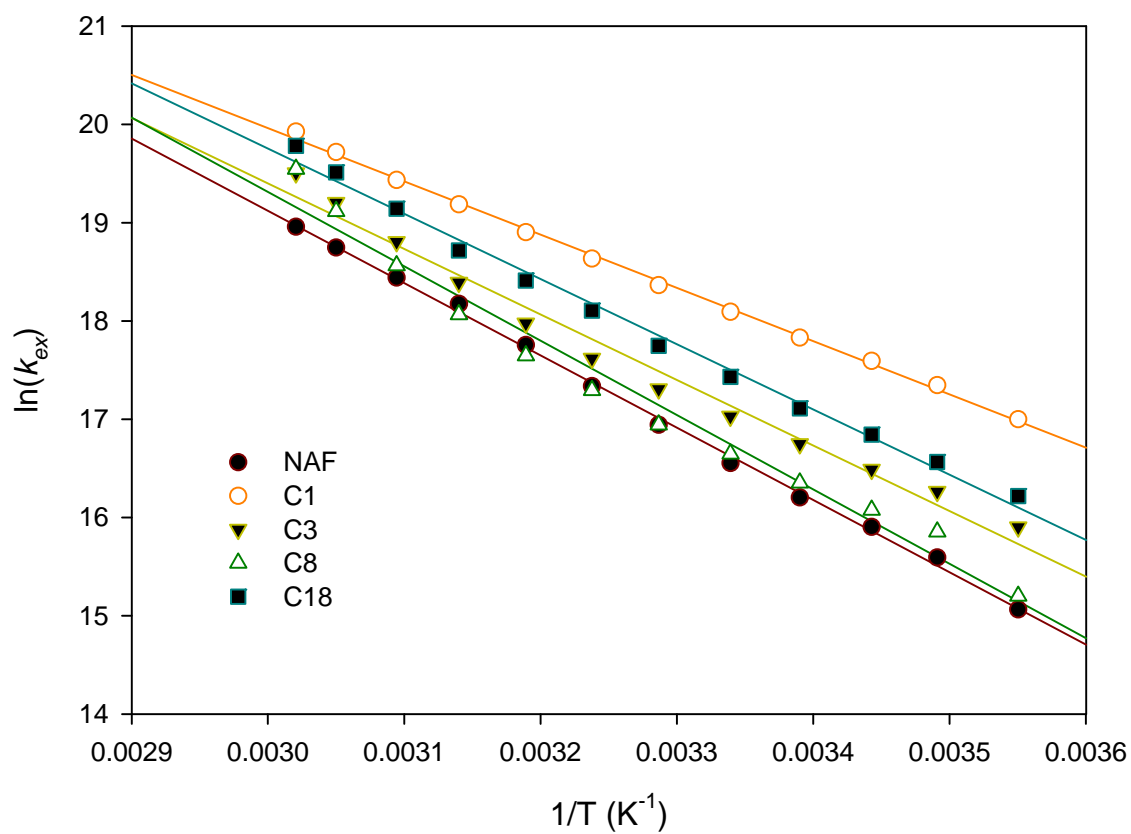
Figure 31. Arrhenius plot of various electrode with individual modifications. Slopes represents activation energy (E_a) and intercept can be converted to pre-exponential factor (A).

Table 21. The slopes (*slope*) and intercepts (*b*) of the Arrhenius Analysis for Various Commercial Particles.

	Naf	C1	C3	C8	C18
b	41.18 ± 0.31	36.22 ± 0.23	39.39 ± 0.88	42.01 ± 1.19	39.66 ± 0.55
$slope(-E_a/R)$	-7352 ± 94	-5420 ± 69	-6664 ± 268	-7267 ± 364	-6635 ± 169
r^2	0.998	0.998	0.984	0.978	0.993
$100\frac{slope}{slope_{Nafion}}$	100	72.5 ± 1.8	90.1 ± 5.5	103 ± 7	89.7 ± 3.6

activation energy (E_a) and pre-exponential factor (A) vlaues can be obtained for each magnetic particle which has different magnetic volume susceptibility. Slopes represent activation energy (E_a) and intercept can be converted to pre-exponential factor (A). Results are tabulated in Table 21.

In Table 21, the last row is the ratio of the activation energy for the magnetic composite relative to the nonmagnetic Nafion film. C1, the composite with the strongest magnetic field, has a 27 % lower activation energy than the Nafion film. C3 and C18 also show activation energies reduced relative to the Nafion film. The composite formed with the lowest reported magnetic susceptibility, C8, has an activation energy that is the same as the nonmagnetic Nafion film. This is consistent with the results in Figures 30 and 31 where the C8 composite data are fully coincident with the Nafion data.

4.3.2.3 Magnetic Susceptibility vs Activation Energy

The relationship between activation energy with magnetic susceptibility for self exchange reaction of $Ru(bpy)^{2+/3+}$ is shown in Figure 32. When volume magnetic susceptibility increases, activation energy for the composite decreases linearly. The
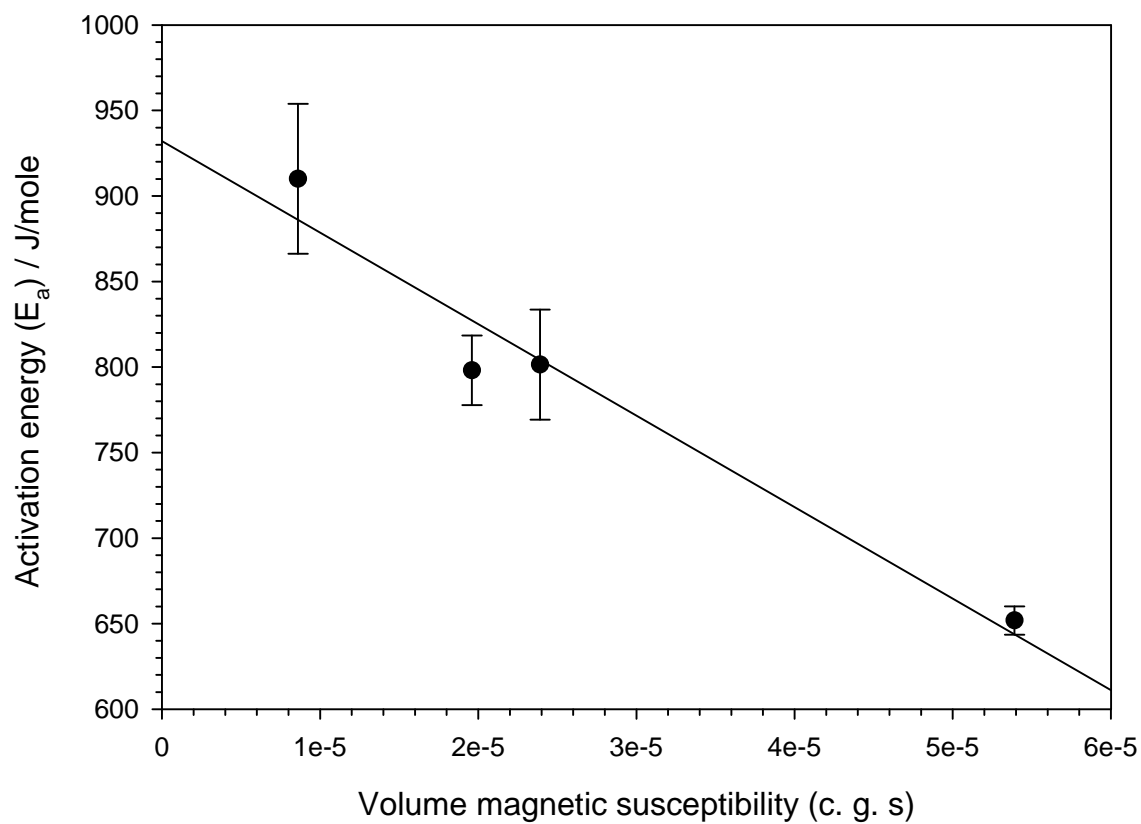
Figure 32. Activation energy (E_a) of $Ru(bpy)^{2+/3+}$ self exchange reaction versus volume magnetic susceptibility. When volume magnetic susceptibility increases, activation energy of the reaction decreases.

Table 22. The slope (E_a/R) and the intercept $(\ln(A))$ of the Arrhenius Analysis for $Co(bpy)_3^{2+/3+}$.

	Naf	Mag
$\ln(A)$	34.09 ± 1.02	25.10 ± 0.64
E_a/R	6594 ± 312	3803 ± 194
R^2	0.982	0.979
% E_a	100	57

intercept of the plot is 932.1 ± 25.6 and the slope is $-5.348 \pm 0.816 \times 10^6$. The R^2 of the regression line is 0.96.

4.3.2.4 Magnetic Susceptibility vs Pre-exponential Factor

The relationship between activation energy with pre-exponential factor for self exchange reaction of $Ru(bpy)^{2+/3+}$ is shown in Figure 33. When volume magnetic susceptibility increases, activation energy for the composite decreases linearly. The intercept of the plot is 41.83 ± 0.51 and the slope is $-1.019 \pm 0.183 \times 10^5$.The R^2 of the regression line is 0.91.

4.3.3 Activation Energy and Pre-exponential Factor of $Co(bpy)_3^{2+/3+}$ Self Exchange Reaction

In Figure 34, $\ln(k_{ex})$ versus $1/T$ for $Co(bpy)_3^{2+/3+}$ on magnetically modified electrode and Nafion modified electrode are plotted. Using Equation 25, E_a/R and $\ln(A)$ values are extracted by linear regression. Slopes of the Nafion and magnetic particles modified electrodes are linear showing R^2 of 0.97 and 0.97, respectively. Percent activation energies relative to Nafion modified electrode are calculated and
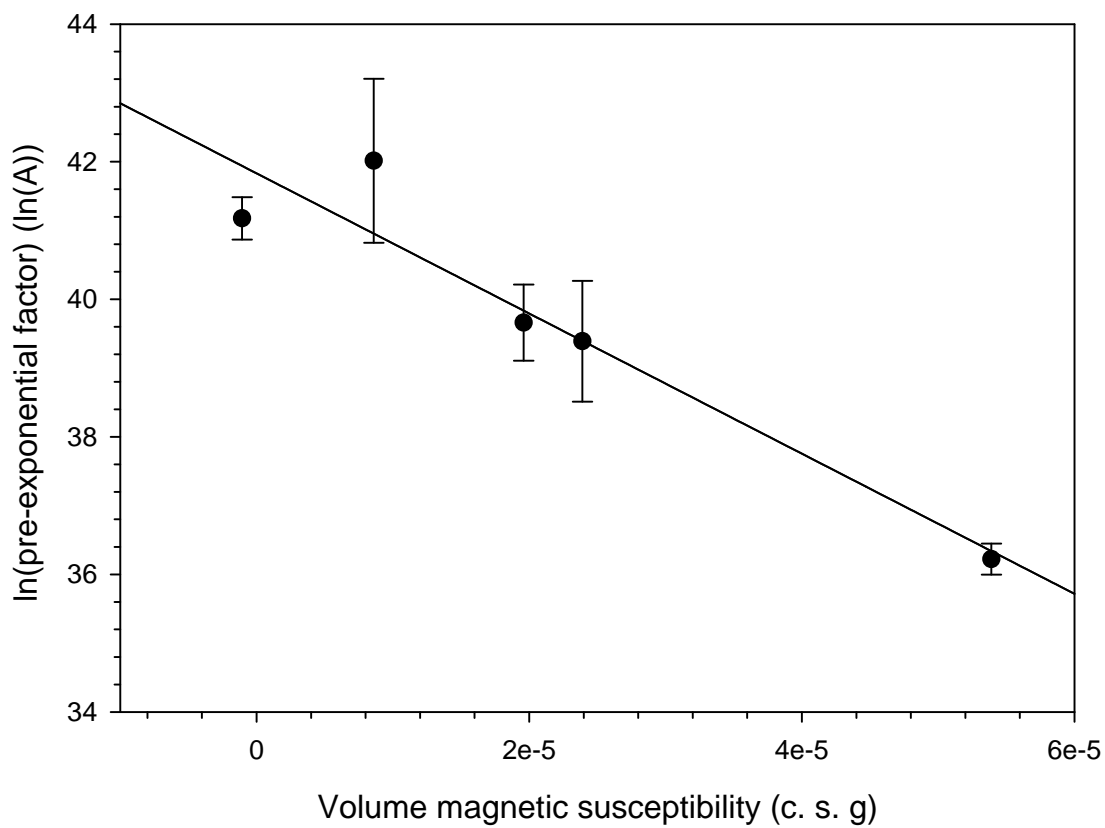
Figure 33. ln(A) of $Ru(bpy)^{2+/3+}$ self exchange reaction versus volume magnetic susceptibility. When volume magnetic susceptibility increases, activation energy of the reaction decreases.
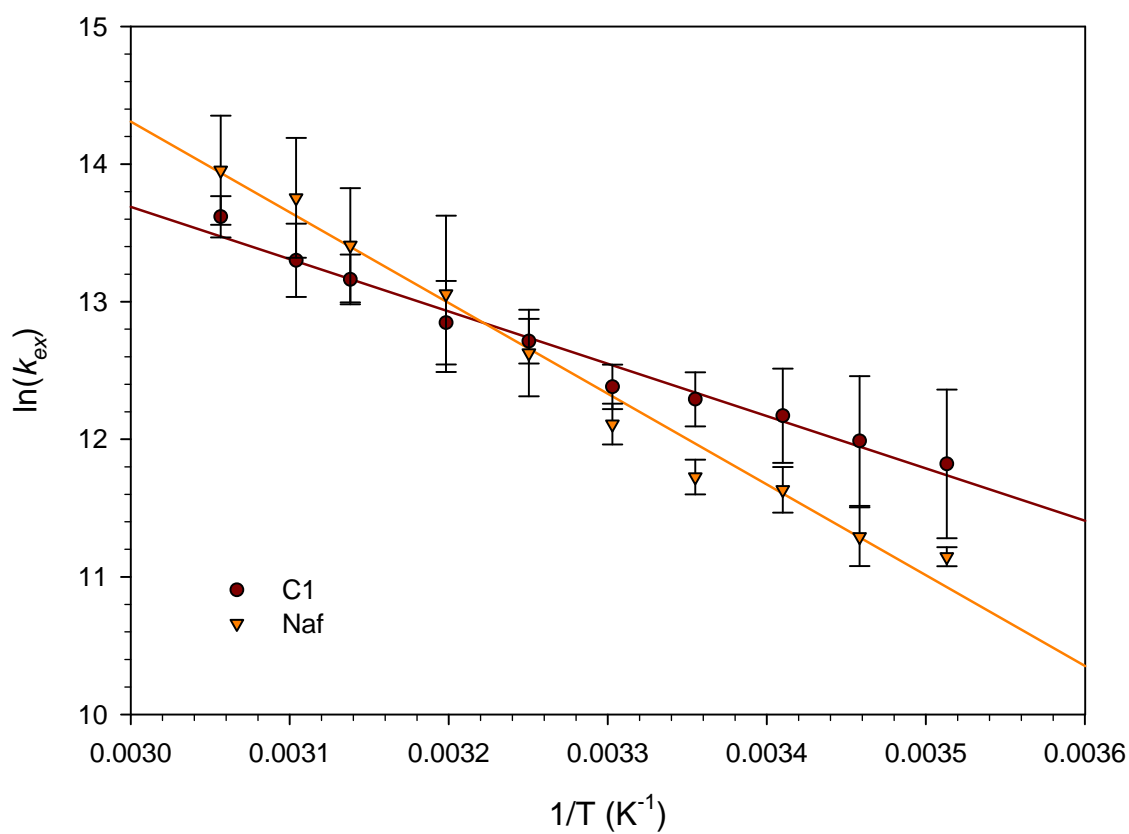
Figure 34. $\ln(k_{ex})$ versus 1/T for $Co(bpy)_3^{2+/3+}$ on magnetically modified electrode and Nafion modified electrode.

Table 23. The slope (E_a/R) and the intercept $(\ln(A))$ of the Arrhenius Analysis for $Co(bpy)_3^{2+/1+}$.

	Naf	Mag
ln(A')	47.13±2.75	34.48 ± 0.27
E_a/R	-10400±50	-6230 ± 34
R^2	0.9308	0.9980
% E_a	100	60

tabulated in Table 22. As a result, it is speculated that magnetic modification reduces the activation energy of $Co(bpy)_3^{2+/3+}$ self exchange reaction 43 %.

4.3.4 Activation Energy and Pre-exponential Factor of $Co(bpy)_3^{2+/1+}$ Self Exchange Reaction

In Figure 35, $\ln(k_{ex})$ versus 1/T for $Co(bpy)_3^{2+/1+}$ on magnetically modified electrode and Nafion modified electrode are plotted. Using Equation 25, E_a/R and $\ln(A)$ values are extracted by linear regression. Slopes of the Nafion and magnetic particles modified electrodes are linear showing R^2 of 0.93 and 0.99, respectively. Percent activation energies relative to Nafion modified electrode are calculated and tabulated in Table 23. As a result, it is speculated that magnetic modification reduces the activation energy of $Co(bpy)_3^{2+/1+}$ self exchange reaction 40 %.

4.3.5 Activation Energy and Pre-exponential Factor of $Os(bpy)_3^{2+/3+}$ Self Exchange Reaction

In Figure 36, $\ln(k_{ex})$ versus 1/T for $Os(bpy)_3^{2+/3+}$ on magnetically modified electrode and Nafion modified electrode are plotted. Using Equation 25, E_a/R and
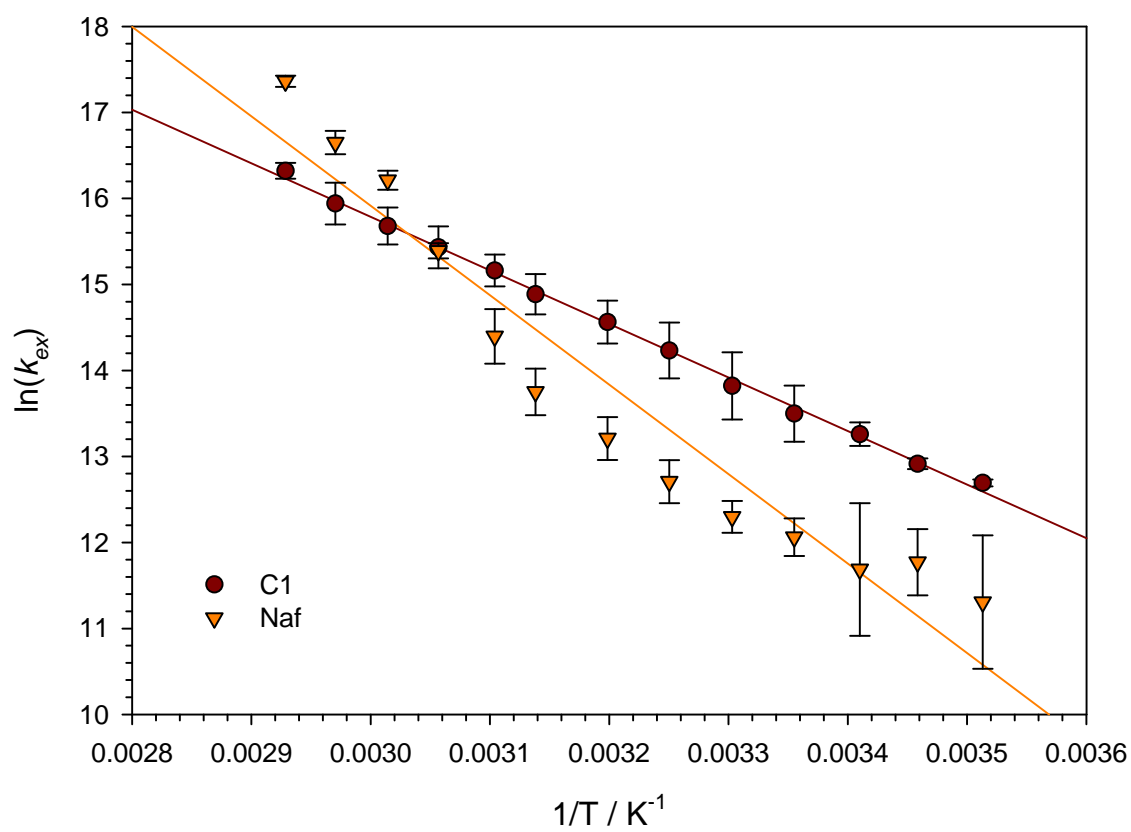
Figure 35. $\ln\left(k_{ex}\right)$ versus 1/T for $\mathrm{Co(bpy)_3^{2+/1+}}$ on magnetically modified electrode and Nafion modified electrode.
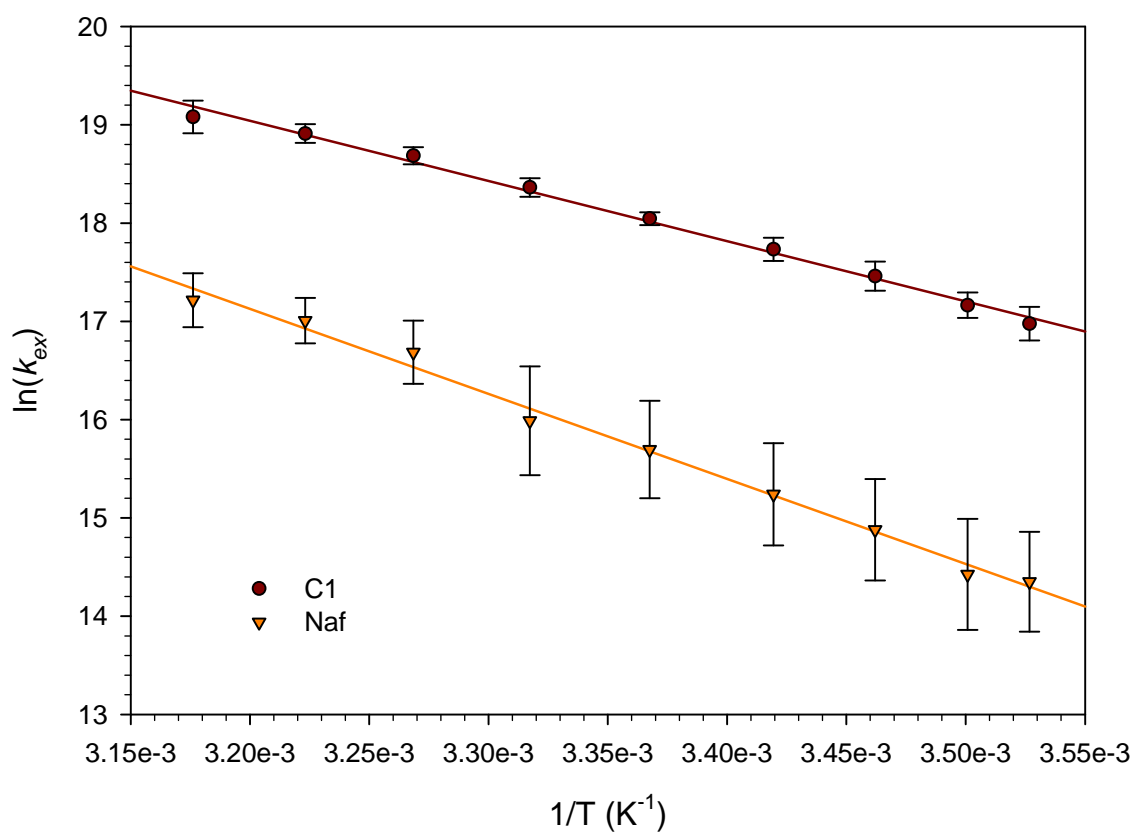
Figure 36. $\ln(k_{ex})$ versus 1/T for $Os(bpy)_3^{2+/3+}$ on magnetically modified electrode and Nafion modified electrode.

Table 24. The slope (E_a/R) and the intercept $(\ln(A))$ of the Arrhenius Analysis for $Os(bpy)_3^{2+/3+}$.

	Naf	Mag
$\ln(A')$	44.83 ± 0.97	38.64 ± 0.57
E_a/R	-8656 ± 288	-6124 ± 170
R^2	0.9923	0.9946
$\% \, E_a$	100	71

$\ln(A)$ values are extracted by linear regression. Slopes of the Nafion and magnetic particles modified electrodes are linear showing R^2 of 0.99 and 0.99, respectively. Percent activation energies relative to Nafion modified electrode are calculated and tabulated in Table 22. As a result, it is speculated that magnetic modification reduces the activation energy of $Os(bpy)_3^{2+/3+}$ self exchange reaction 30 %.

4.4 Model for Magnetic Effects in Self Exchange Reactions

4.4.1 Self Exchange Reactions

Self exchange reactions are a specific class of electron transfer reactions in which the products and reactants are the same species but the electron transfer leads to a transposition of the reactants in space. Consider the two halves of the couple in a tris-bipyridal transition metal complex with oxidation states +2 and +3 that undergoes electron transfer at a standard potential, E^0.

$$M\,(bpy)_3^{3+} + e \rightleftharpoons M\,(bpy)_3^{2+} \tag{26}$$
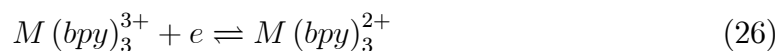
Allow that in a matrix, the two halves of the couple are directly adjacent and

sufficiently close that electron transfer is possible. The most probable electron transfer is when the moieties are in contact, as is assumed in the following. Place reactants $M\left(bpy\right)_3^{2+}$ at position A and $M\left(bpy\right)_3^{3+}$ at position B. Following electron transfer from $M\left(bpy\right)_3^{2+}$ to $M\left(bpy\right)_3^{3+}$, $M\left(bpy\right)_3^{2+}$ will be at position B and $M\left(bpy\right)_3^{3+}$ will be at position A.

$$M\left(bpy\right)_3^{2+}\big|_A + M\left(bpy\right)_3^{3+}\big|_B \rightleftharpoons M\left(bpy\right)_3^{3+}\big|_A + M\left(bpy\right)_3^{2+}\big|_B \tag{27}$$
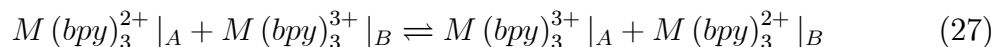
Such processes are known to contribute to charge flux in highly concentrated and slow transport matrices, such as ion exchange polymers.

4.4.1.1 Self Exchange Reactions in Matrices of High Concentration and Slow Transport

Models have been developed for enhanced transport where self exchange processes augment or supplant physical diffusion. Physical diffusion is the process by which a moiety physically moves through space. Dahms [47] and Ruff [48–50, 54] independently developed models for the effective or measured diffusion coefficient, $D_m\left(cm^2/s\right)$, that include the physical diffusion coefficient, D_p, and the self exchange or electron hopping diffusion coefficient, D_{hop}. The self exchange process is embedded in D_{hop} where the self exchange rate is $k_{11}\left(M^{-1}s^{-1}\right)$, $\delta\left(cm\right)$ is the diameter of the reactants, $c^*\left(M\right)$ is the concentration of the reactants, and 6 is a geometrical factor for diffusion in a three dimensional rectilinear coordinate system.

$$D_m = D_p + \frac{k_{11}c^*\delta^2}{6} \tag{28}$$

Measurements in solution, matrices of high D_p, did not reveal significant

contributions to D_m by self exchange. However, from Equation 28, impacts of self exchange on D_m will increase as D_p decreases and c^* increases for a given k_{11}. Conditions of slow transport and high concentration are met when redox probes are adsorbed to electrode surfaces, present in the solid state, and embedded in polymer matrices. Electron hopping by self exchange is an established transport mechanism in ion exchange polymers such as Nafion [55]. For a series of redox couples $M\,(bpy)_3^{2+/3+}$ where $M = Ru$, Os, Cr, and Co, D_p is $\sim 0\,(10^{-12}\ \mathrm{cm^2/s}) << D_{hop}$[2].

Here, data for a variety of magnetic microparticles in Nafion and Nafion films were collected as a function of temperature. Data were evaluated by an Arrhenius analysis. The slope and intercepts of the Arrhenius plots are well correlated with the properties of the magnetic particles. Temperature data were also collected for C1 particles across a set of redox probes. Magnetic effects were again found. The effects were quantified with an Arrhenius analysis. There is greater variability and more parameters to consider in examining the redox probes than in the studies of the microparticles with $Ru\,(bpy)_3^{2+}$. The following is a brief outline of a possible model for the magnetic effects. Some evaluation of the model against the data is presented.

4.4.2   Transition State Theory (TST) for Self Exchange Reactions without Magnetic Effects

Transition state theory (TST) evolved as a model for kinetics based on classical mechanics and an activated complex. TST is also known as activated complex theory and absolute rate theory [56]. In TST, two reactants come together to form an associated pair of reactants held together in a cage of surrounding continuum

media, denoted as follows where $[AB]$ is the activated complex.

$$A + B \rightleftharpoons [AB] \tag{29}$$

The formation of the activated complex is associated with a potential energy barrier of height $\Delta G^{\ddagger}$, the free energy of activation, as shown in Figure 37 for the self exchange reaction $A + B \rightleftharpoons B + A$. The rate of the self exchange reaction is

$$Rate = k_{11} [A] [B] \tag{30}$$
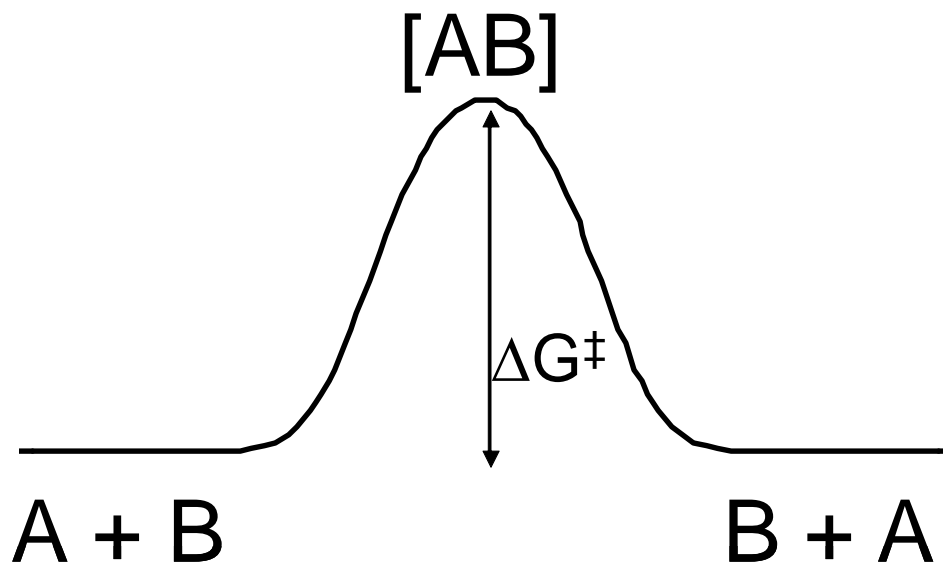
Figure 37. In transition state theory, the reactants, A and B, come together to form an activated complex $[AB]$. The complex is at higher energy than the reactants or products by the free energy of activation, $\Delta G^{\ddagger}$.

In TST, the self exchange rate is expressed as

$$k_{11} = Kk \tag{31}$$

where K is a pre-equilibrium constant that describes the formation of the activated

complex from the available reactants as

$$K = \frac{[AB]}{[A][B]} \tag{32}$$

The pre-equilibrium constant is calculated on a strictly electrostatic basis. K is developed from considerations similar to those for activity effects, such as Debye Hückel theory [57]. In this model, K has units of M^{-1}. Note that in TST, the activated complex is formed as in equilibrium with the reactant and as in equilibrium with the products.

The rate constant, k, for a self exchange reaction is the rate of the electron transfer based on the concentration of the activated complex $[AB]$. Note, that in TST models, the model follows the path of the reaction to the instant of electron transfer. The process as drawn is reversible, but the TST model only considers elementary kinetic steps along the path from the activated complex to the instant of electron transfer. This consideration is particularly important in developing TST models for self exchange reactions where there is no change in the concentration of the reactants and products.

Here, the $\Delta G^{\ddagger}$ embeds free energies associated with the formation of the activated complex and with the subsequent steps to the electron transfer. The rate k is then expressed in an Arrhenius form as

$$k = A \exp\left[-\frac{\Delta G^{\ddagger}}{k_b T}\right] \tag{33}$$

where $k\,(s^{-1})$, k_b is Boltzmann's constant $(1.3806568 \times 10^{-23}\,\mathrm{J\,K^{-1}})$, and T is temperature in Kelvin. This is on a per molecule basis; the form that uses

energies of activation, E_A and the gas constant, R, is on a per mole basis, $k = A \exp\left[-\Delta G^{\ddagger}/RT\right]$. The pre-exponential factor is $A\,(s^{-1})$. In classical TST, A is taken as $k_b T/h$ where h is Planck constant $(6.6260755 \times 10^{-34}\,\mathrm{J\,s})$. It is noted that $k_b T/h$ has units of frequency (s^{-1}).

From the Gibbs equation for the activated complex,

$$\Delta G^{\ddagger} = \Delta H^{\ddagger} - T\Delta S^{\ddagger} \tag{34}$$

where $\Delta H^{\ddagger}$ is the enthalpy of activation and $\Delta S^{\ddagger}$ is the entropy of activation. Enthalpy measures heat and entropy measures disorder. The rate expression is equivalently written as

$$k = A \exp\left[\frac{\Delta S^{\ddagger}}{k_b}\right] \exp\left[-\frac{\Delta H^{\ddagger}}{k_b T}\right] \tag{35}$$

4.4.3 General Considerations for Transition State Theory (TST) That Includes Magnetic Effects

The TST model can be modified to include magnetic effects on the self exchange reactions. Two components are considered here, the re-expression of Equation 35 to segregate magnetic terms and a description of magnetically dependent entropy terms based on probabilities. It is noted that all self exchange reactions considered here are outer sphere reactions that do not undergo structural changes on electron transfer; that is, the reactions are simple.

The total enthalpy of activation is segregated into two parts, $\Delta H_0^{\ddagger}$ and $\Delta H_m^{\ddagger}$, the enthalpy not subject to magnetic effects and the enthalpy dependent on the magnetic effects, respectively. Segregation of thermodynamic parameters into two

enthalpies is consistent with compounds in the magneto electrochemical potential. The two components are taken as independent and to represent the total enthalpy of activation as a sum.

$$\Delta H^{\ddagger} = \Delta H_0^{\ddagger} + \Delta H_m^{\ddagger} \tag{36}$$

Analogous definitions are provided for the entropy where $\Delta S_0^{\ddagger}$ is the magnetically independent entropy term and $\Delta S_m^{\ddagger}$ is the magnetically dependent entropy term. Then, based on common thermodynamic methodes,

$$\Delta S^{\ddagger} = \Delta S_0^{\ddagger} + \Delta S_m^{\ddagger} \tag{37}$$

Equation 35 is

$$k = A \exp\left[\frac{\Delta S_0^{\ddagger}}{k_b}\right] \exp\left[\frac{\Delta S_m^{\ddagger}}{k_b}\right] \exp\left[-\frac{\Delta H_0^{\ddagger}}{k_b T}\right] \exp\left[-\frac{\Delta H_m^{\ddagger}}{k_b T}\right] \tag{38}$$

In this framework, effects of magnetic fields are expressed in enthalpy and entropy and the magnetic effects are segregated from non-magnetic enthalpy and entropy.

The second consideration is the entropy based on the probability of states that arises in statistical thermodynamics. The entropy for a single species is defined as

$$\frac{S}{k_b} = -\sum_i P_i \ln P_i \tag{39}$$

where the species has several assessable states and the probability of the species being in a state i is P_i. The entropy associated with magnetic effects will be developed from Equation 39. The probabilities of interest are the probabilities of the species being in a particular spin state. For example, in the absence of an applied magnetic field, an unpaired electron has two states, one spin up and one spin down. Then, $S/k_b = -\left(0.5\ln(0.5) + 0.5\ln(0.5)\right) = -\ln(0.5) = 0.693$. Note also that the

calculation of ΔS requires application of Equation 39 to an initial and final state.

4.4.4 TST Modified for Magnetic Effects in Self Exchange Reactions of Singlet-Doublets

Several of the transition metal couples, $M\,(bpy)_3^{2+/3+}$, have one half of the couple that is diamagnetic and one half that has a single unpaired electron, a paramagnetic radical. These two states are a singlet (S) and a double (D), respectively. The self exchange reaction for these systems is

$$M\,(bpy)_3^{2+}\,|_A + M\,(bpy)_3^{3+}\,|_B \rightleftharpoons M\,(bpy)_3^{3+}\,|_A + M\,(bpy)_3^{2+}\,|_B \qquad (40)$$

$$S|_A + D|_B \rightleftharpoons D|_A + S|_B \qquad (41)$$
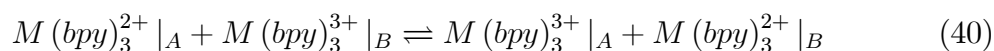
$M\,(bpy)_3^{2+}$ is the singlet and $M\,(bpy)_3^{3+}$ is the doublet (radical of one unpaired electron) when M is from Group 6B of the periodic table: $M\,=\,Fe,\,Ru,$ or Os. Tris-bipyridal complexes are octahedral. For Group 6B, $M\,(bpy)_3^{2+}$ is d^6 and $M\,(bpy)_3^{3+}$ is d^5. The energy levels are filled as shown.
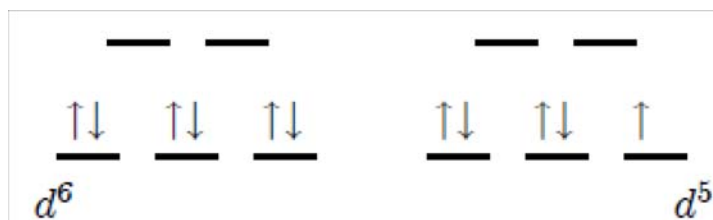
For reaction between a singlet and a radical, magnetic effects couple into the system through electron nuclear spin polarization (ensp). ensp is the process by which the electron spin on the radical couples to the nuclear spin of the singlet when

both are in the cage complex. ensp is important to effective isoenergetic electron transfer. Within the framework of TST, in the presence of a sufficient applied magnetic field, the radical is polarized by the magnetic field. The pre-polarized radical and singlet form a cage complex where the spin is localized on the radical. The system undergoes electron nuclear spin polarization such that the spin is delocalized over the entire cage. This state is represented as the spin delocalized over the cage complex by superscript D on the bracket that represents the cage complex. The isoenergetic electron transfer occurs within the cage while the spin is delocalized across the cage; this is represented by the arrow.

$$\left[\text{↑↓ ↑↓ ↑↓ \quad ↑ ↑↓ ↑↓} \right]^{D}$$
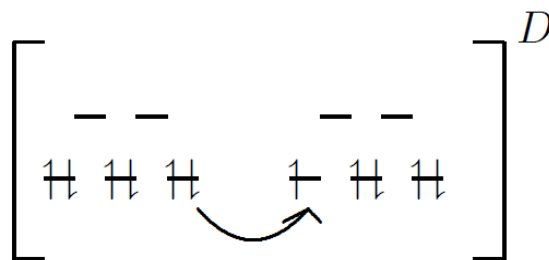
The energetics of this process are shown in Figure 38. The curve for no magnetic effects is shown in grey with a barrier height of $\Delta G_0^{\ddagger}$, the free energy of activation. The magnetic effects are represented by the blue curve where the top of the energy barrier is split into two states. The cage with the spin localized on the radical, $\left[SD^{\uparrow}\right]$, is raised in energy above $\Delta G_0^{\ddagger}$ by an amount $gHS\beta$ and the cage with the spin delocalized over the entire cage, $[SD]^{\uparrow}$, is lowered in energy below $\Delta G_0^{\ddagger}$ by $gHS\beta$.

For $[SD]^{\uparrow}$, the system is fully configured for effective isoenergetic electron transfer,

which is a state slightly lower in energy than $[SD^\uparrow]$. The two energies differ by $2gHS\beta$. There are additional entropy advantages to the electron nuclear spin polarized states that accrue with delocalized spin; this contributes to lower $\Delta G^\ddagger$

The experimental determined g measures the response of the radical to an applied magnetic field, S is spin, determined from g and equal to $1/2$ for a doublet, H is the strength of the applied magnetic field, and β is a constant, the Bohr magneton $\left(9.2740154 \times 10^{-24}\,\mathrm{J\,T^{-1}}\right)$. The Zeeman energy, $gHS\beta$ is small compared to k_bT.
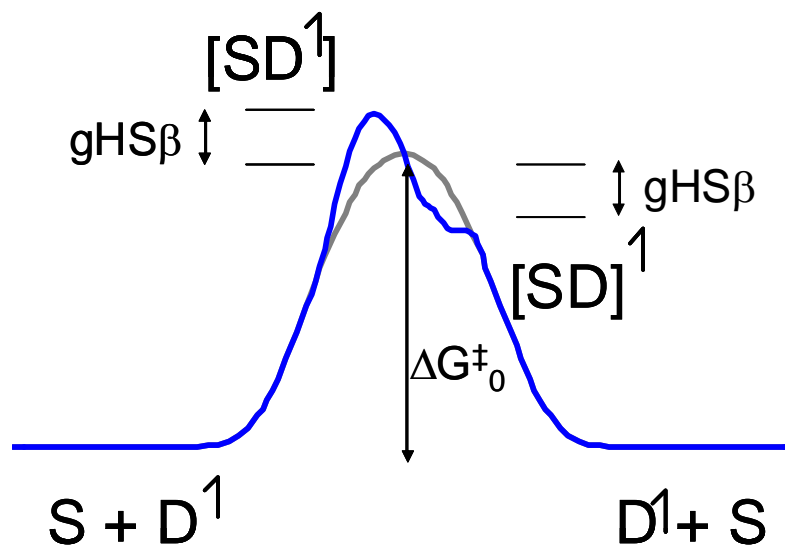
Figure 38. For a self exchange reaction between a singlet (S) and a doublet ($D^\uparrow$), a cage complex is formed, $[SD^\uparrow]$ where the spin is localized on the doublet within the cage. The spin is then delocalized over the entire cage complex by electron nuclear spin polarization to form $[SD]^\uparrow$. The isoenergetic electron transfer occurs within the cage to form $[DS]^\uparrow$. The cage with localized spin, $[SD^\uparrow]$, has energy elevated slightly above the free energy of activation in the absence of magnetic effects, $\Delta G_0^\ddagger$, to $\Delta G_0^\ddagger + gHS\beta$. The spin delocalized cage complex has a slightly lower energy, $\Delta G_0^\ddagger - gHS\beta$. In the Figure, the gray curve represents the barrier when no magnetic effects are considered.

$$[SD^\uparrow]$$

$$k_1 \big\Updownarrow k_{-1}$$

$$[SD]^\uparrow \underset{k_{-2}}{\overset{k_2}{\rightleftharpoons}} [DS]^\uparrow$$

$$K_A \qquad\qquad\qquad K_A$$

$$S + D^\uparrow \qquad\qquad\qquad D^\uparrow + S$$
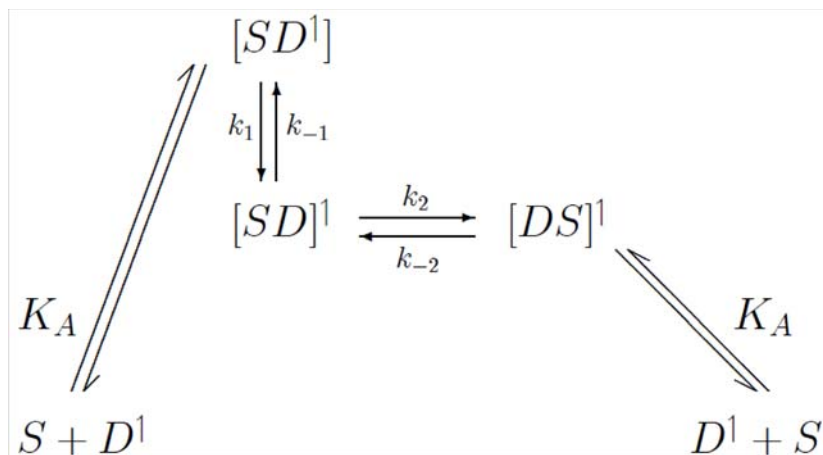
The sequence of steps is represented as follows, where energy increases along the y axis. Several points are evident. First, the pre-equilibrium constant, K, is calculated from a purely electrostatic model. The energetics of the two states $\left[SD^\uparrow\right]$ and $[SD]^\uparrow$ could in principle be included in the pre-equilibrium constant to distribute the cage complexes between localized and delocalized spin. But the energy differences between the two states are small and the redistribution between the states upon electron nuclear spin polarization is characterized by the kinetic steps. Thus, the strictly electrostatic calculation of K is used to determine the concentration of the cage complex and, because of the similar energies of the delocalized and localized complexes, the concentrations are approximated as equal.

$$\frac{1}{2} K \left[S\right] \left[D^\uparrow\right] \cong \left[SD^\uparrow\right] \cong [SD]^\uparrow \tag{42}$$

Further refinements are possible, but this suffices for the current development. Second, the reaction between $\left[SD^\uparrow\right]$ and $[SD]^\uparrow$ is modeled as a forward rate of electron nuclear spin polarization, k_1 and a backward rate where the spin is again

localized on the radical within the complex, k_{-1}. Third, there is no energy change associated with the isoenergetic forward and backward electron transfer rates within the cage, k_2 and k_{-2}, respectively. Fourth, once the spin is polarized by the applied field, the spin is inherited up until the instance of electron transfer. Spin does not spontaneously flip once it is oriented by the applied field. Finally, in TST, it is only necessary to map the kinetic processes up to the instant of electron transfer, here step k_2. The rate is based on the concentration of $[SD]^{\uparrow}$.

The rate expression for the process is dependent on expressing the concentration of $[SD]^{\uparrow}$ subject to generation and loss. The mechanism is traced to the instant of electron transfer, the isoenergetic and spin invariant rate, k_2.

$$Rate \;=\; k_2 \, [SD]^{\uparrow} \tag{43}$$

$$=\; k_2 \left(k_1 \left[SD^{\uparrow} \right] - k_{-1} \left[SD \right]^{\uparrow} \right) \tag{44}$$

$$=\; \frac{1}{2} K \left[S \right] \left[D^{\uparrow} \right] \left(k_1 - k_{-1} \right) k_2 \tag{45}$$

The measured self exchange rate, $k_{11} = K \left(k_1 - k_{-1} \right) k_2$. Because k_2 is isoenergetic and does not change entropy states, including spin, k_2 is unity. The rates k_1 and k_{-1} are expressed within TST as follows. Note the entropy terms are not yet expressed.

$$k_1 = A \exp \left[\frac{\Delta S^{\ddagger}}{k_b} \right] \exp \left[-\frac{\Delta H_{0'}^{\ddagger} - gHS\beta}{k_b T} \right] \tag{46}$$

$$k_{-1} = A \exp \left[\frac{\Delta S^{\ddagger}}{k_b} \right] \exp \left[-\frac{\Delta H_{0'}^{\ddagger} + gHS\beta}{k_b T} \right] \tag{47}$$

The measured self exchange rate is now expressed as

$$k_{11} = KA \exp\left[\frac{\Delta S^\ddagger}{k_b}\right] \left\{\exp\left[-\frac{\Delta H^\ddagger_{0'} - gHS\beta}{k_b T}\right] - \exp\left[-\frac{\Delta H^\ddagger_{0'} + gHS\beta}{k_b T}\right]\right\} \quad (48)$$

Consider the magnetic component of the entropy term. The complex $[SD^\uparrow]$ has

one unpaired spin and it can be present in one of two states, spin up and spin down.

The probability of either state is 1/2. The entropy for the state is then

$$\frac{S^\ddagger_m\left([SD^\uparrow]\right)}{k_b} = -\sum_i P_i \ln P_i = -\sum_{i=1}^{2} \frac{1}{2} \ln\left(\frac{1}{2}\right) = -\ln\left(\frac{1}{2}\right) \quad (49)$$

The spin is taken as inherited, so the entropy from magnet effects for $[SD]^\uparrow$ is zero

because there is only one allowed spin state.

$$\frac{S^\ddagger_m\left([SD]^\uparrow\right)}{k_b} = -\sum_i P_i \ln P_i = -\sum_{i=1}^{1} 1 \ln(1) = -\ln(1) = 0 \quad (50)$$

The difference in the entropies is based on the difference in delocalized and localized

spin for the cage complex.

$$\frac{\Delta S^\ddagger_m}{k_b} = \frac{S^\ddagger_m\left([SD]^\uparrow\right)}{k_b} - \frac{S^\ddagger_m\left([SD^\uparrow]\right)}{k_b} = \ln\left(\frac{1}{2}\right) \quad (51)$$

Upon substitution of $\Delta S^\ddagger_m$, the above rate expression becomes

$$k_{11} = KA \exp\left[\frac{\Delta S^\ddagger_0}{k_b}\right] \exp\left[\frac{\Delta S^\ddagger_m}{k_b}\right] \exp\left[-\frac{\Delta H^\ddagger_{0'}}{k_b T}\right] \left\{\begin{array}{c} \exp\left[\frac{gHS\beta}{k_b T}\right] \\ -\exp\left[-\frac{gHS\beta}{k_b T}\right] \end{array}\right\} \quad (52)$$

$$= KA \exp\left[\frac{\Delta S^\ddagger_0}{k_b}\right] \exp\left[-\frac{\Delta H^\ddagger_{0'}}{k_b T}\right] \exp\left[\ln\left(\frac{1}{2}\right)\right] \left\{\begin{array}{c} \exp\left[\frac{gHS\beta}{k_b T}\right] \\ -\exp\left[-\frac{gHS\beta}{k_b T}\right] \end{array}\right\} \quad (53)$$

$$= KA \exp\left[\frac{\Delta S^\ddagger_0}{k_b}\right] \exp\left[-\frac{\Delta H^\ddagger_{0'}}{k_b T}\right] \underbrace{\left(\frac{1}{2}\right)}_{\exp\left[\frac{\Delta S^\ddagger_m}{k_b}\right]} \underbrace{\left\{\begin{array}{c} \exp\left[\frac{gHS\beta}{k_b T}\right] \\ -\exp\left[-\frac{gHS\beta}{k_b T}\right] \end{array}\right\}}_{\exp\left[-\frac{\Delta H^\ddagger_m}{k_b T}\right]} \quad (54)$$

For no sufficient applied magnetic field, the entropy for the SD reaction is 1/2.

When a sufficient magnetic field is applied, the spins are all pre-polarized by the field, and the entropy term is 1, no uncertainty about the state because there is only one state.

For the state where the systems are identical except that one has a sufficient magnetic field applied, $\Delta G_0^{\ddagger}$ is the same as are the collision frequency and pre-equilibrium constant. The expression for the enthalpy for $k_{11}(0)$ comes from the expression for no magnetic effects, Equation 35. The entropy is calculated as above. The ratio of k_{11} in an applied field H as compared to no applied field, $H = 0$, is

$$\frac{k_{11}(H)}{k_{11}(0)} = -\frac{KA\exp\left[\frac{\Delta S_0^{\ddagger}}{k_b}\right]\exp\left[-\frac{\Delta H_{0'}^{\ddagger}}{k_bT}\right]1\left\{\exp\left[\frac{gHS\beta}{k_bT}\right] - \exp\left[-\frac{gHS\beta}{k_bT}\right]\right\}}{KA\exp\left[\frac{\Delta S_0^{\ddagger}}{k_b}\right]\exp\left[-\frac{\Delta H_{0'}^{\ddagger}}{k_bT}\right]\frac{1}{2}} \tag{55}$$

Several notes are made based on this ratio and Equation 54. First, for a SD reaction, the ratio shows that the rate is doubled by applying a sufficient field because the degeneracy of the spins is removed. Second, from Equation 54, the approximation that

$$\lim_{x\to 0}\exp\left[x\right] \to 1 + x... \tag{56}$$

and the note that $gHS\beta << k_bT$, $k_{11}(H)$ can be expressed as

$$k_{11}(H) = KA\exp\left[\frac{\Delta S_0^{\ddagger}}{k_b}\right]\exp\left[-\frac{\Delta H_{0'}^{\ddagger}}{k_bT}\right]1\left\{\begin{array}{c}\exp\left[\frac{gHS\beta}{k_bT}\right]\\ -\exp\left[-\frac{gHS\beta}{k_bT}\right]\end{array}\right\} \tag{57}$$

$$= KA\exp\left[\frac{\Delta S_0^{\ddagger}}{k_b}\right]\exp\left[-\frac{\Delta H_{0'}^{\ddagger}}{k_bT}\right]1\left\{\begin{array}{c}1 + \frac{gHS\beta}{k_bT}\\ -\left(1 - \frac{gHS\beta}{k_bT}\right)\end{array}\right\} \tag{58}$$

$$= KA\exp\left[\frac{\Delta S_0^{\ddagger}}{k_b}\right]\exp\left[-\frac{\Delta H_{0'}^{\ddagger}}{k_bT}\right]1\left\{2\frac{gHS\beta}{k_bT}\right\} \tag{59}$$

The rate is directly proportional to $gHS\beta$. Third, the collision frequency, A is taken

as $k_b T/h$ in classical TST. If this is substituted into the k_{11} expression, the result is

$$k_{11}(H) = K\frac{k_b T}{h}\exp\left[\frac{\Delta S_0^\ddagger}{k_b}\right]\exp\left[-\frac{\Delta H_{0'}^\ddagger}{k_b T}\right]1\left\{2\frac{gHS\beta}{k_b T}\right\} \tag{60}$$

$$= K\frac{2gHS\beta}{h}\exp\left[\frac{\Delta S_0^\ddagger}{k_b}\right]\exp\left[-\frac{\Delta H_{0'}^\ddagger}{k_b T}\right] \tag{61}$$

Two additional points of interest are of note. The collision frequency is no longer temperature dependent, $2gHS/h$. The ratio $gHS\beta/h$ is the frequency for the magnetic effects and it is substantially lower than the time constant $k_b T/h$. This frequency $gHS\beta/h$ may account for the lack of temperature dependence typically observed for Arrhenius plots ($\ln k$ vs $1/T$) made for rate analyses.

4.4.5 TST Extended to Other Reaction Mechanisms and Incorporation of Prepolarization of the Reactants

The model for the self exchange reaction between singlet and doublet states is extended to other singlet radical reactions and is applicable to radical-radical reactions. For radical-radical reactions, that electron spin polarization may have to be considered, is under consideration which may require additional experimental studies for verification.

The model is modified to allow a prepolarization step that polarizes the spins of the reactants when there is an applied magnetic field. This prepolarization has two impacts. First, the applied field reduces the entropy because there is only one probable state for the spins in the field. A consequence of that in the absence of the applied field, the entropy terms are large for radical-radical reactions, such as TQ reactions, and the rates are slow. Radical-radical reactions can be dramatically
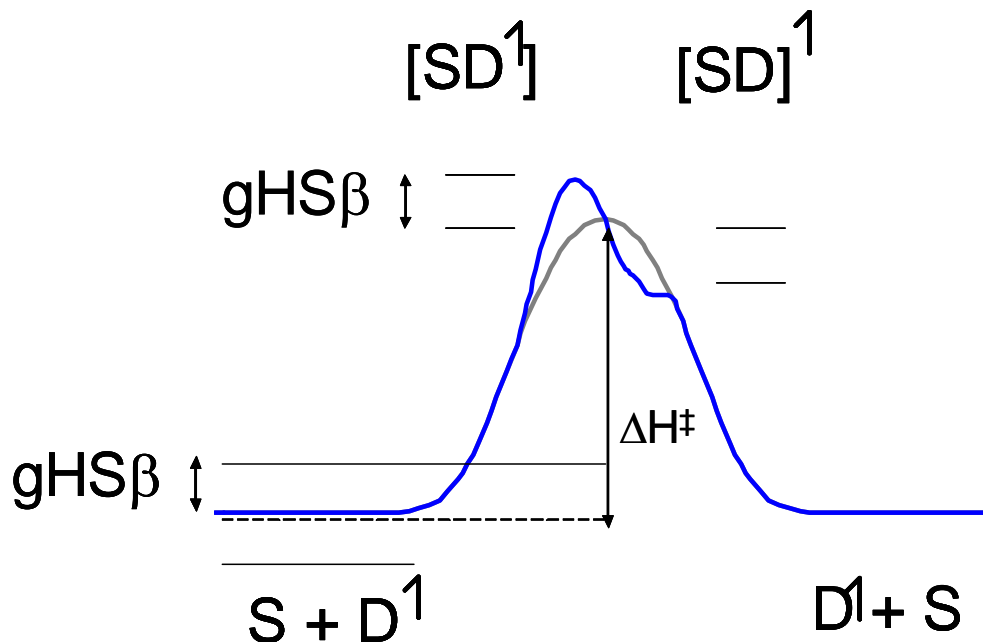
Figure 39. Energetic states of TST with pre-polarization.

impacted by applied fields because the field reduces the spin entropy of the reactants. Second, the prepolarization of the reactants raises their reference energetic state by a Zeeman energy, $gSH\beta$, relative to the reactant energy when there is no applied field. Thus, the net enthalpy of activation barrier is reduced and the reaction rate facilitated. In the model with the prepolarization, the entropy associated with the spin is now moved into $\Delta S_p^{\ddagger}$ for the prepolarization step. $\Delta S_0^{\ddagger}$ remains magnetically independent and is $\Delta S_0^{\ddagger}$.

The rate expression for the self exchange rate is now the product of the prepolarization rate, k_p, the the self exchange process developed above. Note that when two radicals react, gS is replaced with ΔgS.

$$k_{ex} = K \exp\left[\frac{\Delta S_p^{\ddagger}}{k_b}\right] \underbrace{\exp\left[+\frac{gHS\beta}{k_bT}\right]}_{k_p} \tag{62}$$

$$\underbrace{\times A \exp\left[\frac{\Delta S_0^{\ddagger}}{k_b}\right] \left\{ \begin{array}{l} \exp\left[\frac{-\left[\left(\Delta H_{0'}^{\ddagger}\right)-gHS\beta\right]}{k_bT}\right] \\ -\exp\left[\frac{-\left[\left(\Delta H_{0'}^{\ddagger}\right)+gHS\beta\right]}{k_bT}\right] \end{array} \right\}}_{ket} \tag{63}$$

Rearranging,

$$k_{ex} = KA \exp\left[\frac{\Delta S_p^{\ddagger}}{k_b}\right] \exp\left[\frac{\Delta S_0^{\ddagger}}{k_b}\right] \tag{64}$$

$$\times \exp\left[+\frac{gHS\beta}{k_bT}\right] \left\{ \begin{array}{l} \exp\left[\frac{-\left[\left(\Delta H_{0'}^{\ddagger}\right)-gHS\beta\right]}{k_bT}\right] \\ -\exp\left[\frac{-\left[\left(\Delta H_{0'}^{\ddagger}\right)+gHS\beta\right]}{k_bT}\right] \end{array} \right\} \tag{65}$$

$$= KA \exp\left[\frac{\Delta S_p^{\ddagger}}{k_b}\right] \exp\left[\frac{\Delta S_0^{\ddagger}}{k_b}\right] \exp\left[+\frac{gHS\beta}{k_bT}\right] \tag{66}$$

$$\times \exp\left[-\frac{\Delta H_{0'}^{\ddagger}}{k_bT}\right] \left\{ \begin{array}{l} \exp\left[\frac{gHS\beta}{k_bT}\right] \\ -\exp\left[\frac{-gHS\beta}{k_bT}\right] \end{array} \right\} \tag{67}$$

$$= KA \exp\left[\frac{\Delta S_p^{\ddagger}}{k_b}\right] \exp\left[\frac{\Delta S_0^{\ddagger}}{k_b}\right] \tag{68}$$

$$\times \exp\left[-\frac{\left(\Delta H_{0'}^{\ddagger} - gHS\beta\right)}{k_bT}\right] \left\{ \begin{array}{l} \exp\left[\frac{gHS\beta}{k_bT}\right] \\ -\exp\left[\frac{-gHS\beta}{k_bT}\right] \end{array} \right\} \tag{69}$$

Then, from Arrhenius plot

$$
\ln\left[k_{ex}\right] = \ln K + \ln A + \frac{\Delta S_p^{\ddagger}}{k_b} + \frac{\Delta S_0^{\ddagger}}{k_b} \tag{70}
$$

$$
+ \left[-\frac{\left(\Delta H_{0'}^{\ddagger} - gHS\beta\right)}{k_bT}\right] + \ln\left\{\frac{\exp\left[\frac{gHS\beta}{k_bT}\right]}{-\exp\left[\frac{-gHS\beta}{k_bT}\right]}\right\} \tag{71}
$$

$$
= \ln K + \ln A + \frac{\Delta S_p^{\ddagger}}{k_b} + \frac{\Delta S_0^{\ddagger}}{k_b} \tag{72}
$$

$$
-\frac{\Delta H_{0'}^{\ddagger} - gHS\beta}{k_bT} + \ln\left\{\frac{\exp\left[\frac{gHS\beta}{k_bT}\right]}{-\exp\left[\frac{-gHS\beta}{k_bT}\right]}\right\} \tag{73}
$$

Now simplify $\exp\left[\frac{gHS\beta}{kT}\right] - \exp\left[\frac{-gHS\beta}{kT}\right]$ by noting that

$$
\lim_{x\to 0} e^x \to 1 + x \tag{74}
$$

$$
\lim_{gHS\beta/kT\to 0}\left\{\exp\left[\frac{gHS\beta}{k_bT}\right] - \exp\left[\frac{-gHS\beta}{k_bT}\right]\right\} = 1 + \frac{gHS\beta}{k_bT} - \left(1 - \frac{gHS\beta}{k_bT}\right) \tag{75}
$$

$$
= \frac{2gHS\beta}{k_bT} \tag{76}
$$

So

$$
\ln k_{ex} = \ln K + \ln A + \frac{\Delta S_p^{\ddagger}}{k_b} + \frac{\Delta S_0^{\ddagger}}{k_b} - \frac{\Delta H_{0'}^{\ddagger} - gHS\beta}{k_bT} + \ln\left[\frac{2gHS\beta}{k_bT}\right] \tag{77}
$$

$$
= \ln K + \ln A + \ln\left[\frac{2gHS\beta}{k_bT}\right] + \frac{\Delta S_p^{\ddagger}}{k_b} + \frac{\Delta S_0^{\ddagger}}{k_b} - \frac{\Delta H_{0'}^{\ddagger} - gHS\beta}{k_bT} \tag{78}
$$

If

$$
A = \frac{kT}{h} \tag{79}
$$

This becomes

$$
\ln k_{ex} = \ln K + \ln\left[\frac{2gHS\beta}{h}\right] + \frac{\Delta S_p^{\ddagger}}{k_b} + \frac{\Delta S_0^{\ddagger}}{k_b} - \frac{\Delta H_{0'}^{\ddagger} - gHS\beta}{k_bT} \tag{80}
$$

Equilibrium constant $K = \exp\left(\frac{-\Delta G_o^{\ddagger}}{kT}\right)$, then

$$
\begin{aligned}
\ln k_{ex} &= \frac{-\Delta G_o^{\ddagger}}{k_b T} + \ln\left[\frac{2gHS\beta}{h}\right] + \frac{\Delta S_p^{\ddagger}}{k_b} + \frac{\Delta S_0^{\ddagger}}{k_b} - \frac{\Delta H_{0'}^{\ddagger} - gHS\beta}{k_b T} \tag{81} \\
&= -\frac{\Delta H_o^{\ddagger}}{k_b T} + \frac{\Delta S_o^{\ddagger}}{k_b} + \ln\left[\frac{2gHS\beta}{h}\right] + \frac{\Delta S_p^{\ddagger}}{k_b} + \frac{\Delta S_0^{\ddagger}}{k_b} - \frac{\Delta H_{0'}^{\ddagger} - gHS\beta}{k_b T} \tag{82}
\end{aligned}
$$

Because spin states are inherited $\Delta S_o^{\ddagger} = 0$, then

$$
\ln k_{ex} = \ln\left[\frac{2gHS\beta}{h}\right] + \frac{\Delta S_p^{\ddagger}}{k_b} + \frac{\Delta S_0^{\ddagger}}{k_b} - \frac{\Delta H_o^{\ddagger} + \Delta H_{0'}^{\ddagger} - gHS\beta}{k_b T}
$$

$\Delta H_{0'}^{\ddagger} \simeq 0$ because energy state of $\left[SD^{\uparrow}\right]$ and $\left[SD^{\uparrow}\right]$ is almost same.

$$
\ln k_{ex} = \ln\left[\frac{2gHS\beta}{h}\right] + \frac{\Delta S_p^{\ddagger}}{k_b} + \frac{\Delta S_0^{\ddagger}}{k_b} - \frac{\Delta H_o^{\ddagger} - gHS\beta}{k_b T}
$$

Note the time constant for the magnetic effect is

$$
\tau_{magEff} = \frac{h}{gHS\beta} \tag{83}
$$

Arrhenius plots from Equation 80 yield intercepts (b) and slopes ($slope$).

$$
\begin{aligned}
b &= \ln\left[\frac{2gHS\beta}{h}\right] + \frac{\Delta S_p^{\ddagger}}{k_b} + \frac{\Delta S_0^{\ddagger}}{k_b} \tag{84} \\
slope &= -\frac{\Delta H_0^{\ddagger} - gHS\beta}{k_b} = -\frac{\Delta H_0^{\ddagger}}{k_b}\left[1 - \frac{gHS\beta}{\Delta H_0^{\ddagger}/k_b}\right] \tag{85}
\end{aligned}
$$

4.4.5.1 Considerations of $\Delta S_p^{\ddagger}$

The sources of the $\Delta S_p^{\ddagger}$ is the unpaired spins on the reactants before the formation of the cage complex. The model is that when there is a sufficiently large magnetic field H, the spins are prepolarized into a single spin configuration and there is no multiplicity of spin states. When the field is not sufficiently large or $H \rightarrow 0$, then

the full multiplicity of spin states is described by Boltzmann's statistical mechanical description. That is, for i states where each state has a probability P_i, the entropy is

$$\frac{S}{k_b} = -\sum_{i=1} P_i \ln P_i \tag{86}$$

Consider a species with m unpaired spins. The number of spin states is $\frac{1}{2^m}$. For a doublet, D, there is one unpaired electron that can be either up or down, so the probability of each state is $\frac{1}{2^1}$. The entropy for D is then

$$\left.\frac{S_p}{k_b}\right|_D = -\sum_{i=1} P_i \ln P_i = -\left[\frac{1}{2}\ln\left[\frac{1}{2}\right] + \frac{1}{2}\ln\left[\frac{1}{2}\right]\right] = -\ln\left[\frac{1}{2}\right] = \ln[2] = 0.693 \tag{87}$$

If there is sufficient H then $-S/k_b \to 0$ and there is no entropy for the prepolarized D but the initial energy is shifted by the Zeeman energy $gSH\beta$.

The triplet T has $m = 2$ and the quartet Q has $m = 3$. So, for the *unpolarized* radicals where every state has probability $1/2^m$, Equation 86 becomes

$$\frac{S_p}{k_b} = -\sum_{i=1}^{m^2} P_i \ln P_i = -\ln\frac{1}{2^m} = m\ln 2 = 0.693m \tag{88}$$

To arrive at $\Delta S_p^\ddagger$, it is necessary to consider the product, the cage complex as it is first formed, and the reactant, which is the individual radicals. If there is a sufficiently large H, then the individual reactant radicals are prepolarized to a single state so $S_p/k_b|_{\text{reactant}} = 0$. The spin on the cage complex is inherited, so there is only one possible state for the product cage, so the cage complex has $S_p/k_b|_{\text{product(cage)}} = 0$. For the prepolarized radicals (in a field of sufficient H),

$$\frac{\Delta S_p^\ddagger}{k_b} = \frac{S_p}{k_b}\Big|_{\text{product(cage)}} \frac{S_p}{k_b}\Big|_{\text{reactant}} \tag{89}$$

In a sufficiently large H that reactants are prepolarized

$$\frac{\Delta S_p^{\ddagger}}{k_b} = 0 - 0 = 0 \tag{90}$$

The entropy for the radicals not prepolarized is set by the sum of the entropies for the individual reactant species. For the reaction of a singlet with a radical with m unpaired spins, $S_p/k|_{\text{reactant}} = S_p/k|_{\text{reactant,S}} + S_p/k|_{\text{reactant,radical}} = 0 + m \ln 2$ where the radical has m unpaired spins. For the reaction between two radicals, as for $Co\,(bpy)_3^{2/1}$ which is a TQ reaction, where there are m_a unpaired spins on one reactant and m_b unpaired spins on the other reactant,

$$S_p/k_b|_{\text{reactant}} = S_p/k_b|_{\text{reactant,radicala}} + S_p/k_b|_{\text{reactant,radicalb}} \tag{91}$$

$$= m_a \ln 2 + m_b \ln 2 = (m_a + m_b) \ln 2 \tag{92}$$

For the TQ of $Co\,(bpy)_3^{2+/1+}$, the entropy of the reactant is high as $S_p/k_b|_{\text{reactant,TQ}} = (2+3) \ln 2 = 5 \ln 2$. When on reactant is a singlet, the same equation applies but $m_a = 0$. The spin is inherited for the product cage complex, so $S_p/k_b|_{\text{product(cage)}} = 0$. Then for radical not pre-polarized by an applied field,

$$\frac{\Delta S_p^{\ddagger}}{k_b} = \frac{S_p}{k_b}|_{\text{product(cage)}} \frac{S_p}{k_b}|_{\text{reactant}} \tag{93}$$

$$= 0 - (m_a + m_b) \ln 2 = -(m_a + m_b) \ln 2 \tag{94}$$

$$\text{as } H \rightarrow 0 \text{ and reactants are not prepolarized} \tag{95}$$

Thus, in considering difference in the intercepts of the Arrhenius plots for the Nafion (not prepolarized) and C1 (assumed H sufficient for the radicals to be fully prepolarized), then the difference between an Arrhenius intercept for a sufficient

magnetic field and for a Nafion film will be

$$\frac{\Delta S_p^\ddagger}{k_b}\bigg|_{magnetic} - \frac{\Delta S_p^\ddagger}{k_b}\bigg|_{Nafion} = 0 - (-(m_a + m_b)\ln 2) \tag{96}$$

$$= (m_a + m_b)\ln 2 \tag{97}$$

Return now to the Arrhenius derived slope and intercept.

$$b = \ln\left[\frac{2gHS\beta}{h}\right] + \frac{\Delta S_p^\ddagger}{k_b} + \frac{\Delta S^\ddagger}{k_b} \tag{98}$$

$$slope = \frac{\Delta H_0^\ddagger - gHS\beta}{k_b} = \frac{\Delta H_0^\ddagger}{k_b}\left[1 - \frac{gHS\beta}{\Delta H_0^\ddagger/k_b}\right] \tag{99}$$

The term $\Delta S_p^\ddagger$ does not appear in the slope. The Arrhenius slope does provide

access to $\Delta H_0^\ddagger$ and $gSH\beta$. The term $\Delta S_0^\ddagger$ is found in the Arrhenius slope.

4.4.5.2 Time Constant for Magnetic Effects on Chemical Reactions

The frequency for magnetic effects on chemical reactions is now embedded in the

preexponential factor, $gSH\beta/h$. This yields the time constant for magnetic effects,

$\tau_{MagEffect}$.

$$\tau_{MagEffect} = \frac{h}{gSH\beta} \tag{100}$$

For a reaction of one unpaired electron in the earth's magnetic field, $g \sim 2$, $S = 1/2$,

and $H = 1G$. $\tau_{MagEffect} \sim hH/\beta = (1G)\,6.626 \times 10^{-34}\,\mathrm{J\,s}/9.274 \times 10^{-28}\,\mathrm{J\,G}^{-1} = 7.$

$1448 \times 10^{-7} s$ or about 1 μs. The time constant decreases with a stronger field or

more unpaired spins. Also note that this time constant is significantly longer than

$h/k_b T$, which is of the order of 10^{-13} s or 0.1 ps. The time constant for diffusion,

$\tau_{diffusion}$, in solution is approximated as ℓ_{hop}^2/D, where ℓ_{hop} is the distance a species

moves from one solvent well to the next, perhaps ~ 0.3 nm, and D is the diffusion coefficient in the solvent, $\sim 5 \times 10^{-6}$ cm^2/s in water. Then, in water the time constant for diffusion is $\tau_{diffusion} \sim \left(3 \times 10^{-8} \text{ cm}\right)^2 / 5 \times 10^{-6}$ cm^2/s $\sim 1.8 \times 10^{-10}$ s or about 0.2 ns.

4.4.5.2.1 Why Magnetic Effects on Electron Transfer Kinetics Rarely Observed

There are several reasons why magnetic effects on electron transfer kinetics are rarely observed. Most kinetic measurements are made in solvents with diffusion coefficients comparable to water or in the gas phase where diffusion is even faster. The time it takes for molecular species to move short compared to the time needed to implement a magnetic effect. In solution, $\tau_{MagEfffect} \sim 3500\tau_{diffusion}$. When measurements are made in polymers, in near solid state matrices such as batteries, and on adsorbates, transport is markedly slowed or even eliminated. Under those conditions the time constant for diffusion is comparable or longer than $\tau_{MagEffect}$. In domains of slow or no transport, magnetic effects are more likely to be observed.

A second reason magnetic effects on electron transfer reactions and on reactions in general are rarely observed may be that it is easy to overlook effects when, for $gS \sim 1$ and $H = 1G$ for one unpaired electron in the earth's magnetic field, $gSH \sim 1$.

Finally, in our studies, nonuniform magnetic fields established about the micromagnets are always more effective at generating magnetic effects than application of a uniform external field. It is probable that the magnetic field gradient

is important in establishing an effect. It is noted that the model developed here is for an average uniform field. Effects of a field gradient are beyond the scope of the current model.

4.4.6 Some Testing of the Model against the Data

Consider first the data collected for $Ru\,(bpy)_3^{2+/3+}$ for a series of magnetic particles.

4.4.6.1 Data with Magnetic Susceptibility

It is expected that H is proportional to magnetic susceptibility of the particles. Measurements were made with a single redox probe, $Ru\,(bpy)_3^{2+}$ and films of Nafion and Nafion plus one of four different coatings, denoted C1, C3, C8, and C18. The designation is for the number of carbons in the chain of the coating. It was expected that stronger fields would be found with thinner coatings and that was largely true. However, the C8 coating had a lower magnetic susceptibility than C18. In the following, H is taken as proportional to susceptibility. That is, higher measured susceptibility is taken as greater magnetite content by volume and thus a stronger field.

4.4.6.1.2 Equation 85: slope vs H

A plot of Arrhenius slope, *slope* versus H should be linear with form
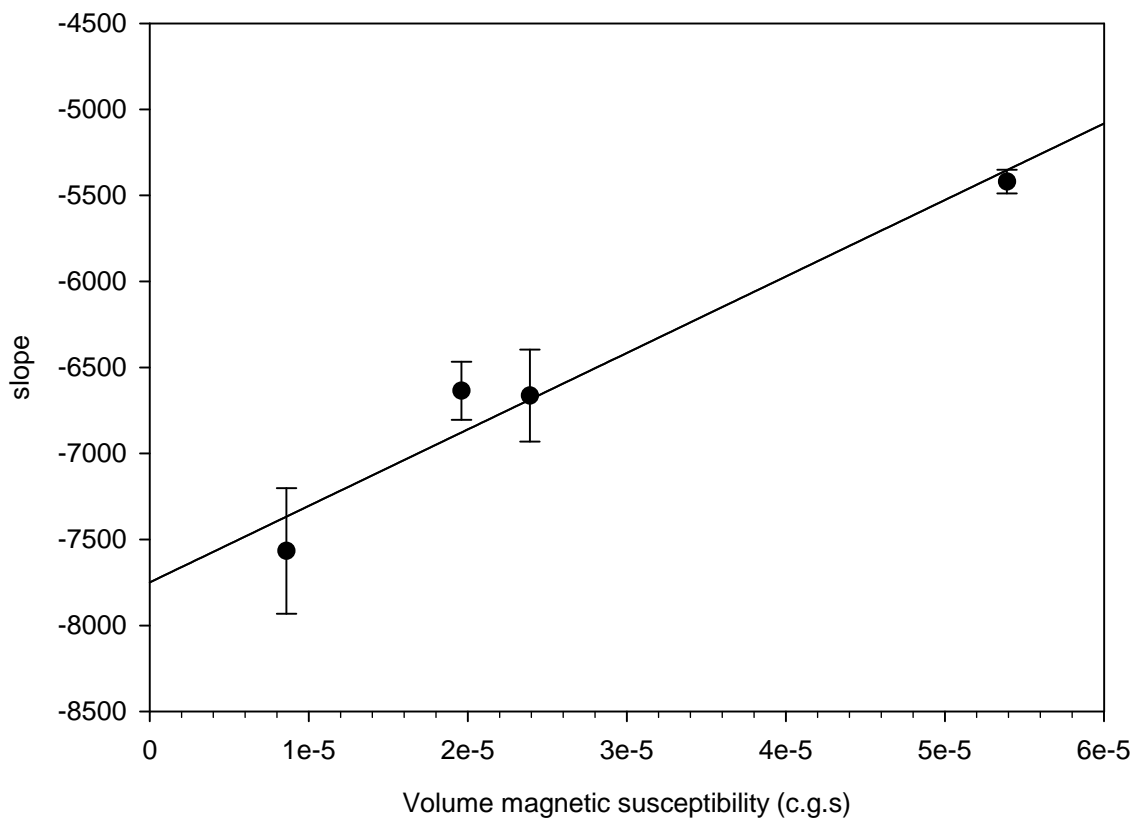
Figure 40. Equation 85: slope vs H.

$slope = slope_{mvsH}H + b_{mvsH}$.

$$slope_{mvsH} = \frac{+gS\beta}{k_b} \tag{101}$$

$$b_{mvsH} = -\frac{\Delta H_0^{\ddagger}}{k_b} \tag{102}$$

Note slope should be negative.

$$slope = + (4.45 \pm 0.68) \times 10^7 \, (mag \; sus) - (7749 \pm 212) \; \text{ with } R^2 = 0.9333 \tag{103}$$

Assessment of the Plot:

1. For a plot of the Arrhenius slope with assessment of magnetic strength, a positive slope is expected, as found.

2. The correlation is acceptable given that this is a plot derived from another plot.

3. If H were plotted, then expect the slope of this plot to be $+gS\beta/k$. For $Ru\,(bpy)_3^3$, $gS = 2.15 \times \frac{1}{2} = 1.075$. The constants $\beta/k = 6.7 \times 10^{-5} K/G$, so the predicted slope would be 7.2×10^{-5} K/G. The slope is substantially higher, but it cannot be interpreted as we do not know the correlation between H and magnetic susceptibility. The discrepancy in the values may reflect the relationship between H and the measured susceptibility.

4. The intercept is expected to be the enthalpy of activation independent of magnetic effects, $-\Delta H_0^{\ddagger}/k$. From the plot, this is -7400 ± 200, which correlates very well with the value of $-\Delta H_0^{\ddagger}/k$ found for the Nafion films of -7050 ± 90.

4.4.6.1.3 Equation 84: b vs H

The equation for the intercept can be rewritten as

$$b = \ln\left[\frac{2gS\beta}{h}\right] + \ln[H] + \frac{\Delta S_p^{\ddagger}}{k_b} + \frac{\Delta S^{\ddagger}}{k_b} \tag{104}$$

A plot of Arrhenius intercept b versus $\ln H$ should be linear with form $slope = slope_{bvsH} H + b_{bvsH}$. Because the relationship between H and susceptibility is not known, it is expected that the slope should be positive. Similarly the intercept will likely have additional, but at this time, unknown terms. The terms should be
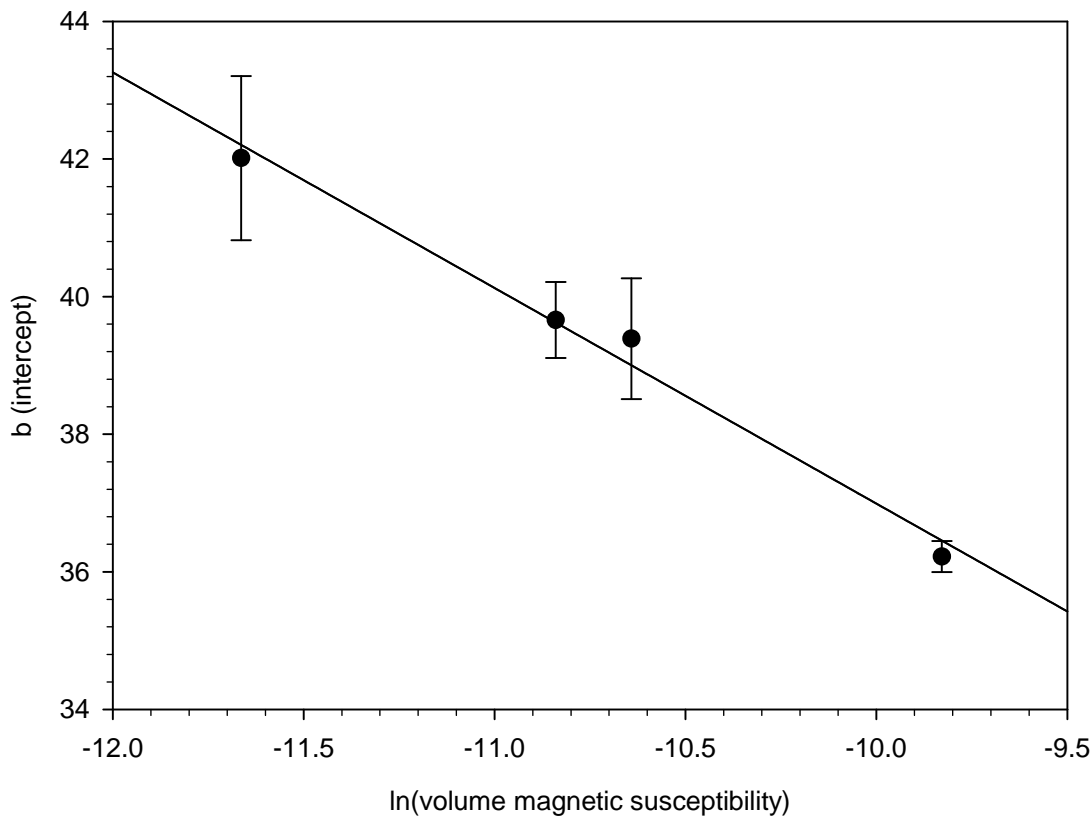
Figure 41. Equation 84: b vs $\ln H$.

the same for all Cn coatings.

$$slope_{bvsH} > 0 \tag{105}$$

$$b_{bvsH} = \ln\left[\frac{2gS\beta}{h}\right] + \frac{\Delta S_p^{\ddagger}}{k_b} + \frac{\Delta S^{\ddagger}}{k_b} + \ldots \tag{106}$$

$$b = -\left(3.13 \pm 0.27\right)\ln\left(mag\ sus\right) - \left(5.65 \pm 2.87\right) \ \text{ with } R^2 = 0.9858 \tag{107}$$

Assessment of the Plot:

1. These plots show strong correlation between b and $\ln\left(mag\ sus\right)$. From the

equation, however, a positive slope is expected which is not what is observed.

The following point must be considered.

(a) The intercept interprets the electron nuclear spin polarization term, so this is not an issue of the reactant energy being misinterpreted. It is conceivable that the assumption of one zero for the sufficient field may be incorrect.

2. Given the derivative nature of the plot, the correlation is good.

3. The slope cannot be interpreted as the magnetic susceptibility relationship to H is not known. However, the negative slope is difficult to understand, unless the field is not large enough.

4. The intercept is complex because there may be other terms within the intercept that are not accounted for by this model. It is interesting to consider the intercept, -5.65 relative to the intercept of the Nafion film, 5.1. In the simplest model, the difference would be $\Delta S_p^{\ddagger}$. That the difference of the determined values are 10.75 would indicate that the simplest case is not operative.

4.4.6.1.4 Equation 85: slope(M) - slope(N) vs H

It is anticipated that the $\Delta H_0^{\ddagger}$ contains no magnetic terms and because it is largely electrostatic, that the value of $\Delta H_0^{\ddagger}$ is the same for all $M\,(bpy)_3^{2+/3+}$ redox couples and is the same in Nafion as in the magnetic composites. It may be slightly different for $Co\,(bpy)_3^{2+/1+}$ because they have different charges. For Nafion, $H \to 0$ so that the Arrhenius slope for Nafion is

$$slope(N) \to \frac{\Delta H_0^{\ddagger}}{k_b} \qquad (108)$$

This enthalpy will include any nonmagnetic effects and assumes the earth's field

is negligible where as the earth's field is $\sim 1G$. Note that $\Delta H_0^{\ddagger}$ would include any events such as spin pairing that may be important to the SQ reaction of the $Co\,(bpy)_3^{2+/3+}$. Allow $slope(M)$ is the slope of the Arrhenius with magnetic microparticles in the film and $slope\,(N)$ be the slope of the Arrhenius plot for the Nafion film. Then, by examining the difference $slope(M) - slope\,(N)$ the magnetic enthalpy term is isolated.

$$slope\,(M) - slope\,(N) = +\frac{gS\beta}{k_b}\,(H_{big} - H) \tag{109}$$

So a plot of $slope\,(M) - slope\,(N)$ versus H should be linear with a slope of and an intercept of $\pm gS\beta H/k$. But this is a tertiary analysis and may be prone a great deal of uncertainty and error propagation.

4.4.6.1.5 $slope_A$ versus gS ($slopeAvgS$) across $M\,(bpy)_3^{n/n+1}$ for C1

From Equation 85 and variation $M\,(bpy)_3^{n/n+1}$ for each separate Nafion and C1 micromagnet composites, a plot of $slope_A$ versus gS is characterized as

$$slope_A = \frac{\beta H}{k_b}gS - \frac{\Delta H_0^{\ddagger}}{k_b} \tag{110}$$

yields

$$slope_{slopeAvgS} \propto \frac{gH}{k_b} \tag{111}$$

$$b_{slopeAvgS} = -\frac{\Delta H_0^{\ddagger}}{k_b} \tag{112}$$

Note the proportionality in $slope_{slopeAvH}$ because only a relative measure of H is available.

The plot is shown for Nafion and C1 magnets. For the radical radical reaction of
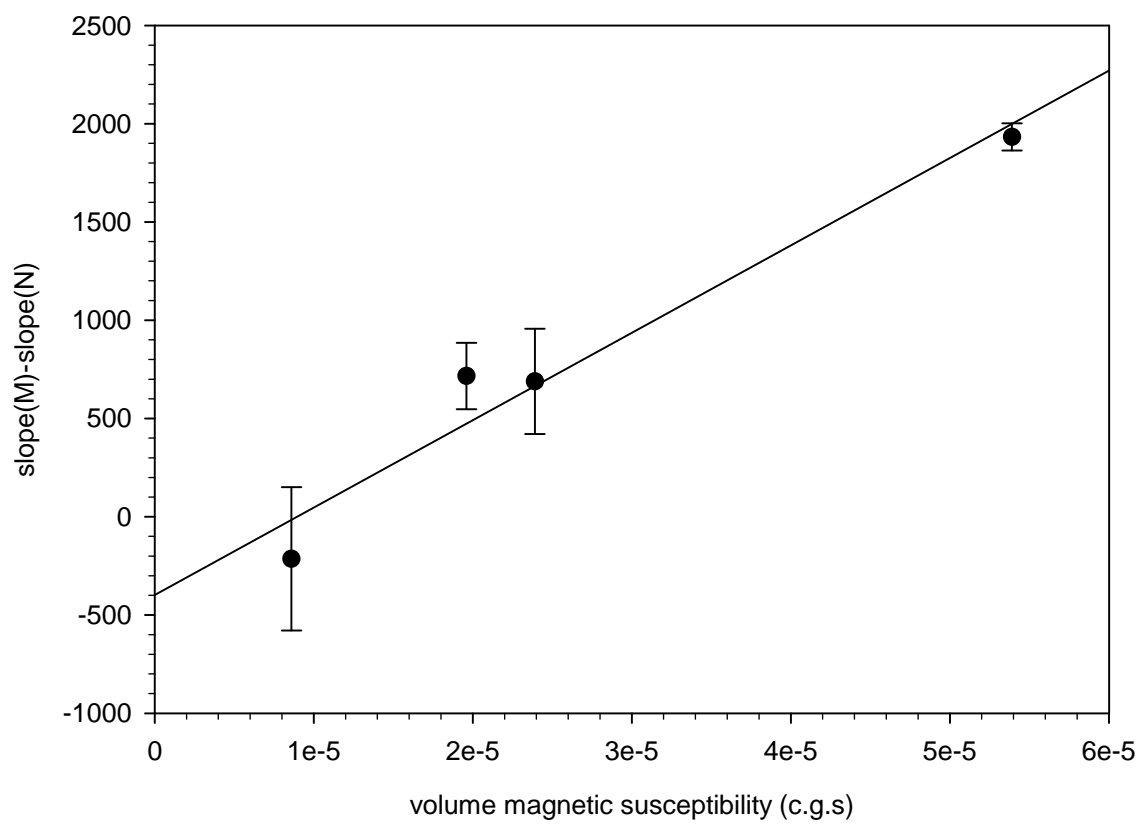
Figure 42. Equation 109: slope(M) - slope(N) vs H.
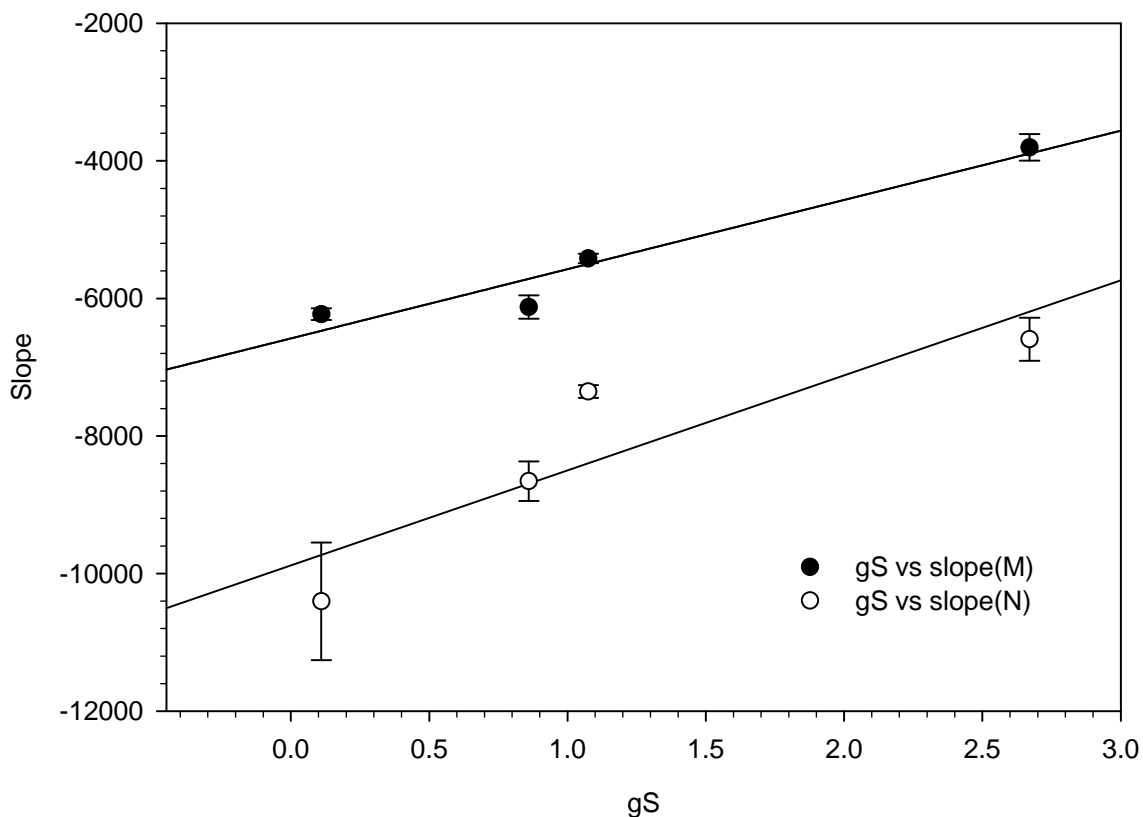
Figure 43. $slope_A$ versus gS for the Nafion films and C1 magnetic composites. $\Delta H_0^{\ddagger}$ may be different for the $\text{Co}(bpy)_3^{2/1}$ couple. The g value for the radical radical reaction is taken as $\Delta g = \left| g_{Co(bpy)_3^2} - g_{Co(bpy)_3^1} \right|$ where the g-value for $Co\,(bpy)_3^1$ is approximated as 2.

$Co\,(bpy)_3^{2/1}$, a QT, the g value is either $g_1 + g_2$ or $|g_1 - g_2|$ where the S value matches the number of unpaired spins, 5/2 or 1/2. Here the difference is shown. So, the g value for the radical radical reaction is taken as $\Delta g = \left| g_{Co(bpy)_3^2} - g_{Co(bpy)_3^1} \right|$ where the g-value for $Co\,(bpy)_3^{1+}$ is approximated as 2 and $S = 1/2$. This gives the best line but the data interpretation is not apparent.

The equation for the line is

$$slope_A (N) = (1380 \pm 490) \, gS - (9880 \pm 740) \text{ with } r^2 = 0.78 \qquad (113)$$

$$slope_A (C1) = (1000 \pm 190) \, gS - (6580 \pm 280) \text{ with } r^2 = 0.93 \qquad (114)$$

Assessment of the Plot:

1. $\Delta H_0^{\ddagger}$ may be different for the $Co\,(bpy)_3^{2+/1+}$ couple than for $M\,(bpy)_3^{2+/3+}$. Removing $Co(bpy)_3^{2+/1+}$ from the plots does not improve the quality of the plots.

2. There is a difference in the concentrations of the probes based on the initial probe: $Co\,(bpy)_3^{3+}$, $Os\,(bpy)_3^{3+}$, and $Ru\,(bpy)_3^{2+}$ for the $M\,(bpy)_3^{2+/3+}$ and $Co\,(bpy)_3^{2+}$ for $Co\,(bpy)_3^{2+/1+}$. This may be reflected in the data. The data as yet are not corrected for the differences in concentration.

3. From the model, it is expected the slopes will be positive, which they are.

4. It is expected that the slopes will be proportional to H so Nafion should have a lower slope than C1 magnets, but that is not observed.

5. The intercepts should reflect $-\Delta H_0^{\ddagger}/k_b$. The plot correlations are poor, so this analysis is suspect but the intercept for the C1 magnetic data is comparable (-7749 K) to $slope_A (C1) = -6580$ K . The intercept for the Nafion analysis is -9880 K. Given the uncertainties, the values are some what similar. Both intercepts are negative as anticipated.

6. Overall, the quality of the fit is poor and the uncertainties of concentration, correct g value for the TQ couple, and the difference in $\Delta H_0^{\ddagger}$, the analysis should
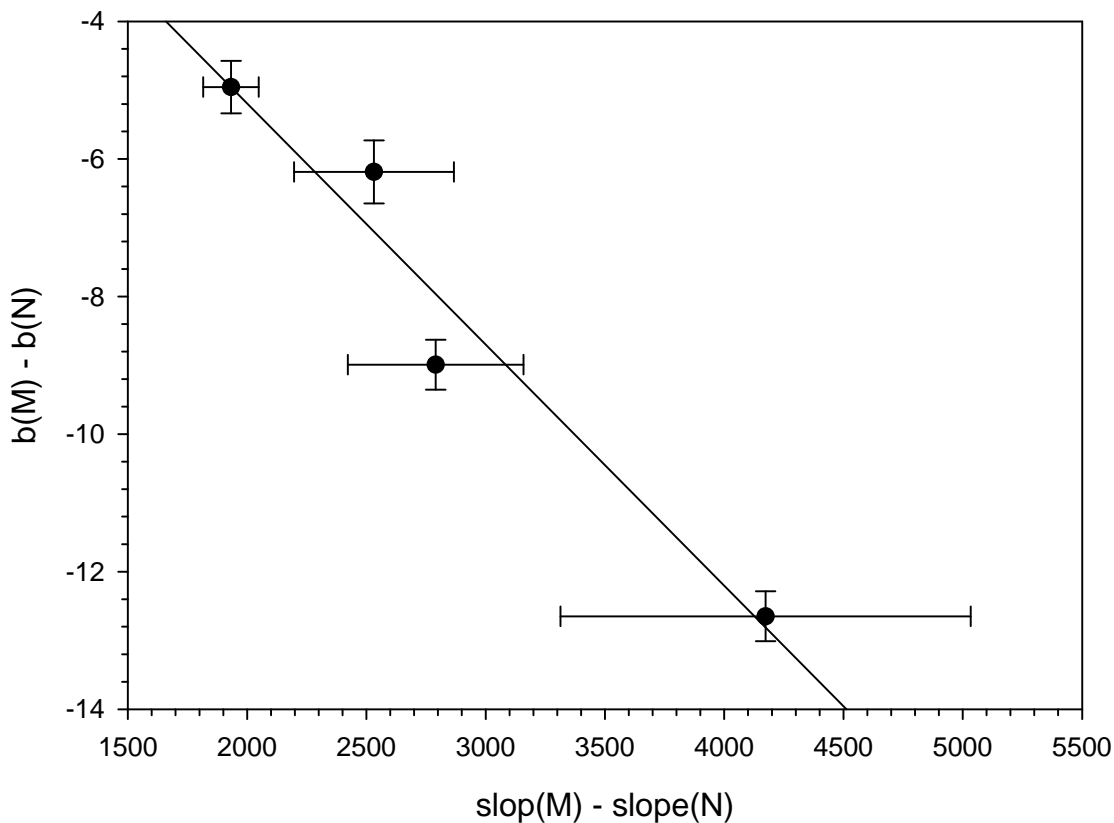
Figure 44. Relationship between b(M) - b(N) vs slope(M) - slope(N).

not be relied on heavily.

It is interesting to note that $b\left(M\right) - b\left(N\right)$ versus $\left[slope\left(M\right) - slope\left(N\right)\right]$ is linear and consistent with a magnetic effect.

4.4.6.1.6 Entropy Analysis for Arrhenius Intercept with H

The studies with various magnetic particles, C1, C3, C8, and C18 and Nafion, but one redox probe, $Ru\left(bpy\right)_3^{2+}$, allow b for the Nafion and the magnetic composites to

be expressed as

$$b\left(N\right) = \ln\left[\frac{2gS\beta}{h}\right] + \ln\left[H\right] + \ln 2 + \frac{\Delta S^{\ddagger}}{k_b} \qquad (115)$$

$$b\left(M\right) = \ln\left[\frac{2gS\beta}{h}\right] + \ln\left[H_{big}\right] + \frac{\Delta S^{\ddagger}}{k_b} \qquad (116)$$

where H_{small} approaches zero and is the earth's field or less. If H is proportional to magnetic suggestibility,

$$b\left(M\right) - b\left(N\right) = \ln\left[\frac{H}{H_{small}}\right] + \ln 2 \qquad (117)$$

So, if all else is equal, $b\left(M\right) - b\left(N\right)$ versus $\ln\left[H\right]$ should be linear and the intercept should be $\ln 2$ as long as $H_{small} = 1$ and the relationship between H and magnetic susceptibility is simply proportional.

4.4.6.1.7 Entropy Analysis for Arrhenius Intercept with gS

For the expressions of $b\left(M\right)$ and $\left(N\right)$ with gS,

$$b\left(N\right) = \ln\left[\frac{2H_{small}\beta}{h}\right] + \ln\left[gS\right] + \left(m_a + m_b\right)\ln 2 + \frac{\Delta S^{\ddagger}}{k} \qquad (118)$$

$$b\left(M\right) = \ln\left[\frac{2H\beta}{h}\right] + \ln\left[gS\right] + \frac{\Delta S^{\ddagger}}{k} \qquad (119)$$

In both cases, the Arrhenius intercepts $b\left(N\right)$ and $b\left(M\right)$ should increase with gS.

If all else remains the same, then

$$b\left(M\right) - b\left(N\right) = \ln\left[\frac{H}{H_{small}}\right] - \left(m_a + m_b\right)\ln 2 \qquad (120)$$

So a plot of $b\left(M\right) - b\left(N\right)$ versus the expected $\left(m_a + m_b\right)$ should be linear with a slope of -ln 2 and an intercept of $\ln\left[H/H_{small}\right]$.
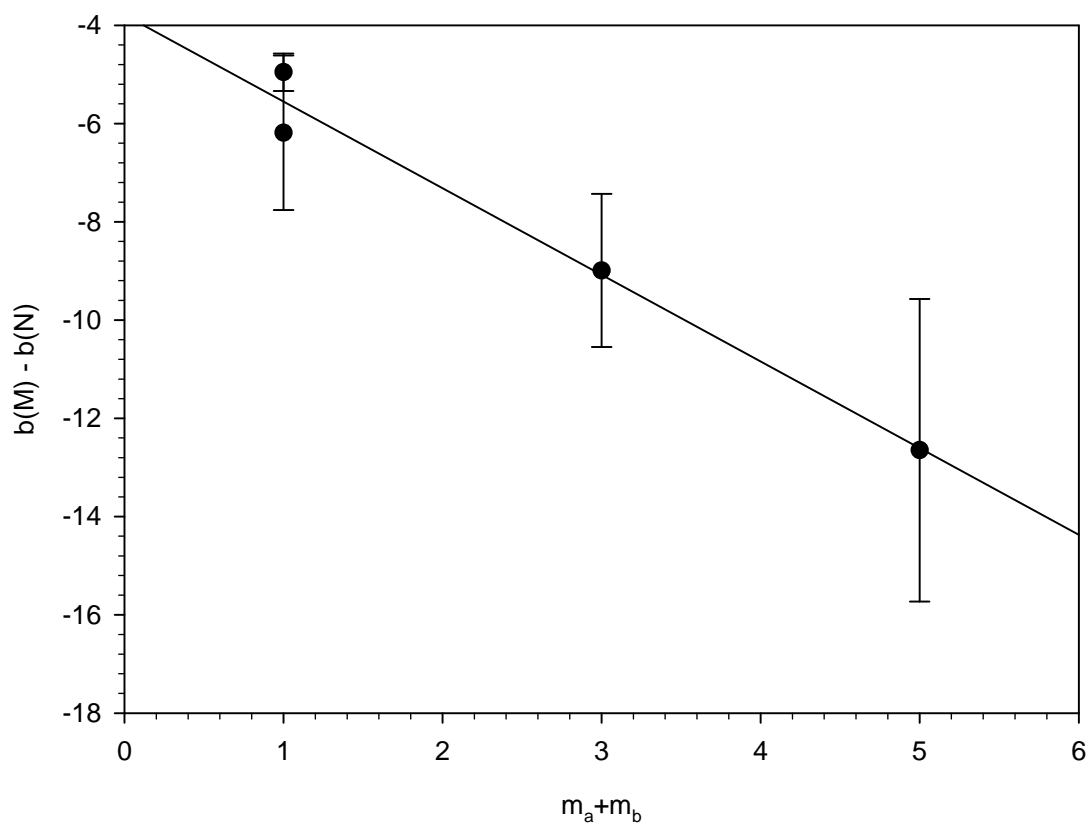
Figure 45. Entropy Analysis for Arrhenius Intercept with gS.

$$b\left(M\right)-b\left(N\right)=-\left(0.554\pm0.059\right)\left(m_a+m_b\right)-\left(2.04\pm0.51\right) \text{ with } R^2=0.9896 \quad (121)$$

Assessment of the Plot:

1. For a plot of difference in the Arrhenius intercepts with m_a+m_b should have a negative slope, as shown.

2. The correlation is acceptable given that this is a plot derived from another plot.

3. The slope is expected to be $-\ln 2 = -0.7$. We have a slope of -0.554 that is close to the expected value.

4. The intercept is expected to be $\ln\left[\frac{H}{H_{small}}\right]$, which suggests the intercept should be positive if $H > H_{small}$. The intercept is negative at -2.4.

4.5   Conclusion

Data have been collected for magnetically modified electrodes for a series of transition metal complexes and for a series of magnetic microparticles with different magnetic properties. Cyclic voltammetric studies as a function of temperature have confirmed that magnetic fields impact the rates of self exchange reactions for the transition metal complexes. The rates of the reactions increase with the magnetic content of the microparticles.

The temperature data were analyzed by Arrhenius plots of log rate against reciprocal temperature. These data were used to test models of magnetic effects on electron transfer rates. Impacts were found in both the slope and intercept data for

the magnetic composites and Nafion films.

The models predict that the enthalpy of activation is largely established by electrostatics and is not subject to magnetic impacts. Magnetic effects on the enthalpy arise from electron nuclear spin polarization and electron spin polarization events. The magnetic effects on the entropy of the reaction arise from the spins on the reactants such that in the absence of an applied field, the spin probabilities establish the magnetically based entropy. When the field is applied, a single state is probable and the spin based entropy becomes negligible. An additional step is included in the mechanism. This is the prepolarization of the reactant spins in the applied field. This reduces the entropy and the activation enthalpy for the reaction.

CHAPTER 5

CONVOLUTION TECHNIQUE FOR THIN FILM ELECTRODES

In the previous chapters, magnetic field effects on heterogeneous electron transfer and self exchange reactions have been examined by coating electrodes with ion exchange polymers and magnetic particle composites. For these modifications, use of an ion exchange polymer is indispensable to create coatings and to provide ionic conductivity. Because the ion exchange polymer coating alters diffusion profiles about the electrode surface, more advanced electrochemical modeling is needed to further the understanding and interpretation of the current-voltage profiles of modified electrodes. The type of films examined here fall in the class of polymer coated electrode generally represented as uniform films because the film is spatially invariant normal to the electrode.

Other examples of surface modifications include catalytic modifications, which is an active research area for energy conversion applications. The modification is to attach catalytic material or metal alloys to noncatalytic electrodes. The objective of catalyst modification is to facilitate a slow electrochemical reaction on an inexpensive electrode such that the reaction occurs at a potential closer to the theoretical redox potential. For analytical applications, electrode modifications improve selectivity and sensitivity to a specific electroactive analyte by selective extraction based on their charge, hydrophilicity, and size.

For most of these electrode surface modifications, the uniform film model is applicable. Development of an analytical tool to characterize uniform films would
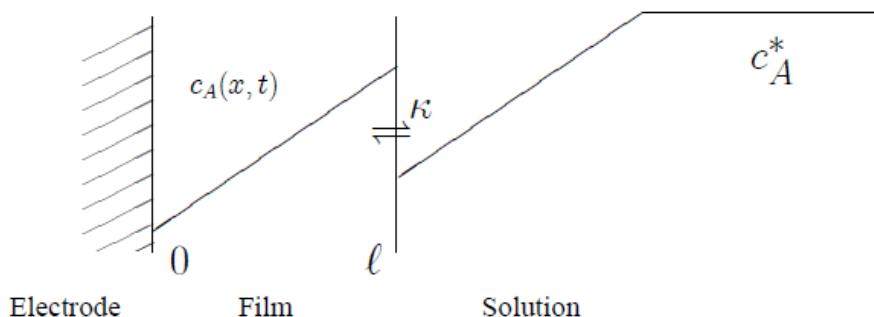
Figure 46. Concentration profile of thin film modified electrode where redox probe present in solution at concentration c_A^* partitions across the film solution interface such that the initial concentration in the film is κc_A^*. At the electrode surface, probe is electrolyzed. The x-axis is the distance from the electrode and the y-axis is the concentration of the redox probe. l is thickness of film and κ is the extraction parameter. Profiles are shown for steady state electrolysis.

facilitate characterization of these systems. In this chapter, a newly developed convolution technique for the uniform film is introduced and discussed.

5.1 Theoretical Background

Nafion is commonly used for various types of electrode modifications. Assessment of the uniform film properties is critical to good system analysis. Nafion is well represented as an uniform film on the electrode surface. The chemical structure is shown in Figure 1.

When an electrode coated with an uniform film is placed in electrolyte solution that contains a redox probe, the probe extracts across the film solution interface and equilibrates in the film. Under electrochemical perturbation, diffusion profiles for the probe are established in the film and the solution. The two diffusion profiles interact with each other at the interface as described by an extraction parameter (κ). A schematic description of the system is shown in Figure 46.

The characteristics of electrochemical current responses to any voltammetric perturbation are defined by a combination of models for charge transfer kinetic and mass transport. Fick's laws of diffusion are appropriate for uniform films. For unmodified, planar electrodes, current voltage profiles for the redox probe in a semi-infinite linear diffusion system was solved implicitly by Nicholson and Shain [53]. The current-voltage profile for a redox probe in a uniform film on an electrode was modeled and simulated explicitly by Hettige and Leddy [58]. The simulation for cyclic voltammetry at a uniform film on an electrode uses an explicit finite difference method and Butler-Volmer electron transfer kinetics.

Convolution techniques, also known as semi-integral methods, are one of the electrochemical data analysis techniques introduced in the early 1970's by Oldham and Savéant [59,60]. The major advantage of this technique is to convert transient currents to simpler, more steady state-like responses that are easier to analyze and to extract parameters [61]. Convolution methods can discriminate against nonfaradaic capacitance and uncompensated resistance and allows rapid determination of reaction kinetics [37].

5.1.1 Derivation of the Convolution Responses

Figure 47 shows that a typical current-voltage profile from cyclic voltammetry at an unmodified, large planar electrode. The characteristic avian shape of the cyclic voltammogram (CV) is converted by convolution to a sigmoidal morphology more characteristic of steady state voltammetry.

Derivations of the response for semi-infinite linear diffusion to a planar electrode
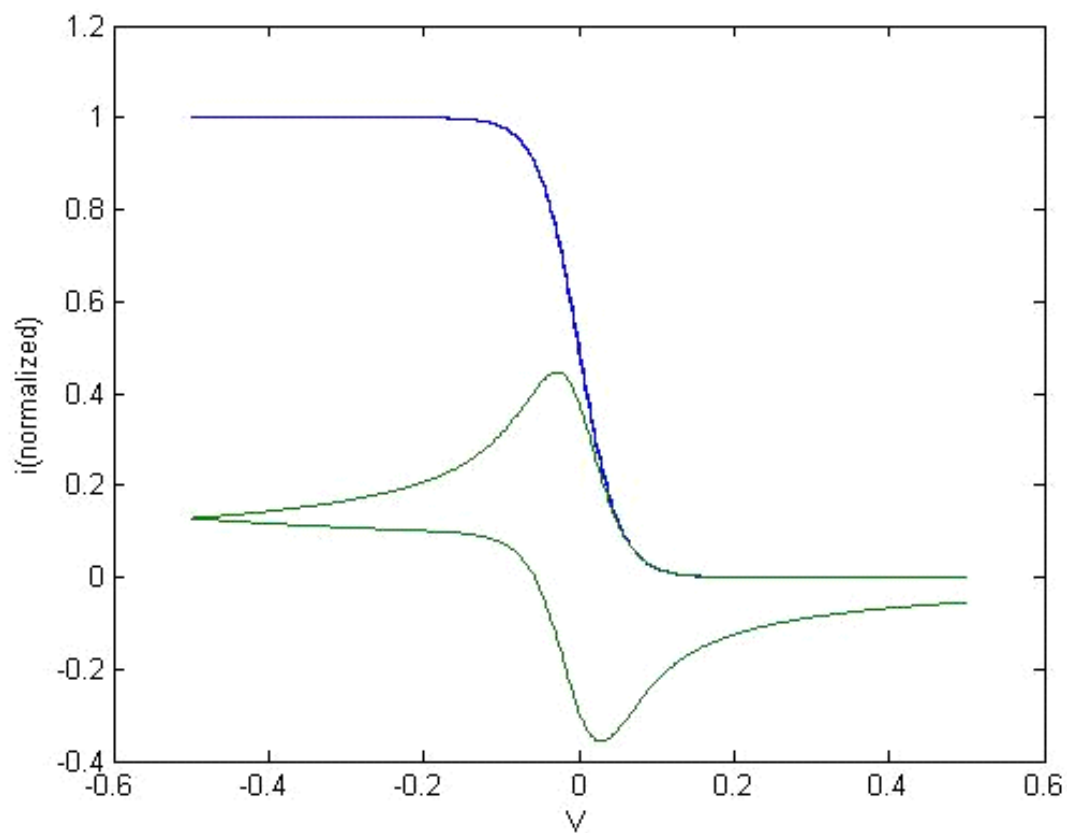
Figure 47. Cyclic voltammogram (green) and its convoluted current-voltage plot (blue) for semi-inifinite linear diffusion at an unmodified electrode. The y-axis is the dimensionless current and the dimensionless convoluted current. The x-axis is potential. The CV is generated by computer simulation and convoluted computationally.

were originally provided by Oldham [59, 62] and Savéant [63]. The derivations serve

as a template for the derivations for an electrode modified with a uniform film and

the redox probe partitions from solution into the film. Derivation of the convolution

equation for an unmodified, planar electrode is as follows. The resulting convolution

equation, Equation 140 (page 133), is used to generate the response shown in Figure

47.

The current expression for a planar, unmodified electrode in one dimension is

$$\frac{i(t)}{nFA} = D\frac{\partial C(0, t)}{\partial x} \qquad (122)$$

where $i(t)$ is the current (A); $C(x, t)$ is the space and time dependent concentration

of the probe (mol/cm^3); x is the coordinate normal to the electrode; D is the

diffusion coefficient of the probe (cm^2/s); n is the number of electrons transferred in

the electron transfer reaction; F is the Faraday constant; and A is the electrode area

(cm^2). The Laplace transform of the current expression is

$$\frac{\overline{i(s)}}{nFA} = D\frac{\partial \overline{C(0, s)}}{\partial x} \qquad (123)$$

Fick's second law for the concentration gradients and diffusion is

$$\frac{\partial C(x, t)}{\partial t} = D\frac{\partial^2 C(x, t)}{\partial x^2} \qquad (124)$$

The Laplace transform of this equation is

$$s\overline{C(x, s)} - C(x, 0) = D\frac{\partial^2 \overline{C(x, s)}}{\partial x^2} \qquad (125)$$

$C(x, 0)$ is the initial concentration of the probe for all x. Solution of this first order

differential equation is

$$\overline{C(x,s)} = \frac{C(x,0)}{s} + A \exp\left[-\sqrt{\frac{s}{D}}x\right] + B \exp\left[\sqrt{\frac{s}{D}}x\right] \tag{126}$$

Because the initial condition is specified as a fixed concentration in solution, C^*,

$$C(x,0) = C^* \tag{127}$$

and the semi-infinite boundary condition in t and convolution s coordinates is

$$\lim_{x \to \infty} C(x,t) = C^* \tag{128}$$

$$\lim_{x \to \infty} \overline{C}(x,t) = \frac{C^*}{s} \tag{129}$$

$B = 0$. The equation becomes

$$\overline{C(x,s)} = \frac{C^*}{s} + A \exp\left[-\sqrt{\frac{s}{D}}x\right] \tag{130}$$

Differentiation of the equation yields

$$\frac{\partial \overline{C(x,s)}}{\partial x} = -\sqrt{\frac{s}{D}} A \exp\left[-\sqrt{\frac{s}{D}}x\right] \tag{131}$$

From Equation 130, the coefficient A is evaluated.

$$\frac{\overline{i(s)}}{nFA} = -A\sqrt{\frac{s}{D}} \tag{132}$$

$$A = -\frac{\overline{i(s)}}{nFA\sqrt{sD}} \tag{133}$$

Equation 130 becomes

$$\overline{C(x,s)} = \frac{C^*}{s} - \frac{\overline{i(s)}}{nFA\sqrt{sD}} \exp\left[-\sqrt{\frac{s}{D}}x\right] \tag{134}$$

We are interested in the concentration at the electrode surface, $\overline{C(0,s)}$, where $x = 0$.

$$\overline{C(0,s)} = \frac{C^*}{s} - \frac{\overline{i(s)}}{nFA\sqrt{sD}} \tag{135}$$

$$= \frac{C^*}{s} - \left(\frac{1}{nFA\sqrt{D}}\right)\overline{i(s)}\left(\frac{1}{\sqrt{s}}\right) \tag{136}$$

The convolution is recognized upon substitution as

$$f(s) = \frac{1}{\sqrt{s}}$$

$$g(s) = \overline{i(s)}$$

The generic convolution or semi-integral, Equation 138, allows the inverse of the expression in Laplace transform coordinates, s, to time coordinates t as

$$L^{-1}[f(s)g(s)] = F(t)^*G(t) \tag{137}$$

$$= \int_0^t F(t-\tau)G(\tau)d\tau \tag{138}$$

The inverse of Equation 136 is obtained by application of Equation 138. The concentration at the electrode surface is expressed by the convolution equation.

$$C(0,t) = C^* - \frac{1}{nFAD^{1/2}}\left[\frac{1}{\pi^{1/2}}\int_0^t \frac{i(u)}{(t-u)^{1/2}}du\right] \tag{139}$$

The response to any voltammetric perturbation that starts at zero current can be used to characterize the concentration at the electrode surface through Equation 139 as long as the electrode is planar and the diffusion profile only probes one phase at the electrode surface. The convoluted current, $I(t)$, is defined by Laplace transform.

$$I(t) = \frac{1}{\pi^{1/2}}\int_0^t \frac{i(u)}{(t-u)^{1/2}}du \tag{140}$$

5.2   Mathematical Development of the Convolution
        Equations

For the uniform film on an electrode, the model characterizes two domains. The domain immediately at the planar electrode is the film, which is in contact with the semi-infinite electrolyte layer. The probe is present in both domains and establishes a concentration in the two domains that is characterized by an extraction parameter, κ. Each domain, the film and solution has a diffusion coefficient, D_f and D_s, respectively. A schematic diagram of the system is shown in Figure 46.

Fick's second law for this system is specified for each domain. The film of thickness l is established at the electrode surface from $x = 0$ to $x = l$. The electrolyte is present for $x > l$. The concentrations in the film and solution are space and time dependent as $C_f(x, t)$ and $C_s(x, t)$.

$$\frac{\partial C_f(x,t)}{\partial t} = D_f \frac{\partial^2 C_f(x,t)}{\partial x^2} \qquad 0 \leq x \leq l \tag{141}$$

$$\frac{\partial C_s(x,t)}{\partial t} = D_s \frac{\partial^2 C_s(x,t)}{\partial x^2} \qquad l < x \tag{142}$$

Laplace transform of these two partial differential equations with respect to time yields

$$\overline{C_f(x,s)} = \kappa \frac{C^*}{s} + A \exp\left(-\sqrt{\frac{s}{D_f}} x\right) + B \exp\left(\sqrt{\frac{s}{D_f}} x\right) \qquad 0 \leq x \leq l \tag{143}$$

$$\overline{C_s(x,s)} = \frac{C^*}{s} + G \exp\left(-\sqrt{\frac{s}{D_s}} x\right) \qquad l < x \tag{144}$$

The semi-infinite boundary condition for the solution phase eliminates the term $\exp\left[\sqrt{s/D_s} x\right]$ because the term will grow without bound as x increases. The initial

concentrations in the film and solution are also incorporated into the equations.

$$C_f(x,0) = \kappa C^* \qquad 0 \le x \le l \tag{145}$$

$$C_s(x,0) = C^* \qquad l < x \tag{146}$$

Boundary conditions for the junction between the film and solution, where $x = l$, are

$$C(l^-,t) = \kappa C(l^+,t) \tag{147}$$

$$D_f \frac{\partial C(l^-,t)}{\partial x} = D_s \frac{\partial C(l^+,t)}{\partial x} \tag{148}$$

The positions l^- and l^+ are the positions just inside the film and just outside the film at the film solution interface. Equation 148 indicates the flux of probe into the film must equal the flux of probe out of the solution; no material is lost. Laplace transform of Equations 147 and 148 yields

$$\overline{C(l^-,s)} = \kappa \overline{C(l^+,t)} \tag{149}$$

$$D_f \frac{\partial \overline{C(l^-,s)}}{\partial x} = D_s \frac{\partial \overline{C(l^+,s)}}{\partial x} \tag{150}$$

Equations 143 and 144 are combined in these two expressions to yield

$$A \exp\left(-\sqrt{\frac{s}{D_f}}l\right) + B \exp\left(\sqrt{\frac{s}{D_f}}l\right) = \kappa G \exp\left(-\sqrt{\frac{s}{D_s}}l\right) \tag{151}$$

The first derivatives of Equations 143 and 144 yield

$$\frac{\partial \overline{C_f(x,s)}}{\partial x} = \left[\begin{array}{c} -\sqrt{\frac{s}{D_f}} A \exp\left(-\sqrt{\frac{s}{D_f}}x\right) \\ +\sqrt{\frac{s}{D_f}} B \exp\left(\sqrt{\frac{s}{D_f}}x\right) \end{array} \right] \qquad 0 \le x \le l \tag{152}$$

$$\frac{\partial \overline{C_s(x,s)}}{\partial x} = -\sqrt{\frac{s}{D_s}} G \exp\left(-\sqrt{\frac{s}{D_s}}x\right) \qquad l < x \tag{153}$$

Substitution into the constraint on flux at the interface, Equation 150 yields

$$\sqrt{\frac{s}{D_f}}\left[\begin{array}{c} -A\exp\left(-\sqrt{\frac{s}{D_f}}l\right) \\ +B\exp\left(\sqrt{\frac{s}{D_f}}l\right) \end{array}\right] = -\sqrt{\frac{s}{D_s}}G\exp\left(-\sqrt{\frac{s}{D_s}}l\right) \qquad (154)$$

$$\sqrt{\frac{D_s}{D_f}}\left[\begin{array}{c} A\exp\left(-\sqrt{\frac{s}{D_f}}l\right) \\ -\sqrt{D_s}B\exp\left(\sqrt{\frac{s}{D_f}}l\right) \end{array}\right] = G\exp\left(-\sqrt{\frac{s}{D_s}}l\right) \qquad (155)$$

Let γ is ratio of diffusion coefficients expressed as $\gamma = \sqrt{D_f/D_s}$. Allow the following notation.

$$\gamma = \sqrt{\frac{D_f}{D_s}} \qquad (156)$$

$$A' = A\exp\left(-\sqrt{\frac{s}{D_f}}l\right) \qquad (157)$$

$$B' = B\exp\left(\sqrt{\frac{s}{D_f}}l\right) \qquad (158)$$

$$G' = G\exp\left(-\sqrt{\frac{s}{D_s}}l\right) \qquad (159)$$

Equations 151 and 155 become

$$A' + B' = \kappa G' \qquad (160)$$

$$\gamma(A' - B') = G' \qquad (161)$$

Equation 160 and 161 are combined to eliminate G'.

$$A' + B' = \kappa\gamma(A' - B') \qquad (162)$$

$$A'(1 - \kappa\gamma) = -B'(1 + \kappa\gamma) \qquad (163)$$

Expanding the equations yields

$$A \exp\left(-\sqrt{\frac{s}{D_f}}l\right)(1 - \kappa\gamma) = -B \exp\left(\sqrt{\frac{s}{D_f}}l\right)(1 + \kappa\gamma) \tag{164}$$

$$B = -A \exp\left(-\sqrt{\frac{s}{D_f}}2l\right)\frac{(1 - \kappa\gamma)}{(1 + \kappa\gamma)} \tag{165}$$

$$\omega = \frac{1 - \kappa\gamma}{1 + \kappa\gamma} \tag{166}$$

then

$$B = -A \exp\left(-\sqrt{\frac{s}{D_f}}2l\right)\omega \tag{167}$$

Equation 123 can be applied to Equation 143 when $x = 0$, which is at the electrode

surface

$$\overline{\frac{i(s)}{nFA}} = D_f\frac{\partial}{\partial x}\left[\kappa\frac{C^*}{s} + A \exp\left(-\sqrt{\frac{s}{D_f}}x\right) + B \exp\left(\sqrt{\frac{s}{D_f}}x\right)\right]_{x=0} \tag{168}$$

$$= D_f\left(-\sqrt{\frac{s}{D_f}}A + \sqrt{\frac{s}{D_f}}B\right) \tag{169}$$

$$= -\sqrt{sD_f}\,(A - B) \tag{170}$$

The current expression for the Laplace transform is

$$\frac{\overline{i(s)}}{nFA\sqrt{sD_f}} = -A + B \tag{171}$$

Because B is determined by Equation 167, A can be determined.

$$\frac{\overline{i(s)}}{nFA\sqrt{sD_f}} = -A - A\omega \exp\left(-\sqrt{\frac{s}{D_f}}2l\right) \tag{172}$$

$$\frac{\overline{i(s)}}{nFA\sqrt{sD_f}} = A\left[-1 - \omega \exp\left(-\sqrt{\frac{s}{D_f}}2l\right)\right] \tag{173}$$

$$A = -\frac{\overline{i(s)}}{nFA\sqrt{sD_f}\left[1 + \omega \exp\left(-\sqrt{\frac{s}{D_f}}2l\right)\right]} \tag{174}$$

We are interested in $\overline{C_f(0,s)}$.

$$
\begin{aligned}
\overline{C_f(0,s)} &= \kappa\frac{C^*}{s} + A + B \tag{175}\\[2mm]
&= \kappa\frac{C^*}{s} + A - A\omega\exp\left(-\sqrt{\frac{s}{D_f}}2l\right) \tag{176}\\[2mm]
&= \kappa\frac{C^*}{s} + A\left[1 - \omega\exp\left(-\sqrt{\frac{s}{D_f}}2l\right)\right] \tag{177}\\[2mm]
&= \kappa\frac{C^*}{s} - \frac{\overline{i(s)}}{nFA\sqrt{sD_f}}\frac{\left[1 - \omega\exp\left(-\sqrt{\frac{s}{D_f}}2l\right)\right]}{\left[1 + \omega\exp\left(-\sqrt{\frac{s}{D_f}}2l\right)\right]} \tag{178}
\end{aligned}
$$

From the series expansion,

$$
\frac{1}{1+a} = \sum_{j=0}^{\infty}(-1)^j a^j \tag{179}
$$

Equation 178 is expanded to

$$\overline{C_f(0,s)} = \kappa \frac{C^*}{s} \tag{180}$$

$$-\frac{\overline{i(s)}}{nFA\sqrt{sD_f}} \left[\begin{array}{c} 1- \\ \omega \exp\left(-\sqrt{\frac{s}{D_f}}2l\right) \end{array} \right] \tag{181}$$

$$\times \sum_{j=0}^{\infty} (-1)^j \omega^j \exp\left(-2j\sqrt{\frac{s}{D_f}}l\right) \tag{182}$$

$$= \kappa \frac{C^*}{s} \tag{183}$$

$$-\frac{\overline{i(s)}}{nFA\sqrt{sD_f}} \left\{ \begin{array}{c} \sum_{j=0}^{\infty} (-1)^j \omega^j \exp\left(-2j\sqrt{\frac{s}{D_f}}l\right) - \\ \exp\left(-\sqrt{\frac{s}{D_f}}2l\right) \omega \sum_{j=0}^{\infty} \\ \times (-1)^j \omega^j \exp\left(-2j\sqrt{\frac{s}{D_f}}l\right) \end{array} \right\} \tag{184}$$

$$= \kappa \frac{C^*}{s} - \frac{\overline{i(s)}}{nFA\sqrt{sD_f}} \left\{ \begin{array}{c} \sum_{j=0}^{\infty} (-1)^j \omega^j \exp\left(-2j\sqrt{\frac{s}{D_f}}l\right) - \\ \sum_{j=0}^{\infty} (-1)^j \omega^{j+1} \exp\left(-2(j+1)\sqrt{\frac{s}{D_f}}l\right) \end{array} \right\} \tag{185}$$

$$= \kappa \frac{C^*}{s} - \frac{\overline{i(s)}}{nFA\sqrt{sD_f}} \left\{ \begin{array}{c} 1 + \sum_{j=1}^{\infty} (-1)^j \omega^j \exp\left(-2j\sqrt{\frac{s}{D_f}}l\right) + \\ \sum_{j=1}^{\infty} (-1)^j \omega^j \exp\left(-2j\sqrt{\frac{s}{D_f}}l\right) \end{array} \right\} \tag{186}$$

$$= \kappa \frac{C^*}{s} - \frac{\overline{i(s)}}{nFA\sqrt{sD_f}} \tag{187}$$

$$-2\frac{\overline{i(s)}}{nFA\sqrt{sD_f}} \sum_{j=1}^{\infty} (-1)^j \omega^j \exp\left(-2j\sqrt{\frac{s}{D_f}}l\right) \tag{188}$$

The second term of Equation 187 is the transformed current expression for unmodified, planar electrode, Equation 136.

$$\frac{1}{nFA\sqrt{D_f}} \overline{i(s)} \frac{1}{\sqrt{s}} = \frac{1}{nFA\sqrt{D_f}} \int_o^t \frac{i(u)}{\sqrt{\pi}\sqrt{t-u}} du \tag{189}$$

The third term is the newly added term for the uniform film modified electrode and

is converted to real space using Equation 138.

$$\frac{2}{nFA\sqrt{D_f}}\overline{i(s)}\sqrt{\frac{1}{s}}\sum_{j=1}^{\infty}(-1)^j\omega^j\exp\left(-\sqrt{\frac{s}{D_f}}2lj\right) \tag{190}$$

$$= \frac{2}{nFA\sqrt{D_f}}\int_0^t\frac{i(u)}{\sqrt{\pi(t-u)}}\sum_{j=1}^{\infty}(-\omega)^j\exp\left(\frac{-l^2j^2}{D_f(t-u)}\right)du \tag{191}$$

The result is

$$C(0,t) = \kappa C^* - \frac{1}{nFA\sqrt{D_f\pi}}\int_0^t\frac{i(u)}{\sqrt{t-u}}du$$

$$-\frac{2}{nFA\sqrt{D_f\pi}}\int_0^t\frac{i(u)}{\sqrt{t-u}}\sum_{j=1}^{\infty}(-\omega)^j\exp\left(\frac{-b^2j^2}{(t-u)}\right)du \tag{192}$$

where

$$b = \sqrt{\frac{l^2}{D_f}} \tag{193}$$

Equation 192 has two important parameters that describe properties of uniform film; b and ω. b is the film thickness relative to the diffusion coefficient and ω is flux parameter for a film in contact with a solution. When b is converted to a dimensionless parameter,

$$b' = \sqrt{\frac{\ell^2}{D_f}nf\upsilon}$$

It approximates the diffusion length relative to the film thickness. n is number of electron, $f = F/RT$ (C/J = V^{-1}), and υ is scan rate (V/s). As b' decreases as for slowed scan rate, the diffusion profile exceeds the film thickness.

ω is the flux parameter for a film in contact with a solution. For flux in the film higher than in solution ($\kappa/\gamma > 1$), $-1 \leq \omega < 0$; for flux in the film less than in solution, ($\kappa/\gamma < 1$), $0 > \omega \geq 1$. For $\omega = 0$, flux in the film and solution are equal. Note that even if $D_f < D_s$, the usual case, κ/γ can be greater than 1 if κ is sufficiently large and ω will be negative.

5.3   Results

The derived equation, Equation 192 is coded in Matlab. The code is in Appendix B. Cyclic voltammetric data are generated by Hettige's program for cyclic voltammetry (CV) for uniform films [58]. Figure 48 shows that computer simulated cyclic voltammogram when $\omega = 0.999$ and $b = 1.2$ (solid) and its convoluted current with convolution for semi-infinite linear diffusion (dashed). As expected, convolution for the unmodified planar electrode does not exhibit a sigmoidal response. However, when the CV is convoluted according to Equation 192, the expected sigmoidal response results (blue dotted).

Figure 49 shows the computer simulated cyclic voltammogram when $\omega = 0.999$ and $b = 3.5$ (solid) and its convoluted graph with the semi-infinite convolution (dashed). This is the case where the flux in the film is low compared to flux in solution, $\kappa/\gamma << 1$. As expected, the semi-infinite convolution for planar electrode does not exhibit a sigmoidal response. However, the same CV is convoluted using the uniform film convolution yields the expected sigmoidal, the typical sigmoidal response is shown (dotted line).

Figure 50 shows the computer simulated cyclic voltammogram for $\omega = -0.8$ and $b = 2.5$ (solid) and its convoluted by the semi-infinite algorithm (dashed). In this case, flux in the film is high compared to flux in solution, consistent with the Gaussian CV, and $\kappa/\gamma > 1$. As expected, the semi-infinite algorithm does not yield a sigmoidal response. However, the same CV convoluted by the uniform film algorithm, yields a sigmoidal response (dotted).

Figure 48. Computer simulated cyclic voltammogram when $\omega = 0.999$ and $b = 1.2$ (solid) and its convoluted current with the semi-inifinite equation technique (dashed). The convolution for the uniform film equation yields the sigmoidal response shown with the dotted lines.
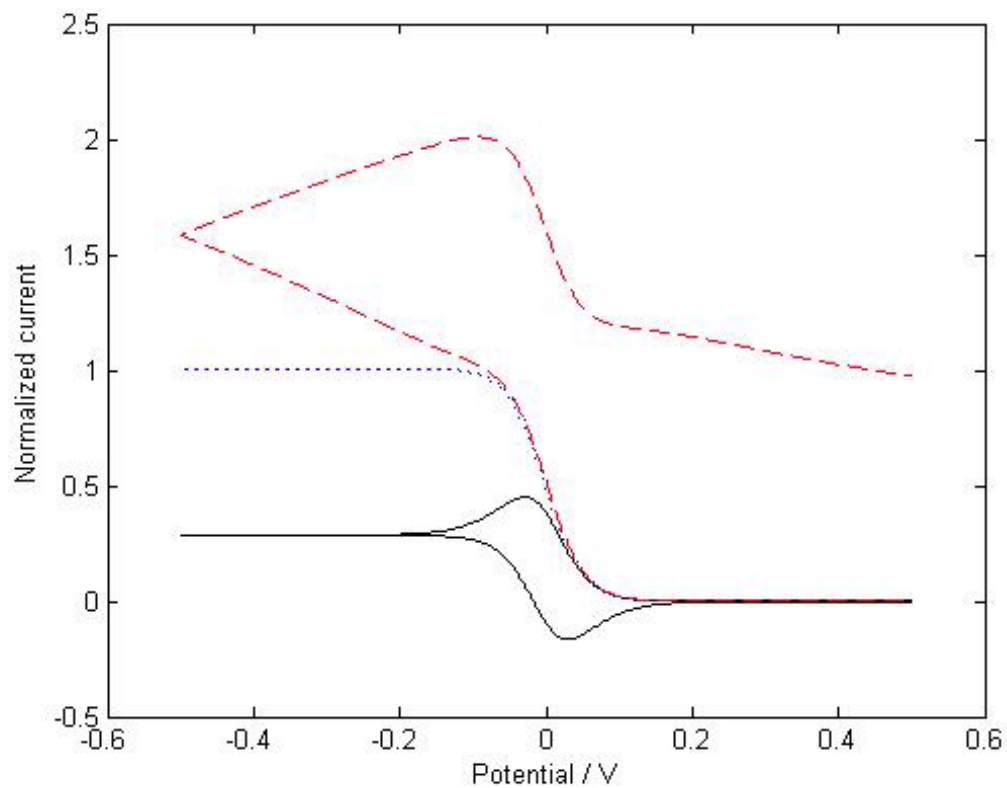
Figure 49. Computer simulated cyclic voltammogram when $\omega = 0.999$ and $b' = 3.5$ (solid) and its convolution by the semi-infinite convolution expression (dashed) and with uniform film convolution (dotted). The uniform film convolution plot shows clear sigmoidal response whereas the semi-infinite convolution does not.
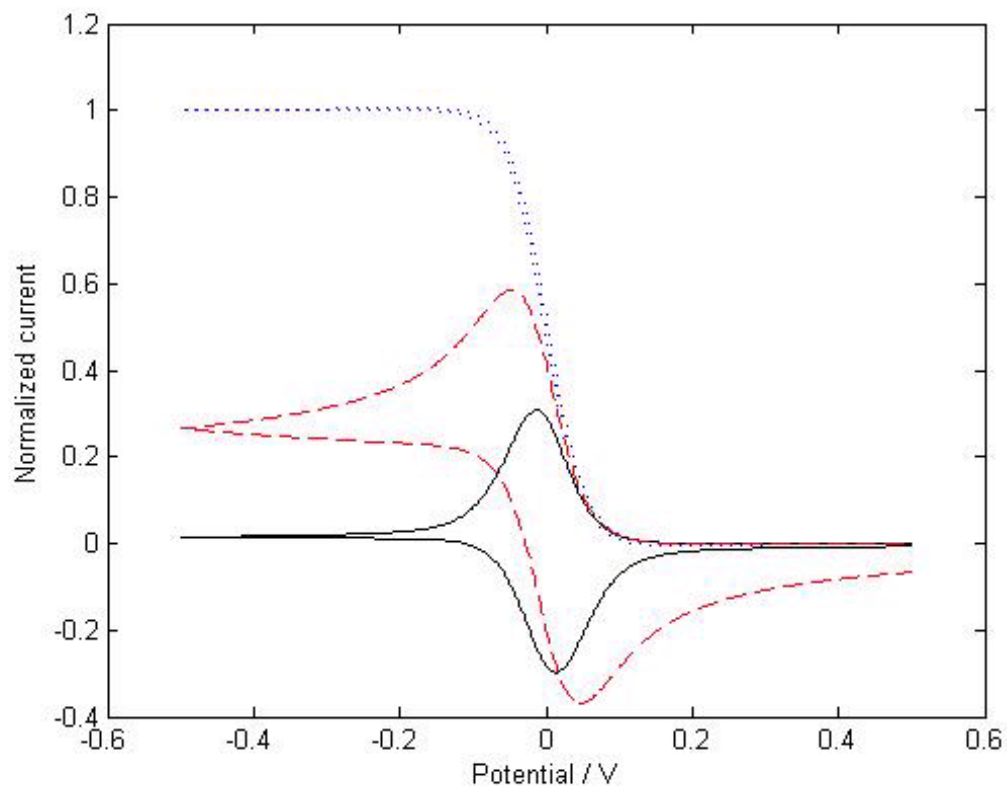
Figure 50. Computer simulated cyclic voltammogram when $\omega = -0.8$ and $b' = 2.5$ (black solid) and its convolution by the semi-infinite algorithm (blue dashed) and the uniform film convolution (dotted red) are shown. The uniform film convolution plot shows a clear sigmoidal response.
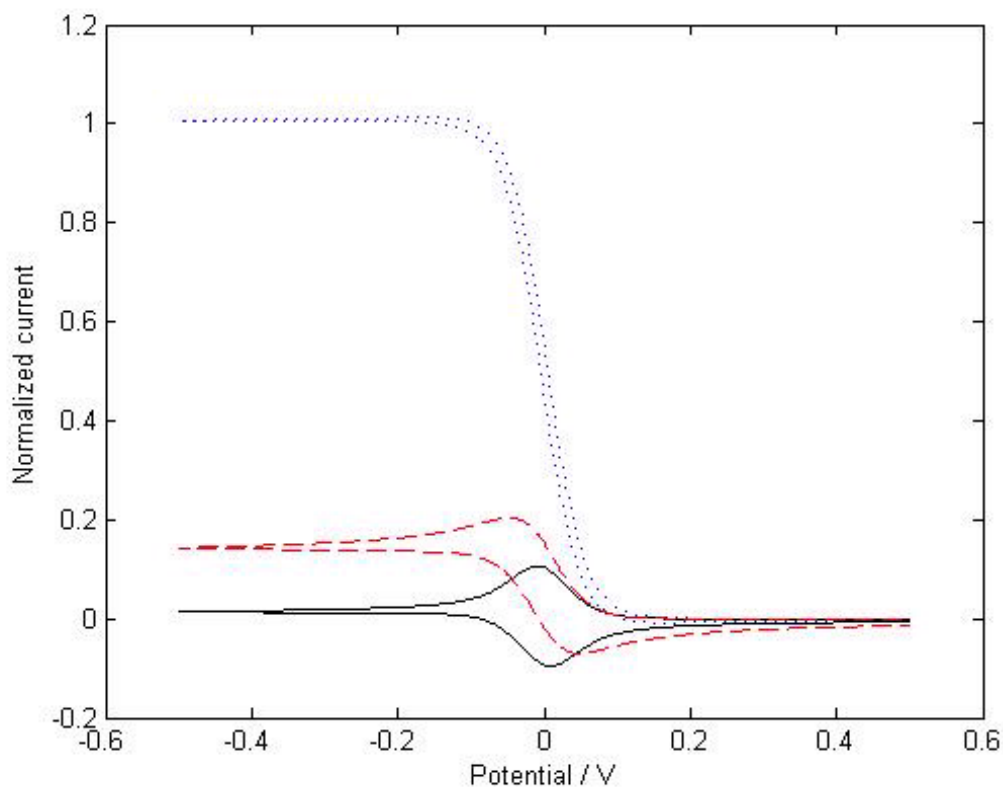
Figure 51. Computer simulated cyclic voltammogram when $\omega = -0.8$ and $b' = 0.25$ (black solid) and its convolution plot by semi-infinite (blue dashed) and uniform film (dotted red) convolution . The uniform film convolution plot shows clear sigmoidal response.

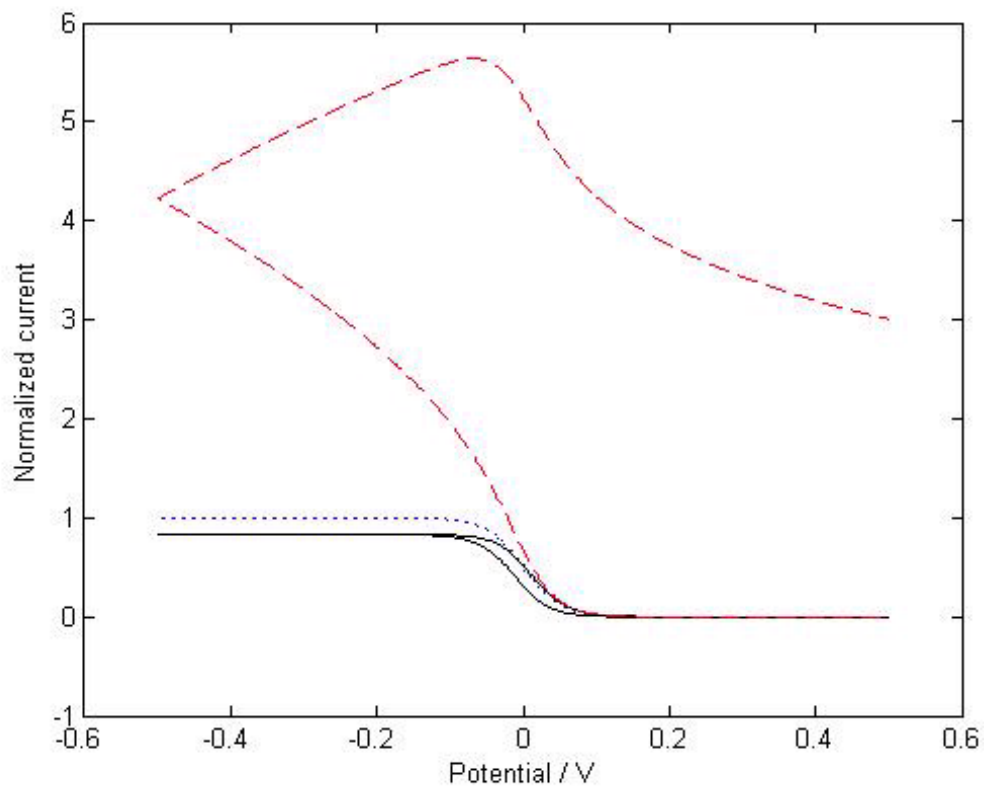Figure 51 shows that computer simulated cyclic voltammogram when $\omega = -0.8$ and $b = 3.5$ (solid) and its convoluted graph by the semi-infinite (dashed) and uniform film (dotted) convolution algorithms. As expected, the semi-infinite algorithm does not yield a sigmoidal response but the uniform film convolution does, as indicative of capturing effects of flux in both the solution and the film.

In conclusion, the uniform film convolution algorithm successful converts a CV to the sigmoidal response characteristic of a successful convolution algorithm. The

algorithm should allow system parameters to be extracted either by fitting or other

parametric protocol.

CHAPTER 6

CONCLUSION AND FUTURE WORK

Magnetic field effects on electrochemical energy conversion are the main topic of this thesis. The photoelectrochemical hydrogen evolution reaction on semiconductor electrodes was manipulated by magnetic modification. Modifications are achieved by applying ion conductive polymer with electrochemically inert magnetic particles to electrode surfaces. 15 % (v/v) magnetic modification on p-Si (1.5 Ωcm resistivity and (100) surface) enhanced the photoelectrochemical hydrogen evolution reaction current voltage profile by 400 mV in 0 pH electrolyte solution and achieved 6.2 % energy conversion efficiency.

The physical basis of the MFEs was also investigated. Heterogeneous electron transfer kinetics for the HER under magnetic modifications were measured on non-catalytic electrodes. On glassy carbon electrodes, the rate constant for HER on magnetically modified electrodes was 80,000 times higher than unmodified electrodes.

Self exchange reaction rate constants were also measured by tracking peak currents while varying redox couples, magnetic particles, and temperatures. Arrhenius type analyses were conducted to evaluate the MFE and the magnetic modifications decreased activation energy for outer sphere self exchange reaction by 30 - 40 %.

A kinetic model based on transition state theory was suggested for the MFE on the self exchange reactions. The model includes a pre-polarization step and an electron nuclear spin polarization step and the model successfully explained that for

the observed MFEs parameter, gHS, the rate constant and the activation energy are proportional to gHS.

A convolution technique for uniform film modified electrodes was developed and programmed in Matlab mathematic software. Using this technique more convenient and straightforward analysis became possible.

Although data have been collected for many different magnetic field experiments relating to electron transfer kinetics, a fundamental understanding of MFE on electrochemical system is still impcomplete. Because MFEs on electrochemistry under external uniform magnetic fields have rarely been detected, magnetic field gradients are speculated as the source of these phenomena. Therefore, a more fundamental understanding and modeling of the MFE effects are needed. Investigation of electron transfers kinetics under oscillating or gradually changing magnetic field is of particularly interest. For such experiments, conditions can be generated by using an electromagnet with AC currents for controlling the magnetic field oscillations. An electrochemical cell with a high viscosity electrolyte and high concentration of a redox couple, such as Nafion coated electrodes, could be placed within the magnetic field. Controlling magnetic field oscillations, the electrochemical response could be measured and recorded to reveal insights on the effects of magnetic field on electrochemical electron transfer rates. This set of experiments will advance the application of MFEs to all other types of electron transfer related chemistries.

APPENDIX A

COMPUTER SIMULATION FOR PHYSICAL DIFFUSION IN TO A THIN FILM

As we discussed, diffusion of redox couple consists of two phenomena, a physical motion and electron hopping. Because these two phenomena always occur simultaneously, a measurement of each parameter separately using electrochemical method has not been done. Here, peak currents are measured while redox couple is loaded in known thickness of an ion exchange polymer, Nafion. By mathematical modeling and computer programing of the diffusion profile, a method to get diffusion coefficient for the physical motion is suggested.

A.1   Experimental

To investigate physical diffusion characteristics of $Ru(bpy)_2^{2+/3+}$ in Nafion matrix, three glassy carbon electrodes were coated with Nafion with thickness of 6 μm and with Nafion and silane coated suspension with the same thickness, respectively. Six electrodes are placed in 1 mM $Ru(bpy)_2^{2+/3+}$ in 0.1M HNO_3 solution. Then cyclic voltammograms are recorded every 30 min for 15 hours.

A.2   Mathematical Description of the Model

The concentration profile when the film is in loading over time is shown in Figure A1. The x-axis is distance from an electrode surface and the y-axis is concentration of a redox couple.

To describe diffusion profile of this system, two Fick's second law equations are
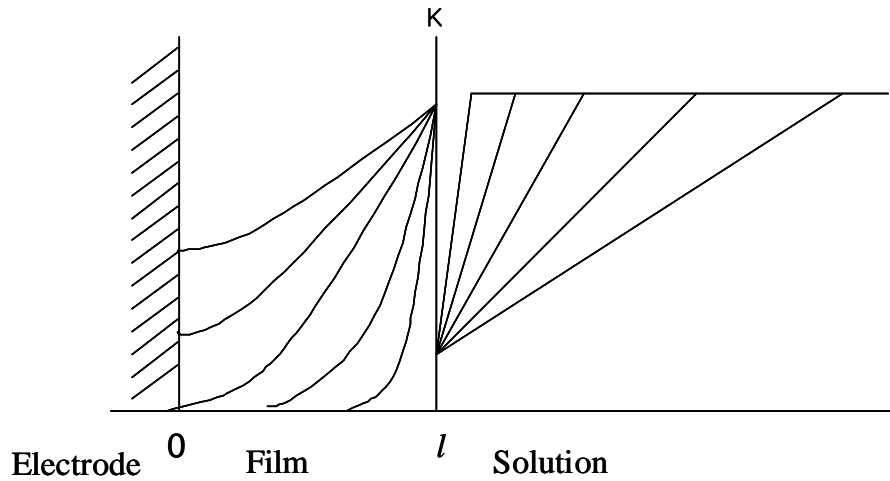
Figure A1. Concentration profile when the film is in loading over time. The x-axis is distance and the y-axis is concentration

used

$$\frac{\partial C_{f(x,t)}}{\partial t} = D_f \frac{\partial^2 C_{f(x,t)}}{\partial x^2} \qquad 0 \leq x \leq l \tag{A.1}$$

$$\frac{\partial C_{s(x,t)}}{\partial t} = D_s \frac{\partial^2 C_{s(x,t)}}{\partial x^2} \qquad l < x \tag{A.2}$$

Boundary conditions for this system are:

$$C_{f(x,0)} = 0 \tag{A.3}$$

$$D_f \frac{\partial C_{f(0,t)}}{\partial x} = 0 \tag{A.4}$$

$$C_{f(l^-,t)} = \kappa C_{s(l^+,t)} \tag{A.5}$$

$$D_f \frac{\partial C_{f(l^-,t)}}{\partial x} = D_s \frac{\partial C_{s(l^+,t)}}{\partial x} \tag{A.6}$$

$$C_{s(x,0)} = C^* \tag{A.7}$$

$$\lim_{x \to \infty} C_{s(x,t)} = C^* \tag{A.8}$$

Then Laplace transformations of them are

$$
\begin{array}{cc}
B.C & Laplace \\
C_{f(x,0)} = 0 & \\
D_f \frac{\partial C_{f(0,t)}}{\partial x} = 0 & D_f \frac{\partial \overline{C}_{f(0,s)}}{\partial x} = 0 \\
C_{f(l^-,t)} = \kappa C_{s(l^+,t)} & \overline{C}_{f(l^-,s)} = \kappa \overline{C}_{s(l^+,s)} \\
D_f \frac{\partial C_{f(l^-,t)}}{\partial x} = D_s \frac{\partial C_{s(l^+,t)}}{\partial x} & D_f \frac{\partial \overline{C}_{f(l^-,s)}}{\partial x} = D_s \frac{\partial \overline{C}_{s(l^+,s)}}{\partial x} \\
C_{s(x,0)} = C^* & \\
\lim_{x \to \infty} C_{s(x,t)} = C^* & \lim_{x \to \infty} \overline{C}_{s(x,t)} = \frac{C^*}{s}
\end{array} \tag{A.9}
$$

$$
\overline{C}_{f(x,s)} = \frac{C_{f(x,0)}}{s} + A \exp\left(-\sqrt{\frac{s}{D_f}}x\right) + B \exp\left(\sqrt{\frac{s}{D_f}}x\right) \tag{A.10}
$$

By the boundary condition Equations A.3 and A.4

$$
\frac{\partial \overline{C}_{f(x,s)}}{\partial x} = -\sqrt{\frac{s}{D_f}}A \exp\left(-\sqrt{\frac{s}{D_f}}x\right) + \sqrt{\frac{s}{D_f}}B \exp\left(\sqrt{\frac{s}{D_f}}x\right) \tag{A.11}
$$

$$
\frac{\partial \overline{C}_{f(0,s)}}{\partial x} = -\sqrt{\frac{s}{D_f}}A + \sqrt{\frac{s}{D_f}}B = 0 \tag{A.12}
$$

$$
A = B \tag{A.13}
$$

So

$$
\overline{C}_{f(x,s)} = A \left[\exp\left(-\sqrt{\frac{s}{D_f}}x\right) + \exp\left(\sqrt{\frac{s}{D_f}}x\right)\right] \tag{A.14}
$$

Laplace transform for in solvent phase is

$$
\overline{C}_{s(x,s)} = \frac{C_{s(x,0)}}{s} + C \exp\left(-\sqrt{\frac{s}{D_s}}x\right) + G \exp\left(\sqrt{\frac{s}{D_s}}x\right) \tag{A.15}
$$

By boundary condition Equation A.7

$$
\overline{C}_{s(x,s)} = \frac{C^*}{s} + C \exp\left(-\sqrt{\frac{s}{D_s}}x\right) + G \exp\left(\sqrt{\frac{s}{D_s}}x\right) \tag{A.16}
$$

By boundary condition Equation A.8

$$
\frac{C^*}{s} = \frac{C^*}{s} + C \exp\left(-\infty\right) + G \exp\left(\infty\right) \tag{A.17}
$$

The Second term on right side goes to zero and third term goes to infinite.

Therefore,

$$G = 0 \tag{A.18}$$

and

$$\overline{C}_{s(x,s)} = \frac{C^*}{s} + C \exp\left(-\sqrt{\frac{s}{D_s}}x\right) \tag{A.19}$$

By Equation A.10

$$\frac{A}{\kappa}\left[\exp\left(-\sqrt{\frac{s}{D_f}}l\right) + \exp\left(\sqrt{\frac{s}{D_f}}l\right)\right] = \frac{C^*}{s} + C\exp\left(-\sqrt{\frac{s}{D_s}}l\right) \tag{A.20}$$

To apply boundary condition Equation A.6, derivatives of A.19 and A.14 are

$$\frac{\partial \overline{C}_{f(x,s)}}{\partial x} = A\sqrt{\frac{s}{D_f}}\left[-\exp\left(-\sqrt{\frac{s}{D_f}}x\right) + \exp\left(\sqrt{\frac{s}{D_f}}x\right)\right] \tag{A.21}$$

$$\frac{\partial \overline{C}_{s(0,s)}}{\partial x} = -\sqrt{\frac{s}{D_f}}C\exp\left(-\sqrt{\frac{s}{Ds}}x\right) \tag{A.22}$$

Then by Equation A.6

$$D_f A\sqrt{\frac{s}{D_f}}\left[\begin{array}{c} -\exp\left(-\sqrt{\frac{s}{D_f}}l\right) \\ +\exp\left(\sqrt{\frac{s}{D_f}}l\right) \end{array}\right] = -D_s\sqrt{\frac{s}{D_s}}C\exp\left(-\sqrt{\frac{s}{D_s}}l\right) \tag{A.23}$$

$$\sqrt{D_f}A\left[\begin{array}{c} \exp\left(-\sqrt{\frac{s}{D_f}}l\right) \\ -\exp\left(\sqrt{\frac{s}{D_f}}l\right) \end{array}\right] = \sqrt{D_s}C\exp\left(-\sqrt{\frac{s}{D_s}}l\right) \tag{A.24}$$

We are interested in $C_{f(0,t)}$ which is transformed to $\overline{C}_{f(0,s)}$ Then,

$$\frac{A}{\kappa}\left[\exp\left(-\sqrt{\frac{s}{D_f}}l\right) + \exp\left(\sqrt{\frac{s}{D_f}}l\right)\right] - \frac{C^*}{s} = C\exp\left(-\sqrt{\frac{s}{D_s}}l\right) \tag{A.25}$$

and the Equation A.14

$$A\frac{\sqrt{D_f}}{\sqrt{D_s}}\left[\exp\left(-\sqrt{\frac{s}{D_f}}l\right) - \exp\left(\sqrt{\frac{s}{D_f}}l\right)\right] = C\exp\left(-\sqrt{\frac{s}{D_s}}l\right) \tag{A.26}$$

Then,

$$A\frac{\sqrt{D_f}}{\sqrt{D_s}}\left[\exp\left(-\sqrt{\frac{s}{D_f}}l\right)-\exp\left(\sqrt{\frac{s}{D_f}}l\right)\right] \tag{A.27}$$

$$=\frac{A}{\kappa}\left[\exp\left(-\sqrt{\frac{s}{D_f}}l\right)+\exp\left(\sqrt{\frac{s}{D_f}}l\right)\right]-\frac{C^*}{s} \tag{A.28}$$

$$\frac{C^*}{s}=\frac{A}{\kappa}\left[\exp\left(-\sqrt{\frac{s}{D_f}}l\right)+\exp\left(\sqrt{\frac{s}{D_f}}l\right)\right] \tag{A.29}$$

$$-A\frac{\sqrt{D_f}}{\sqrt{D_s}}\left[\exp\left(-\sqrt{\frac{s}{D_f}}l\right)-\exp\left(\sqrt{\frac{s}{D_f}}l\right)\right] \tag{A.30}$$

$$\frac{C^*}{s}=A\left[\begin{array}{c}\frac{1}{\kappa}\exp\left(-\sqrt{\frac{s}{D_f}}l\right)+\frac{1}{\kappa}\exp\left(\sqrt{\frac{s}{D_f}}l\right)\\[2mm]-\frac{\sqrt{D_f}}{\sqrt{D_s}}\exp\left(-\sqrt{\frac{s}{D_f}}l\right)+\frac{\sqrt{D_f}}{\sqrt{D_s}}\exp\left(\sqrt{\frac{s}{D_f}}l\right)\end{array}\right] \tag{A.31}$$

$$=A\left[\begin{array}{c}\frac{1}{\kappa}\exp\left(-\sqrt{\frac{s}{D_f}}l\right)-\frac{\sqrt{D_f}}{\sqrt{D_s}}\exp\left(-\sqrt{\frac{s}{D_f}}l\right)\\[2mm]+\frac{1}{\kappa}\exp\left(\sqrt{\frac{s}{D_f}}l\right)+\frac{\sqrt{D_f}}{\sqrt{D_s}}\exp\left(\sqrt{\frac{s}{D_f}}l\right)\end{array}\right] \tag{A.32}$$

$$=A\left[\begin{array}{c}\left(\frac{1}{\kappa}-\frac{\sqrt{D_f}}{\sqrt{D_s}}\right)\exp\left(-\sqrt{\frac{s}{D_f}}l\right)\\[2mm]+\left(\frac{1}{\kappa}+\frac{\sqrt{D_f}}{\sqrt{D_s}}\right)\exp\left(\sqrt{\frac{s}{D_f}}l\right)\end{array}\right] \tag{A.33}$$

$$A=\frac{C^*}{s\left[\left(\frac{1}{\kappa}-\frac{\sqrt{D_f}}{\sqrt{D_s}}\right)\exp\left(-\sqrt{\frac{s}{D_f}}l\right)+\left(\frac{1}{\kappa}+\frac{\sqrt{D_f}}{\sqrt{D_s}}\right)\exp\left(\sqrt{\frac{s}{D_f}}l\right)\right]} \tag{A.34}$$

Let

$$\gamma=\sqrt{\frac{D_f}{D_s}} \tag{A.35}$$

$$A=\frac{C^*}{s\left[\left(\frac{1}{\kappa}-\gamma\right)\exp\left(-\sqrt{\frac{s}{D_f}}l\right)+\left(\frac{1}{\kappa}+\gamma\right)\exp\left(\sqrt{\frac{s}{D_f}}l\right)\right]} \tag{A.36}$$

$$=\frac{C^*}{s\left(\frac{1}{\kappa}+\gamma\right)\exp\left(\sqrt{\frac{s}{D_f}}l\right)}\frac{1}{\left[1+\frac{(1-\kappa\gamma)\exp\left(-\sqrt{\frac{s}{D_f}}l\right)}{(1+\kappa\gamma)\exp\left(\sqrt{\frac{s}{D_f}}l\right)}\right]} \tag{A.37}$$

at

$$\omega = \frac{(1 - \kappa\gamma)}{(1 + \kappa\gamma)} \tag{A.38}$$

Then,

$$A = \frac{C^*}{s\left(\frac{1}{\kappa} + \gamma\right)\exp\left(\sqrt{\frac{s}{D_f}}l\right)} \frac{1}{\left[1 + \omega\exp\left(-2\sqrt{\frac{s}{D_f}}l\right)\right]} \tag{A.39}$$

Because

$$\frac{1}{1 + a} = \sum_{j=0}^{\infty}(-1)^j a^j \tag{A.40}$$

$$A = \frac{C^*}{s\left(\frac{1}{\kappa} + \gamma\right)\exp\left(\sqrt{\frac{s}{D_f}}l\right)} \sum_{j=0}^{\infty}(-1)^j \omega^j \exp\left(-2\sqrt{\frac{s}{D_f}}lj\right) \tag{A.41}$$

Put this to Equation A.14

$$\overline{C}_{f(x,s)} = \frac{C^*}{s\left(\frac{1}{\kappa}+\gamma\right)\exp\left(\sqrt{\frac{s}{D_f}}l\right)} \tag{A.42}$$

$$\times \sum_{j=0}^{\infty}(-1)^j\omega^j\exp\left(-2\sqrt{\frac{s}{D_f}}lj\right)\left[\begin{array}{c}\exp\left(-\sqrt{\frac{s}{D_f}}x\right)\\+\exp\left(\sqrt{\frac{s}{D_f}}x\right)\end{array}\right] \tag{A.43}$$

$$= \left[\begin{array}{c}\exp\left(-\sqrt{\frac{s}{D_f}}x\right)\exp\left(-\sqrt{\frac{s}{D_f}}l\right)\frac{C^*}{s\left(\frac{1}{\kappa}+\gamma\right)}\\\times \sum_{j=0}^{\infty}(-1)^j\omega^j\exp\left(-2\sqrt{\frac{s}{D_f}}lj\right)\end{array}\right] \tag{A.44}$$

$$+ \left[\begin{array}{c}\exp\left(\sqrt{\frac{s}{D_f}}x\right)\exp\left(-\sqrt{\frac{s}{D_f}}l\right)\frac{C^*}{s\left(\frac{1}{\kappa}+\gamma\right)}\\\times \sum_{j=0}^{\infty}(-1)^j\omega^j\exp\left(-2\sqrt{\frac{s}{D_f}}lj\right)\end{array}\right] \tag{A.45}$$

$$= \exp\left(-\sqrt{\frac{s}{D_f}}(x+l)\right)\frac{C^*}{s\left(\frac{1}{\kappa}+\gamma\right)}\sum_{j=0}^{\infty}(-1)^j\omega^j\exp\left(-2\sqrt{\frac{s}{D_f}}lj\right)$$

$$+ \exp\left(\sqrt{\frac{s}{D_f}}(x-l)\right)\frac{C^*}{s\left(\frac{1}{\kappa}+\gamma\right)}\sum_{j=0}^{\infty}(-1)^j\omega^j\exp\left(-2\sqrt{\frac{s}{D_f}}lj\right) \tag{A.46}$$

$$= \frac{C^*}{s\left(\frac{1}{\kappa}+\gamma\right)}\sum_{j=0}^{\infty}(-1)^j\omega^j\exp\left(-2\sqrt{\frac{s}{D_f}}lj-\sqrt{\frac{s}{D_f}}(x+l)\right)$$

$$+ \frac{C^*}{s\left(\frac{1}{\kappa}+\gamma\right)}\sum_{j=0}^{\infty}(-1)^j\omega^j\exp\left(-2\sqrt{\frac{s}{D_f}}lj+\sqrt{\frac{s}{D_f}}(x-l)\right) \tag{A.47}$$

$$= \frac{C^*}{s\left(\frac{1}{\kappa}+\gamma\right)}\sum_{j=0}^{\infty}(-1)^j\omega^j\exp\sqrt{\frac{s}{D_f}}(-2lj-x-l)$$

$$+ \frac{C^*}{s\left(\frac{1}{\kappa}+\gamma\right)}\sum_{j=0}^{\infty}(-1)^j\omega^j\exp\sqrt{\frac{s}{D_f}}(-2lj+x-l) \tag{A.48}$$

$$= \frac{C^*}{s\left(\frac{1}{\kappa}+\gamma\right)}\sum_{j=0}^{\infty}(-1)^j\omega^j\exp\left[-\sqrt{\frac{s}{D_f}}((2j+1)l+x)\right]$$

$$+ \frac{C^*}{s\left(\frac{1}{\kappa}+\gamma\right)}\sum_{j=0}^{\infty}(-1)^j\omega^j\exp\left[-\sqrt{\frac{s}{D_f}}((2j+1)l-x)\right] \tag{A.49}$$

Since

$$\frac{C^*}{s} \exp\left(-\sqrt{\frac{s}{D}}x\right) \longleftrightarrow C^* \operatorname{erf} c\left(\frac{x}{2\sqrt{Dt}}\right)$$

$$\overline{C}_{f(x,s)} = \frac{C^*}{s\left(\frac{1}{\kappa}+\gamma\right)} \sum_{j=0}^{\infty} (-1)^j \omega^j \exp\left[-\sqrt{\frac{s}{D_f}}((2j+1)l+x)\right]$$

$$+ \frac{C^*}{s\left(\frac{1}{\kappa}+\gamma\right)} \sum_{j=0}^{\infty} (-1)^j \omega^j \exp\left[-\sqrt{\frac{s}{D_f}}((2j+1)l-x)\right]$$

$$C_{f(x,t)} = \frac{C^*}{\left(\frac{1}{\kappa}+\gamma\right)} \sum_{j=0}^{\infty} (-1)^j \omega^j \operatorname{erf} c\left[\frac{((2j+1)l+x)}{2\sqrt{D_f t}}\right]$$

$$+ \frac{C^*}{\left(\frac{1}{\kappa}+\gamma\right)} \sum_{j=0}^{\infty} (-1)^j \omega^j \operatorname{erf} c\left[\frac{((2j+1)l-x)}{2\sqrt{D_f t}}\right]$$

Then we are interested in

$$C_{f(o,t)} = \frac{C^*}{\left(\frac{1}{\kappa}+\gamma\right)} \sum_{j=0}^{\infty} (-1)^j \omega^j \operatorname{erf} c\left[\frac{(2j+1)l}{2\sqrt{D_f t}}\right] \tag{A.50}$$

$$+ \frac{C^*}{\left(\frac{1}{\kappa}+\gamma\right)} \sum_{j=0}^{\infty} (-1)^j \omega^j \operatorname{erf} c\left[\frac{(2j+1)l}{2\sqrt{D_f t}}\right] \tag{A.51}$$

$$= \frac{2C^*}{\left(\frac{1}{\kappa}+\gamma\right)} \sum_{j=0}^{\infty} (-1)^j \omega^j \operatorname{erf} c\left[\frac{(2j+1)l}{2\sqrt{D_f t}}\right] \tag{A.52}$$

Let

$$b = \frac{l}{2\sqrt{D_f t}} \tag{A.53}$$

Then

$$C_{f(o,b)} = \frac{2C^*}{\left(\frac{1}{\kappa}+\gamma\right)} \sum_{j=0}^{\infty} (-1)^j \omega^j \operatorname{erf} c\left[(2j+1)b\right] \tag{A.54}$$

For varification

$$C_{f(0,B)} \;=\; \frac{2C^*\kappa}{(1+\kappa\gamma)} \sum_{j=0}^{\infty} (-1)^j \omega^j \operatorname{erf} c\,[(2j+1)b] \tag{A.55}$$

$$=\; 2C^*\kappa \left(\frac{1}{(1+\kappa\gamma)}\right) \sum_{j=0}^{\infty} (-1)^j \omega^j \operatorname{erf} c\,[(2j+1)b] \tag{A.56}$$

$$=\; 2C^*\kappa \left(\sum_{j=0}^{\infty} (-1)^j \kappa^j \gamma^j\right) \sum_{j=0}^{\infty} (-1)^j \omega^j \operatorname{erf} c\,[(2j+1)b] \tag{A.57}$$

$$=\; 2C^*\kappa \sum_{j=0}^{\infty} \kappa^j \gamma^j \omega^j \operatorname{erf} c\,[(2j+1)b] \tag{A.58}$$

$$=\; 2C^*\kappa \sum_{j=0}^{\infty} (\kappa\gamma\omega)^j \operatorname{erf} c\,[(2j+1)b] \tag{A.59}$$

$$=\; 2C^* \sum_{j=0}^{\infty} (\gamma\omega)^j \kappa^{(j+1)} \operatorname{erf} c\,[(2j+1)b] \tag{A.60}$$

$$\gamma = \sqrt{\frac{D_f}{D_s}} \tag{A.61}$$

$$\omega = \frac{(1-\kappa\gamma)}{(1+\kappa\gamma)} \tag{A.62}$$

$$b = \frac{l}{2\sqrt{D_f t}} \tag{A.63}$$

$$\frac{1}{1+a} = \sum_{j=0}^{\infty} (-1)^j a^j \tag{A.64}$$

Verifications are

$$t \;\rightarrow\; \infty \tag{A.65}$$

$$b \;\rightarrow\; 0 \tag{A.66}$$

$$\operatorname{erf} c\,[(2j+1)b] = 1$$

$$C_{f(0,0)} = \frac{2\kappa C^*}{(1+\kappa\gamma)} \sum_{j=0}^{\infty} (-1)^j \omega^j \tag{A.67}$$

$$= \frac{2\kappa C^*}{(1+\kappa\gamma)} \frac{1}{1+\omega} \tag{A.68}$$

$$= \frac{2\kappa C^*}{(1+\kappa\gamma)} \frac{1}{1+\frac{(1-\kappa\gamma)}{(1+\kappa\gamma)}} \tag{A.69}$$

$$= \frac{2\kappa C^*}{(1+\kappa\gamma)} \frac{(1+\kappa\gamma)}{(1+\kappa\gamma)+(1-\kappa\gamma)} \tag{A.70}$$

$$= \kappa C^* \tag{A.71}$$

A.3 Results

The experimental result of peak currents over time when $Ru(bpy)_2^{2+}$ is loaded in Nafion and magnetically modified Nafion is shown in Figure A2. Peak currents are normalized so the currents enhanced by magnetic field effects are minimized. The result is evident that physical diffusion of $Ru(bpy)_2^{2+}$ in Nafion and Nafion with magnetic microparticles is the same. Another interpretation is magnetic modification does not affect physical diffusion.

The derived equation is coded to simulate the concentration on the electrode surface that is physically diffused through Nafion. Matlab is used for the simulation calculation and the code is written in APPENDIX B. Figure A3 shows the result of the simulation when. $D_f = 8 \times 10^{-8}$ cm^2/s, $D_s = 8 \times 10^{-5}$ cm^2/s, $\kappa = 20$, C$^* = 0.05$ and $l = 0.006$ cm.
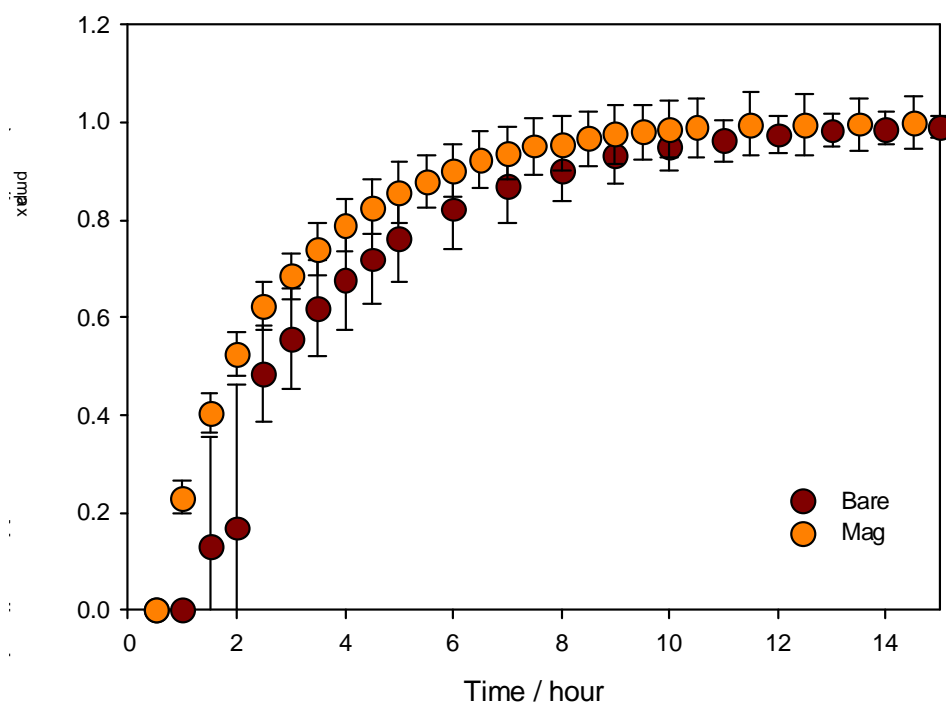
Figure A2. Normalized peak current at an electrode surface versus time when $Ru(bpy)_3^{2+}$ diffuses in Nafion matrix.
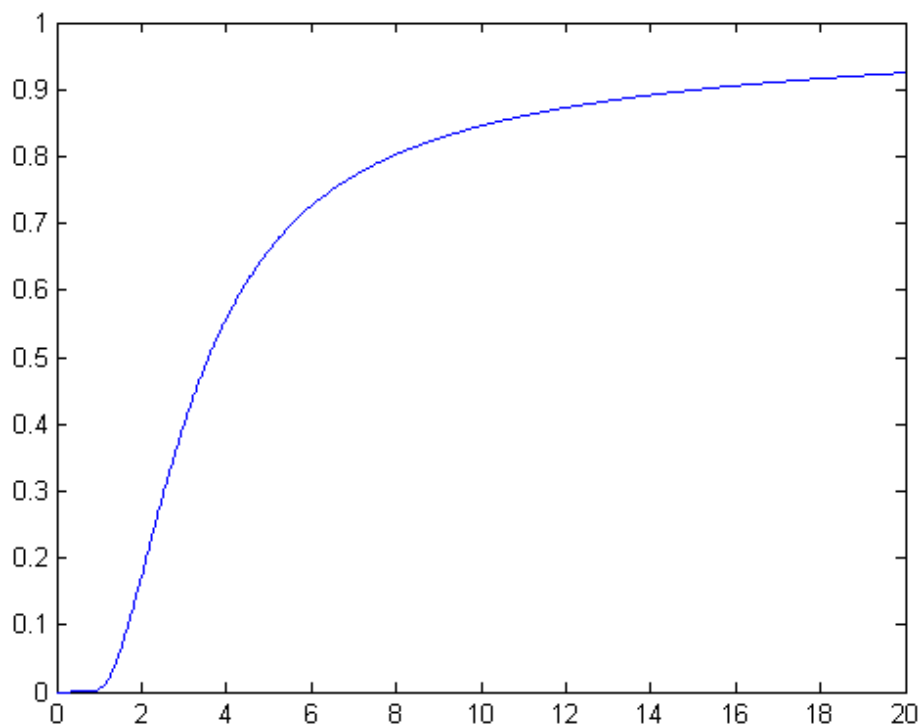
Figure A3. Computer simmulated peak current response with time when. $D_f = 8 \times 10^{-8}$ cm^2/s, $D_s = 8 \times 10^{-5}$ cm^2/s, $\kappa = 20$, C* = 0.05 and $l = 0.006$ cm.

A.4 Computer Code for Physical Diffusion into a Thin Film

```
function filmloading02

%dt=1;

df=0.00000007;

ds=0.00008;

kapa=20

conc=0.05;

l=0.0006;

zi=sqrt(df/ds)

omega=(1-kapa*zi)/(1+kapa*zi)

infi=0:1000;

ziomega=zi*omega;

ziomekapa=zi*omega*kapa;

presig=2*conc/(1/kapa+zi);

for T=1:720

b=l/(2*(df*T*100)^1/2);

errfc=erfc(((2.*infi)+1).*b);

prerr1=(-1).^infi;

prerr2=(omega.^infi);

prerr=prerr1.*prerr2;

sig=prerr.*errfc;

c(T)=presig.*sum(sig);
```

```
i(T)=c(T)^(4/3);

t(T)=T*100/3600;

end

plot(t,c)

end
```

APPENDIX B

COMPUTER CODE FOR HETEROGENEOUS ELECTRON TRANSFER RATE

CONSTANT

Next code is for the Visual Basic in the Microsoft Excel 2007. The program is coded basically for a cyclic voltammogram. In this thesis, this code is run for a single sweep to simulate a potential sweep voltammogram. Heterogeneous electron transfer rate constants are obtained by adjusting parameters.

```
Sub HHCGC()
'define arrays
Dim FAOLD(1001) As Double
Dim FANEW(1001) As Double
Dim FBOLD(1001) As Double
Dim FBNEW(1001) As Double
'ask start
MsgBox "Start?"
Range(Cells(14, 1), Cells(10014, 8)).ClearContents
'Input Simulation variables
Einit = Range("B2")
Efin = Range("B3")
T = Range("B7")
fConc = Range("B5")
```

```
tk = Range("B8")

A = Range("B4")

D = Range("B9")

Conc = Range("B12")

jmax = Range("D11")

kmax = Range("D12")

E01 = Range("D2")

alpha1 = Range("D3")

Dm1 = Range("D4")

XO1 = Range("D5")

n1 = Range("D6")

D1 = Range("D8")

'Initialize Arrays

For i = 0 To jmax

FAOLD(i) = fConc

FANEW(i) = FAOLD(i)

FBOLD(i) = 0

FBNEW(i) = 0

Next i

'Start Time Counter, k=1

For k = 1 To kmax

'Calculate FNEW(j) for 2 to jmax
```

For j = 2 To jmax - 1

FANEW(j) = FAOLD(j) + Dm1 * (FAOLD(j + 1) - 2 * FAOLD(j) + FAOLD(j - 1))

FBNEW(j) = FBOLD(j) + Dm1 * (FBOLD(j + 1) - 2 * FBOLD(j) + FBOLD(j - 1))

Next j

'Calculate Current Allowing Electrolysis in box j=1

If k < 0.5 * kmax Then

E = Einit + 2 * (Efin - Einit) * k / kmax

Else

E = Einit + 2 * (Efin - Einit) * (1 - k / kmax)

End If

Enorm1 = n1 * 96485 / 8.314 / T * (E - E01)

XF1 = XO1 * Exp(-alpha1 * Enorm1)

XB1 = XO1 * Exp((1 - alpha1) * Enorm1)

Z = 2 * Sqr(Dm1 * kmax) * ((XF1 * FAOLD(1) - XB1 * FBOLD(1)) / (2 * Sqr(Dm1 * kmax) + XF1 + XB1))

i = Z * n1 * 96485 * A * Conc * Sqr(D1) / Sqr(tk)

'diffusion in box j=1

FANEW(1) = FAOLD(1) + Dm1 * (FAOLD(2) - FAOLD(1))

FBNEW(1) = FBOLD(1) + Dm1 * (FBOLD(2) - FBOLD(1))

'current in box j=1

FANEW(1) = FANEW(1) - Z * Sqr(Dm1 / kmax)

```
FBNEW(1) = FBNEW(1) + Z * Sqr(Dm1 / kmax)

'Aging

For m = 1 To jmax

FAOLD(m) = FANEW(m)

FBOLD(m) = FBNEW(m)

'Print Concentration profile

Cells(13 + m, 1) = FAOLD(m)

Cells(13 + m, 2) = FBOLD(m)

Next m

'Print Currnet and Potential

Cells(13 + k, 9) = i

Cells(13 + k, 6) = E

Cells(13 + k, 7) = Z

'display progress

'If (k Mod 25 = 0) Then

Application.ScreenUpdating = True

'End If

Next k

End Sub
```

APPENDIX C

COMPUTER CODE FOR THIN FILM CONVOLUTION TECHNIQUE

This code is for Matlab mathematical software. Experimental or simulated cyclic voltammogram data can be imported and convoluted. For example, 'Current-CA+P999_b3p5.txt' is imported here.

```
function totaltfconv09

%dt=1;

cv=csvread('Current-CA+P999_b3p5.txt');

v=cv(:,4);

i=cv(:,5);

infi=1:1000;

kmax=1000;

deltaE=1;

F=96485;

T=298.15;

R=8.314;

b=3.5;

bnew=b*sqrt(kmax*R*T/(2*deltaE*F));

q=1:1000;

omega=0.999;

for j=1:1000; % tf convol
```

```
sig=exp(-(bnew.*infi).^2./j).*(-omega).^infi; % tf convol

sigma(1001-j)=sum(sig); % tf convol

end; % tf convol

for j=1:1000

s(j)=sqrt(1000-j+0.3);

end

for t=1:1000

snew=s(1001-t:end);

inew=i(1:t)';

sigmanew=sigma(1001-t:end); % tf convol

conv=inew./snew+inew./snew.*sigmanew.*2;

sumicon(t)=sum(conv)/sqrt(pi*kmax) ;

end

inorm=i/sqrt(2*F*deltaE/(R*T));

plot(v,sumicon,v,inorm)

ylabel('i(normalized)')

xlabel('V')

end
```

REFERENCES

[1] Minteer, S. D. *Magnetic Field Effects on Electron Transfer Reactions,* Ph.D thesis, University of Iowa, 2000, 2000.

[2] Gellett, W. L. *Magnetic Microparticles on Electrodes: Polymer Electrolyte Membrane Fuel Cells, Carbon Monoxide Oxidation, and Transition Metal Complex Electrochemistry,* Ph.D thesis, University of Iowa, 2004, 2004.

[3] Atkins, P.; Lambert, T. *The Effect of a Magnetic Field on Chemical Reactions,* Annual Report of Progress in Chemistry **1975,** *72A,* 67-88.

[4] Atkins, P. *Magnetic field effects,* Chemistry in Britian **1976,** *12,* 214-228.

[5] Buchachenko, A. *Magnetic Effects in Chemical Reactions,* Russ. Chem. Rev. **1976,** *45,* 375-390.

[6] Sagdeev, R.; Salikhov, K.; Molin, Y. M. *The Influence of the Magnetic Field on Processes Involving Radicals and Triplet Molecules in Solutions,* Russ. Chem. Rev. **1977,** *46,* 297-315.

[7] Steiner, U.; Ulrich, T. *Magnetic Field Effects in Chemical Kinetics and Related Phenomena,* Chem. Rev. **1989,** *89,* 51-147.

[8] Tacken, R. A.; Janssen, L. J. J. *Applications of Magnetoelectrolysis,* J. App. Electrochem. **1995,** *25,* 1-5.

[9] Fahidy, T. *Magnetoelectrolysis,* J. Appl. Electrochem. **1983,** *13,* 553-563.

[10] Ragsdale, S.; Lee, J.; White, H. *Analysis of the Magnetic Force Generated at a Hemispherical Microelectrode,* Anal. Chem. **1997,** *69,* 2072-2076.

[11] Ragsdale, S.; Grant, K.; White, H. *Electrochemically Generated Magnetic Forces. Enhanced Transport of a Paramagnetic Redox Species in Large, Nonuniform Magnetic Fields,* J. Am. Chem. Soc. **1998,** *120,* 13461-13468.

[12] Ragsdale, S.; White, H. *Imaging Microscopic Magnetohydrodynamic Flows,* Anal. Chem. **1999,** *71,* 1923-1927.

[13] Leventis, N.; Gao, X. *Nd-Fe-B Permanent Magnet Electrodes. Theoretical Evaluation and Experimental Demonstration of the Paramagnetic Body Forces,* J. Am. Chem. Soc. **2002,** *124,* 1079-1088.

[14] Arumugam, P. U.; Fakunle, E. S.; Anderson, E. C.; Evans, S. R.; King, K. G.; Aguilar, Z. P.; Carter, C. S.; Fritsch, I. *Characterization and Pumping,* Journal of The Electrochemical Society **2006,** *153,* E185-E194.

[15] Leddy, J.; Zook, L. A.; Amarasinghe, S. US Patent 5,871,625,, *Magnetic Composites for Improved Electrolysis,* 16 February 1999.

[16] Leddy, J.; Amarasinghe, S.; Zook, L. US Patent 6,303,242 B1,, *Gradient Interface Magnetic Composites and Methods Therefor,* 16 October 2001.

[17] Leddy, J.; Amarasinghe, S.; Zook, L. A.; Tinoco, F. *Magnetic Ion Exchange Polymer Composites: Transport Enhancements Driven by Non-Uniform Magnetic Fields and Magnetic Moments of Transported Species,* in *Proceedings of the 37th Power Sources Conference*; United States Army Research Laboratory: 1996 pages 93–95.

[18] Leddy, J.; Chung, H. *Magnetically Modified Fuel Cells,* in *39th Power Sources Proceedings*; 2000 pages 144–147.

[19] Leddy, J.; Amarasinghe, S.; Tinoco, F. US Patent 5,928,804,, *Fuel Cells Incorporating Magnetic Composites Having Distinct Flux Properties,* 27 July 1999.

[20] Leddy, J.; Zook, L.; Amarasinghe, S. US Patent 6,207,313,, *Magnetic Composites and Methods for Improved Electrolysis,* 27 March 2001.

[21] Leddy, J.; Amarasinghe, S. US Patent 6,322,676,, *Magnetic Composites Exhibiting Distinct Flux Properties Due to Gradient Interfaces,* 27 November 2001.

[22] Leddy, J.; Zook, L. A.; Amarasinghe, S. US Patent 5,981,085,, *Magnetic Composites and Methods for Improved Electrolysis,* 9 November 1999.

[23] Dunwoody, D. C.; Wolf, A. K. H.; Gellett, W. L. Magnetically Modified Carbon Paste Electrodes: Method for Construction and Demonstration of Increased Electrochemical Flux over Unmodified Carbon Paste Electrodes, in *Electrode Processes VII*; Birss, V., Ed.; The Electrochemical Society: Pennington, NJ, 2005 pages 181–191.

[24] Gellett, W.; Dunwoody, D.; Leddy, J. *Self-hydrating Polymer Electrolyte Fuel Cells,* in *41st Power Sources Proceedings*; Philadelphia, PA, 2004 pages 251–254.

[25] Zou, P.; Leddy, J. *Magnetized Nickel Electrodes for Improved Charge and Discharge Rates in Nickel Metal Hydride and Nickel Cadmium Batteries,* Electrochemical and Solid-State Letters **2006,** *9,* A43-A45.

[26] Leddy, J.; Tesene, J. P. Published US Patent Application, Publication Number 20070009771,, *Batteries and battery components with magnetically modified manganese dioxide,* 11 January 2007.

[27] Tesene, J. P. *Magnetically-Treated Electrolytic Manganese Dioxide in Alkaline Electrolyte,* Thesis, University of Iowa, 2005, 2005.

[28] Perry N.; Jewett Motsegood, Jessica; Leddy, J.*, Magnetically Modified Electrolytic Manganese Dioxide: Application Toward Alkaline Batteries,* 2009.

[29] Honda, K.; Fujishima, A. *Electrochemical Photolysis of Water at a Semiconductor Electrode,* Nature **1972,** *238,* 37-38.

[30] Bard, A. J. *Design of semiconductor photoelectrochemical systems for solar energy conversion,* The Journal of Physical Chemistry **1982,** *86,* 172-177.

[31] Lewis, N. S. *Chemical Control of Charge Transfer and Recombination at Semiconductor Photoelectrode Surfaces,* Inorganic Chemistry **2005,** *44,* 6900-6911.

[32] Turner, J. *Oxygen catalysis: The other half of the equation,* Nat Mater **2008,** *7,* 770-771.

[33] Wang, H.; Deutsch, T.; Turner, J. A. *Direct Water Splitting under Visible Light with Nanostructured Hematite and WO_3 Photoanodes and a $GaInP_2$ Photocathode,* Journal of The Electrochemical Society **2008,** *155,* F91-F96.

[34] Turner, J. A. American Association for the Advancement of Science,*, Sustainable Hydrogen Production,* 2004 Science Accession Number: 14246263; Source Information: 8/13/2004, Vol. 305 Issue 5686, p972; Subject Term: ENERGY consumption; Subject Term: ENERGY minerals; Subject Term: POWER resources; Subject Term: ENERGY management; Subject Term: EMISSIONS; Geographic Subject: UNITED States; Number of Pages: 3p; Document Type: Article; Full Text Word Count: 2559.

[35] Bockris, J. O.; Srinivasan, S. *Fuel Cells: Their Electrochemistry;* McGraw-Hill: New York, 1969.

[36] Marcus, R. *Electron Transfer at Electrodes and in Solution,* Electrochim. Acta **1968,** *13,* 995-1003.

[37] Bard, A.; Faulkner, L. *Electrochemical Methods;* John Wiley & Sons, Inc.: New York, Second ed.; 2001.

[38] Lewis, N. S. *Light work with water,* Nature **2001,** *414,* 589-590.

[39] Amarasinghe, S.; Minteer, S. D.; Zook, L. A.; Dunwoody, D. C.; Spolar, C.; Chung, H.; Leddy, J. US Patent 6,355,166 B1,, *Magnetically Enhanced Composite Materials and Methods for Making and Using the Same,* 12 March 2002.

[40] Kern, D. P. W. *Cleaning Solutions Based on Hydrogen Peroxide for Use in Silicon Semiconductor Technology,* RCA Review **1970,** *187,* 187-206.

[41] Zook, L. A.; Leddy, J. *Nafion - Cold Cast, Thermally Processed, and Commercial Films: Comparison of Density, Water Content, and Equivalent Weight,* in *New Directions in Electroanalytical Chemistry II*, Vol. 99-5; Leddy, J.; Vanýsek, P.; Porter, M., Eds.; The Electrochemical Society, Inc., Pennington, NJ: Seattle, WA, 1999 pages 217–224.

[42] Zhang, X. G. *Electrochemistry of Silicon and its Oxide.;* Kluwer Academic/Plenum Publishers: Dordrecht, Neth., 2001.

[43] Hilal, H. S.; Turner, J. A. *Controlling charge-transfer processes at semiconductor/liquid junctions,* Electrochimica Acta **2006,** *51,* 6487-6497.

[44] Hagedorn, K.; Forgacs, C.; Collins, S.; Maldonado, S. *Design Considerations for Nanowire Heterojunctions in Solar Energy Conversion/Storage Applications,* The Journal of Physical Chemistry C *114,* 12010-12017.

[45] Chen, T.-Y.; Leddy, J. *Ion Exchange Capacity of Nafion and Nafion Composites,* Langmuir **2000,** *16,* 2866-2871.

[46] Hubbard, A.; Anson, F. The Theory and Practice of Electrochemistry with Thin Layer Cells, in *Electroanalytical Chemistry*, Vol. 4; Bard, A. J., Ed.; Marcel Dekker: New York, 1970 pages 129–214.

[47] Dahms, K. *Electronic Conduction in Aqueous Solution,* J. Phys. Chem. **1968,** *72,* 362-364.

[48] Ruff, I.; Friedrich, V. *Transfer Diffusion. I. Theoretical,* J. Phys. Chem. **1971,** *75,* 3297-3302.

[49] Ruff, I.; Friedrich, V.; Demeter, K.; Csillag, K. *Transfer Diffusion. II. Kinetics of Electron Exchange Reaction between Ferrocene and Ferricinium Ion in Alcohols,* J. Phys. Chem. **1971,** *75,* 3303-3309.

[50] Ruff, I.; Korosi-Odor, I. *Application of Diffusion Constant Measurement to the Determination of the Rate Constant of Electron-Exchange Reactions,* Inorg. Chem. **1970,** *9,* 186-188.

[51] Bard, A. J. *Electroanalytical Chemistry;* Vol. 18 Dekker: New York, 1994.

[52] Zook, L. A.; Leddy, J. *Density and Solubility of Nafion: Recast, Annealed, and Commercial Films,* Anal. Chem. **1996,** *68,* 3793-3796.

[53] Nicholson, R.; Shain, I. *Single Scan and Cyclic Methods Applied to Reversible, Irreversible, and Kinetic Systems,* Anal. Chem. **1964,** *36,* 706-723.

[54] Ruff, I.; Zimonyi, M. *The Rate of the Electron-Exchange between the Tris-1,10-Phenathroline Complexes of Iron (II) and Iron (II),* Electrochimica Acta **1973,** *18,* 515-516.

[55] White, H. S.; Leddy, J.; Bard, A. J. *Investigation of Charge Transport Mechanisms in Nafion Polymer-Modified Electrodes,* J. Am. Chem. Soc. **1982,** *104,* 4811-4817.

[56] Truhlar, D. G.; Garrett, B. C.; Klippenstein, S. J. *Current Status of Transition-State Theory,* The Journal of Physical Chemistry **1996,** *100,* 12771-12800.

[57] Netz, R. R. *Debye-Huuml;ckel theory for interfacial geometries,* Physical Review E **1999,** *60,* 3174.

[58] Hettige, C. *Characterization and Models for Uniform and Non-uniform Films on Electrodes,* Thesis, University of Iowa, 2007, 2007.

[59] Oldham, K. *Tables of Semiintegrals,* J. Electroanal. Chem. **1997,** *430,* 1-14.

[60] Andrieux, C.; Saveant, J. *Kinetics of Electrochemical Reactions Mediated by Redox Polymer Films: Reversible Cross-Exhange Reactions,* J. Electroanal. Chem. **1982,** *142,* 1-30.

[61] Leddy, J.; Bard, A. *Determination of Heterogeneous Electron Transfer Kinetics of Poly(Vinyl Ferrocene) and Nafion/Ru(bpy)$_3^{2+}$ Polymer-Modified Electrodes by Convolution Voltammetry',* J. Electroanal. Chem. **1985,** *189,* 203-219.

[62] Myland, J. C.; Oldham, K. B. *A model of cyclic voltammetry for a thin organic layer sandwiched between an electrode and an aqueous solution.: Convolutive modelling in the absence of supporting electrolyte,* Journal of Electroanalytical Chemistry **2002,** *530,* 1-9.

[63] Leddy, J.; Bard, A.; Maloy, J.; Saveant, J. *Effect of a Finite Mass Transfer Rate across the Film-Solution Interface at Steady State,* J. Electroanal. Chem. **1985,** *187,* 205-227.